Mapping of Tropospheric Greenhouse Gases using Airborne Near-Infrared/Shortwave-Infrared Spectroscopy

Pietro Paolo Bertagnolio

August 19, 2008

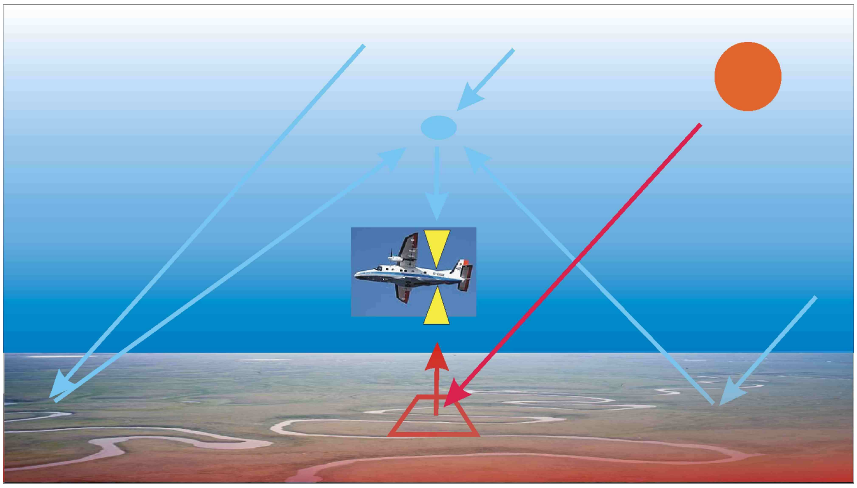

Master Thesis

Supervisor:

Dr. Michael Buchwitz

Examiners:

Prof. John P. Burrows

Prof. Justus Notholt

Postgraduate Programme Environmental Physics (PEP)

Institute of Environmental Physics (IUP)

University of Bremen, Germany

Acknowledgements

In rigorous order of appearance on the stage of my life...

I would like to thank my parents Elena and Gianandrea and all the members of my family, who constantly supported me along the course of my studies, expressing their partecipation in warm and funny ways.

I would like to thank my classmates from the University of Rome, La Sapienza, and all my friends in Rome for their constant and cheerful presence, even from far away, and for repeatedly asking for the day of my defense, unable to believe that in Germany Master's theses don't get an official defense.

I would like to thank all the teachers, the tutors and the staff of the Postgraduate Programme Environmental Physics at the University of Bremen, for the unrepeatable opportunity they offered me, to get in contact with new and exciting realities, as a scientist and as a citizen of the world. A particular thanks goes to Prof. John Burrows, for teaching me everything a young enthusiast student needs to know about research, and will never find in a textbook.

I would like to thank all the scientists and the students who are working on the MAMap project, and in particular my supervisor Dr. Michael Buchwitz, for guiding and helping me at any time I needed it. A special thanks to Konstantin Gerilowski for giving me the chance to help him in the measurement campaigns, and for all the enthusiasm he gave me when working together.

Finally, I would like to thank my PEP classmates, my unconventional family at Falkenstrasse and all the friends I made in Bremen, older and newer, for being there every time I was about to lose hope and surrender, to warm and cheer me up. This pages would have never been written if not for you.

Abstract

Methane (CH_4) is, after water vapour (H_2O) and carbon dioxide (CO_2), the third strongest radiative forcing factor, responsible of about 18% of the direct radiative forcing due to long-lived greenhouse gases (IPCC-AR4, 2007). The correlation of high atmospheric methane concentrations with past global warming events was made evident by the analysis of the Vostok ice cores by Petit et al., (1999). The current state of the knowledge on atmospheric methane mixing ratios and surface sources and sinks is presented, together with short discussion of global satellite-based measurements and local in-situ observations and their capabilities and limitations (Bergamaschi et al., 2005; Schneising et al., 2008a; Schneising et al., 2008b).

A new approach is presented, using a remote sensing airborne instrument (MAMap), designed to measure mixing ratios of greenhouse gases (CH_4 and CO_2) on a local- and regional-scale to allow estimation of surface fluxes not detectable from space. MAMap is a two-channel airborne NIR/SWIR grating spectrometer, similar to the satellite-borne SCIAMACHY.

In order to retrieve greenhouse gas information from the spectral measurements, radiative transfer and inversion theory is needed and here briefly introduced. The general principles of the Differential Optical Absorption Spectroscopy (DOAS) are presented, together with the specific strong absorption issues that led to the development of the Weighting Functions Modified (WFM) DOAS method (Buchwitz et al., 2000).

An increase of the near surface mixing ratio above the background ($\sim$1750 ppb) of 75-250 ppb is estimated as the detection limit, according to the specifications (3% variation of the lowest 3 km partial CH_4 column), by a simple 1D steady-state model of the atmospheric boundary layer.

The results of the first preliminary analysis of MAMap data are presented, based on three measurement campaigns performed between July 2007 and June 2008. The stability of the detector and spectrometer system throughout several flight days is confirmed, together with the impact of the illumination conditions (season, solar zenith angle, cloud coverage) on the fit precision, assessed using digital image processing statistical techniques (Lillesand and Kiefer, 2000). An initial version of the retrieval algorithm for CH_4 and CO_2 has been applied to the MAMap in-flight measurements. The algorithm is still in its initial stage of development and at present cannot make full use off all MAMap capabilities. For example, the algorithm is limited to total vertical column retrieval. The theoretical signal-to-noise ratios and retrieval uncertainties are calculated, leading to an estimate of 1% CH4 and CO2 total column error for a typical measurement (58 ms exposure time, surface reflectance 0.15).

An anthropogenic CO_2 emission (from the Schwarze Pumpe power plant) is successfully observed and characterized through different averaging techniques.

The results are consistent with the expected MAMap instrument and retrieval algorithm performance.

A natural source of CH_4, the Zarnekow wetland, is analysed with the same technique but focusing on CH_4. To reduce light path related errors, e.g., due to clouds, the ratio between the columns of CH_4 and CO_2 is taken. Some correlation of the CH_4/CO_2 ratio with the land cover (and expected emissions) is observed. The expected reproducibility resulting from repeated measurements on overlapping flight trajectories is confirmed. Further comparison with the ground data will be undertaken in the future providing a better understanding of the target and the quality of the MAMap greenhouse gas product.

No conclusive evidence instead is found, in the data from an artificial methane release experiment, of the capability of MAMap of detecting a small, localized methane source. Further experimentation is advised.

Contents

I Introduction and motivation **11**

1 Introduction **11**

2 Motivation **13**

II Foundations and theory **15**

3 Radiative transfer and inversion theory **15**

3.1 Radiative transfer in the atmosphere 16

3.2 Remote sensing spectrometry 21

3.3 Inverse methods 22

4 The MAMap project **29**

4.1 Technical description of MAMap 29

4.1.1 Operation Modes 30

4.1.2 Pre-flight calibration 33

4.2 The SCIATRAN radiative transfer model . . . 34

4.3 The MAMap WFM-DOAS v.HR-002 algorithm 36

III Results of pre-flight theoretical estimates **39**

5 Methane variability and MAMap capabilities **39**

5.1 Boundary layer structure and atmospheric profiles 39

5.2 Methane column estimate from ground concentrations 40

5.3 Comparison with ground data 42

6 Instrument signal-to-noise and retrieval precision estimates 44
6.1 Noise and random uncertainty 47
6.2 Instrument and retrieval simulation 48

IV Results of a first analysis of in-flight data 53

7 Inter-flight stability from calibration spectra 54
7.1 SWIR Detector Stability 54

8 Fit residua: inter-flight stability and impact of illumination 59
8.1 Inter-flight stability and filtering 59
8.2 Multidimensional analysis and data classification: an example 62

9 An anthropogenic carbon dioxide source: the Schwarze Pumpe coal power plant 69
9.1 Target description 69
9.2 Expected signal strength 70
9.3 Data selection and filtering 71
9.4 Spatial analysis and comparison with ground type information 72
9.4.1 Maximum signal 72
9.4.2 CO_2, CH_4 column factors, ratio CO_2/ CH_4 72
9.5 Transects over the exhaust plume 73

10 A natural methane source: the Zarnekow wetland 86
10.1 Target description 86
10.2 Expected signal strength 88
10.3 Data selection and filtering 90

10.4 Spatial analysis and comparison with ground type information 90
10.4.1 Image manipulation and enhancement . 90
10.4.2 Maximum signal 91
10.4.3 CO_2, CH_4 column factors, ratio CO_2/CH_4 91
10.5 Comparison of repeated overpasses 91

11 An artificial methane source: the Ketzin experiment 104
11.1 Target description 104
11.2 Expected signal strength 104
11.3 Data selection and filtering 105
11.4 Spatial analysis and comparison with ground type information 105
11.5 Time series analysis 105

V Conclusions 112

A Other Targets 114
A.1 COTTBUS (Open Coal Mines) 114
A.2 PAULIN AUE (Wetlands) 114

Part I

Introduction and motivation

1 Introduction

This scientific study is a contribution to a larger project, the Methane Airborne Mapper (MAMap) project, started in 2005 as a cooperation between the Institute of Environmental Physics (IUP) at the University of Bremen and the Helmholtz Centre Potsdam - German Research Centre for Geosciences (GFZ). The overall goal of the project is to provide a new tool, an airborne hyperspectral infrared remote sensor, the first of its kind to measure the concentration of the greenhouse gases methane and carbon dioxide at a local and regional scale. As a matter of fact, currently available satellite-based instruments like SCIAMACHY can provide global datasets for these greenhouse gases, but with a resolution of several tens of kilometers. Ground-based measurement systems like the NOAA/CMDL global cooperative air sampling network or the German Umweltbundesamt operational network instead can provide stable and accurate data time series, but only locally, resulting in a sparse global coverage. MAMap is designed as a bridge between these two approaches, to provide valuable additional information on the strength of GHG sources and sinks.

The MAMap project is still at an early phase, and the focus is on testing the instrument in real flight conditions, assessing the hardware capabilities and the sensitivity of intermediate retrieved products to variations in the gases to be measured. In this context, this work addresses the question whether the instrument is working as specified and if it is effectively capable of detecting relative variations of methane in natural and artificial conditions. The answer then needs the collection of knowledge in different fields, from the distribution of greenhouse gases and the carbon cycle (Part I) to the understanding of the theoretical background to the measurement (Part II). With this theoretical equipment, the investigation can be divided on two sides: on one side, the theoretical detection capability, given the instrument specifications and the known range of natural variations can be estimated prior to any actual flight. In Part III a simple atmospheric boundary layer steady-state model is presented, to estimate the expected strength of a methane variation signal, and the theoretical sensitivity of the instrument is calculated, through estimates of the different noise sources. On the other side, the effective instrument performance can be assessed by the analysis of the in-flight retrieved products (Part IV). Such products are the relative variation in the vertical column of CH_4 and CO_2, and the ratio between them, as retrieved through an initial inversion algorithm. The data is then analysed both in the time domain, as a time series along the flight track, and in the space domain, as a two-dimensional field. Part V then summarizes the conclusions of the analyses of Sections 5 to 11.

Dipl. Phys. Konstantin Gerilowski (IUP) and Dr. Andreas Tretner (GFZ) designed, built and operated the instrument in three measurement campaigns between 2007 and 2008. Dr. Michael Buchwitz (IUP) wrote the inversion algorithm, based on his experience on SCIAMACHY. Dr. Heinrich Bovensmann (IUP) provided organizational support for every phase of the project and Prof. Jürgen Augustin (ZALF) coordinated the joint measurement campaign on the Zarnekow site. Dr. Carsten Lindemann (FU Berlin) piloted the Cessna that carried MAMap in the three measurement campaigns based in Berlin. Dr. Lars Kutzbach (Ernst Moritz Arndt University Greifswald) provided the data from the eddy-covariance measurements at Zarnekow.

Note

This Master Thesis is based on the previous Thesis Paper with the same name, submitted by the author in February 2008 at the University of Bremen. Parts I and II are an expanded and corrected version of that text, amended to answer the comments of the examiners. Parts II to V are completely new material, presenting the results of original research work.

As stated in the Introduction, the focus of the research has slightly changed from what had been proposed in the Thesis Paper. In the first plan the main aim was in analyzing and improving the retrieval algorithm by integrating more sources of data and better a priori assumptions. This work instead used the retrieval algorithm as it was (with changes to integrate with improved instrument software and allow a high-resolution analysis), and used the results together with different tools to have a more complete characterization of the different target scenes.

2 Motivation

Our planet, the Earth, continuously keeps a balance with the energy coming from the Sun. The atmospheric greenhouse effect determines the amount of energy trapped in the system as opposed to the amount emitted or reflected back to space. The available energy, in turn, determines the climatic state, so land and ocean temperatures, rainfall, ocean level, ice cover.

Gases like water vapour (H_2O), carbon dioxide (CO_2) and methane (CH_4) produce this greenhouse effect by absorbing infrared radiation. The relative impact of each of these greenhouse gases (GHG) is different, with CH_4 20 times more effective than CO_2 (Wallace and Hobbs, 2006). If methane accounts for 20% only of the overall greenhouse radiative forcing this is primarily because of the different atmospheric mixing ratios: 380 ppm on average for CO_2 and 1.75 ppm on average for CH_4. Due to human activities, the global mixing ratios of CO_2 and CH_4 have risen to levels never recorded in the last 650,000 years (Forster et al., 2007), and keep rising. The analysis of the ice core records, since the drilling at the Vostok station in Antarctica, is the most important evidence of a positive correlation between GHG mixing ratios and surface temperature throughout the Earth's climate history (Petit et al., ,1999;Brook, 2005). Therefore, to predict future climate changes caused by the enhanced greenhouse effect and to assess the magnitude of anthropogenic impact it is necessary to characterize the global distribution of these two gases' sources and sinks.

While the global biogeochemical cycle of the element carbon is reasonably well known, with the regional sources and sinks of carbon dioxide (Baker, 2007), the sources and sinks of methane are still subject to great uncertainties (Lowe, 2006; Lelieveld, 2006). Lowe (2006) reports that almost 2/3 of all CH_4 emissions are anthropogenic (from rice and cattle farming, fires, fossil fuel burning and landfills), and the models presented by Bousquet et al. (2006) suggest that anthropogenic emissions from fossil fuels, thought being stable, have kept rising since 1999.

The observation by Severinghaus et al. (1998) that the CH_4 mixing ratio rise at the end of the Younger Dryas interval follows the temperature rise by 0-30 years leads to think that a positive feedback climate mechanism could be based on methane. Three natural CH_4 sources, more or less clearly understood, could prove to be each a separate positive feedback mechanism on climate. The strongest known natural source of CH_4 is bacterial decomposition in wetlands, accounting for 20-40% of the total emissions. As shown in the models by Walter et al. (2001), the feedback potential is very strong (a temperature increase of 1°C leads to a 20% increase in CH_4 emissions). The second possibility comes from the very recent, and highly debated, discovery of the methane production by living plants in aerobic conditions (Keppler et al., 2006), combined by the observations by SCIAMACHY onboard the European satellite ENVISAT of high CH_4 levels at the tropics not explained by current models (Frankenberg et al., 2005a; Buchwitz et al., 2005). Methane emission from plants could be responsible of 10-30% of the total emission, and would be as well subject to positive climate feedback due to the influence of temperature on vegetation growth. Walter et al. (2006) discovered another natural CH_4 source poorly accounted in the models, namely the emission from thawing permafrost areas in Northern Siberia, estimated as 70% of the total CH_4 increase in the northern region.

The main sink process for CH_4 is the chemical destruction by hydroxyl radicals (OH), which produces the pollutant gas ozone (O_3) and influences the main tropospheric chemical cycles. Since both sources and sinks are located in the lower troposphere, and the chemical lifetime of CH_4 is nearly a decade, most of atmospheric methane is well-mixed zonally and confined in that altitude range. While the difference in the mixing ratio between the two hemispheres amounts to 10% of the total average mixing ratio, temporal variability, like the seasonal cycle, and local spatial variability amounts only to 3%, and as such is difficult to observe using satellite-borne systems. The only instrument currently able to observe the CO_2 and CH_4 signal from the lower stratosphere on the global scale is SCIAMACHY, but with a low spatial resolution (30 x 60 km). Currently the SCIAMACHY dataset is being compared with results of methane cycle inverse models, which in turn must be based on local or regional scale data for validation. Examples are the wetland climatic and hydrological model from Walter et al. (2001) and the chemical and meteorological model from Bousquet et al. (2006). These are currently initialized with local scale data coming from ground stations, which offer high accuracy and time persistance, but sparse spatial coverage, or ground-based campaigns like TROICA, which measured mixing ratio levels of both polluted and natural background areas through the Trans-Siberian railroad (Oberlander et al., 2002; Belikov et al., 2006), covering a wide area but for a time frame limited to the measurement campaigns.

An instrument able to cover systematically large areas, with a spatial resolution on the order of hundreds of meters then could prove of great importance to better relate global-scale and local-scale measurements. The MAMap project, presented in 4, was designed to bridge this gap.

Part II

Foundations and theory

In order to retrieve greenhouse gas information from the spectral measurements, the knowledge in several fields is needed. The theory of radiative transfer in the atmosphere is presented in Section 3.1, based on Schneising (2008). Remote sensing spectrometers and sensors are described in Section 3.2, after von Savigny (2007). Finally, the the algorithms to extract the information contained in remote sensing measurements (inverse methods) are discussed in Section 3.3, based on Rodgers (2000), Schlitzer (2006), Richter (2007) and Buchwitz et al. (2000).

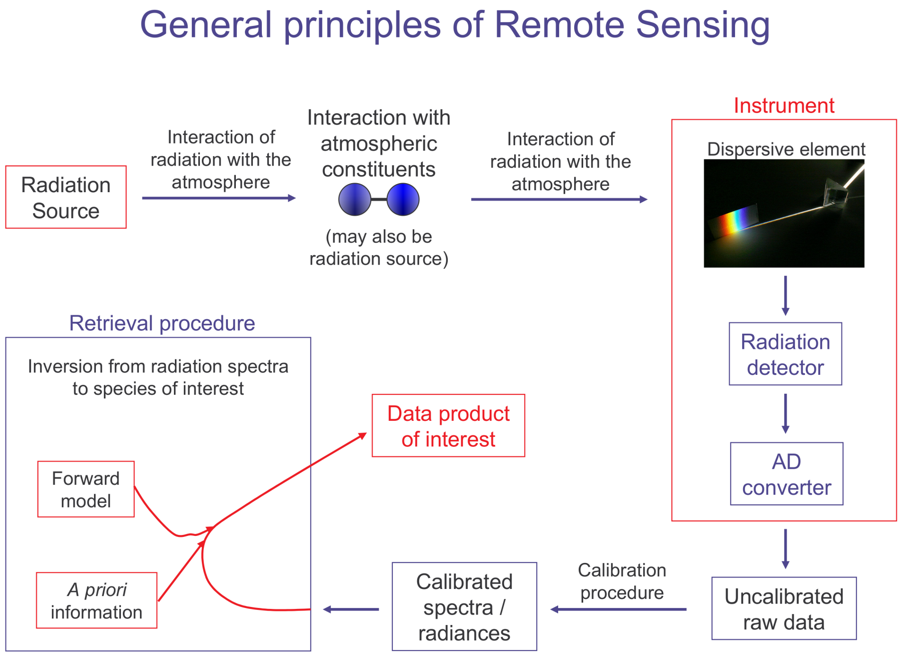

Figure 1: General principles of remote sensing. From von Savigny (2007).

3 Radiative transfer and inversion theory

Remote sensing is the technique of measuring physical quantities without being in direct contact with the object measured, by analyzing the changes that an external probe, for example electromagnetic radiation, undergoes when it interacts with the object. It is an extremely important tool for atmospheric and climate research, an irreplaceable complement to the collection of in-situ samples.

Its most important advantages are that it makes possible to measure in areas otherwise difficult to access, that most instruments can be fully automated, so to allow the collection of long time series, and the coverage of large regions, that the analysis of the measured radiation provides information on several different physical quantities at the same time, and finally that large amounts of data can be collected with less financial and logistic effort than it would be possible otherwise.

On the other side, remote sensing has many limitations that need to be taken into account. It allows, in fact, only indirect measurements. This means that several processes and factors concur to affect the probe, for example interacting with the radiation that gets measured. For this reason, it is not possible to accurately interpret the measurements without the help of additional assumptions and models. And on the other side to accurately validate the data, that is to relate it univocally to measurements performed in a laboratory is often very difficult, when possible at all. An accurate estimate of the uncertainties of such measurements requires then an extensive work.

3.1 Radiative transfer in the atmosphere

Electromagnetic radiation is useful for atmospheric remote sensing because of the properties of its interaction with matter. Many processes affect the radiative transfer through the atmosphere: direct photon absorption by atoms and molecules, elastic and inelastic scattering by molecules and aerosols, stimulated and thermal emissions, and geometric reflection by macroscopic surfaces. All of these effects depend on the radiation wavelength, and this allows to separate them and to identify the different components involved. The near-infrared region of the electromagnetic spectrum, for example, is susceptible to absorption by molecules leading to a change in their rotational-vibrational modes. This gives to every different species its own absorption spectrum, that can be recognized, and whose amplitude is related to the quantity of the absorbers that interacted with the radiation.

Molecular absorption The absorption of a molecule is described by its absorption cross-section k_λ exhibiting unique spectral signatures characteristic for the respective molecule. In general the absorption cross-section depends on pressure and temperature. Its product with the concentration n of the molecule is referred to as the absorption coefficient α_λ whose integration along the finite light path gives the corresponding optical density τ. Following Beer-Lambert's law,

$$L_\lambda(s) = L_{\lambda 0}(s) \exp\left(-\int_{s_1}^{s_2} k_\lambda(s)\, n(s)\, ds\right) \tag{1}$$

the monochromatic radiance L_λ decays exponentially with respect to τ neglecting other absorbers, scattering and surface reflection.

Rayleigh and Raman scattering Rayleigh scattering describes the elastic scattering of electromagnetic radiation by a volume of molecules or particles with microscopic density fluctuations due to thermal motion whose size is very small compared to the wavelength of the incident radiation ($2\pi r \ll \lambda$). It therefore applies to scattering of solar radiation by air molecules. The Rayleigh scattering phase function normalised to 4π which describes the angular distribution of the scattered light is given by

$$\varphi_R(\vartheta) = \frac{3}{2}\frac{(1+d)+(1-d)\,cos^2\vartheta}{2+d} \tag{2}$$

with scattering angle ϑ and depolarisation factor d. The Rayleigh scattering coefficient σ_R which is obtained by multiplication of the Rayleigh scattering cross-section and the air density $n(p,T)$ is proportional to λ^{-4}. This, by the way, is the reason why the sky is blue during the day: light with shorter wavelengths gets scattered more by the air molecules.

A small fraction of the solar radiation is also scattered inelastically by Raman scattering resulting in less deep Fraunhofer lines in scattered solar radiation compared to the direct sun light spectrum. This Raman filling-in of spectral lines is known as the Ring effect.

Aerosol extinction "Aerosol" is an expression that refers to airborne liquid droplets, particulate matter (PM), or combinations of these, that exhibit typical radii between 0.01 µm and 10 µm. Besides natural occurrences, about 10% of the total amount of aerosols in the atmosphere is of anthropogenic origin. The main contribution of aerosols to radiative transfer in the solar spectral region is scattering. Apart from desert dust, soot, and volcanic ash, absorption of aerosols generally only plays a minor role.

The scattering of spherical aerosols comparable in size with the wavelength of incident radiation ($2\pi r \approx \lambda$) is well described by Mie theory. In contrast to the Rayleigh scattering coefficient the aerosol extinction coefficient κ_A cannot be derived analytically due to the complex dependencies between the involved microphysical parameters and the variety of shapes and composition of the aerosol particles. As a first approximation, the aerosol extinction coeficient can be estimated proportional to λ^{-a} with typical Ångstrom exponent $a \in [0,\ 1.5]$ depending on the wavelength range and aerosol scenario considered.

The angular distribution of the scattered light is described by the aerosol scattering phase function φ_A, which depends on the aerosol type and usually shows a complex dependence on the scattering angle and wavelength. However, it generally has a strong forward peak and is often parametrised by the Henyey-Greenstein

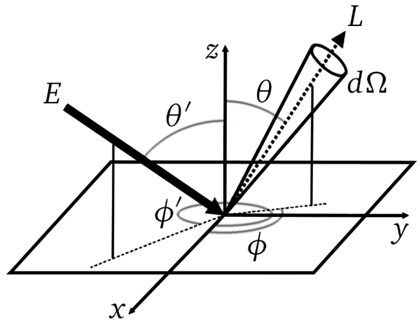

Figure 2: Reflection directions and angles.

approximation (normalised to 4π)

$$\varphi_A(\vartheta) = \frac{1 - g^2}{\left(1 + g^2 - 2g\cos\vartheta\right)^{\frac{3}{2}}} \tag{3}$$

with the asymmetry factor $g \in [-1, 1]$, that defines how strong and in which direction is the peak of the phase function. For $g = 0$ the scattering is isotropic. For cloud particle scattering ($2\pi r \gg \lambda$) the scattering coefficient σ_C is approximately constant with wavelength, as can be seen by the fact that clouds have no color, but reflect all of them in the same way.

Surface reflection Given a reflecting surface illuminated by a light source under the zenith angle θ', the ratio of reflected radiant flux density (the radiance L integrated over the semi-sphere) to incident radiant flux density (irradiance) $E = E_0 \cos\theta'$ defines the albedo of the surface

$$\rho = \frac{1}{E} \int_{2\pi} L \cos\theta d\Omega \tag{4}$$

where Ω is the solid angle and θ the angle between the reflection direction and the normal to the surface (Figure 2). Hence, albedo is the fraction of incident radiation that is reflected by a surface, with $\rho \in [0,\ 1]$ being a dimensionless quantity. In case of a Lambertian surface, the reflected radiance L is isotropic and therefore independent of the viewing geometry which simplifies the relation to

$$\rho = \frac{L}{E} \int_{2\pi} \cos\theta d\Omega = \frac{\pi L}{E} \tag{5}$$

The albedo is characteristic for a particular material and usually depends on wavelength for natural surface types (e.g., see Figure 12).

In the general case of a non-Lambertian surface the reflection can be described by a Bidirectional Reflectance Distribution Function (BRDF) $\tilde{\rho}(\theta', \phi', \theta, \phi)$, dependent on the direction of incident and reflected radiation.

Radiative transfer equation The radiative transfer equation in its most general form describes the change in radiance (radiant flux per area and solid angle in a given direction)

$$L = \frac{d^2\Phi}{\cos\theta d\Omega dA} \tag{6}$$

in an infinitesimal path element ds along the direction $\vec{s}$ in the atmosphere

$$dL_\lambda = \kappa_\lambda \left[J_\lambda\left(\vec{s}, L\right) - L_\lambda\left(\vec{s}\right)\right] \tag{7}$$

The extinction coefficient κ_λ is the sum of the absorption coefficient α_λ and the scattering coefficient σ_λ, while J_λ denotes the so-called *source function* which can be splitted in two terms, the scattering source function J_{sc} and the emission source function J_{em}.

Thus, the radiative transfer equation, which completely defines the radiance for specified boundary conditions, describes the loss of photons due to absorption along the light path or scattering out of the beam and the gain caused by local sources or scattering into the beam. Introducing the single scattering albedo

$$\omega = \frac{\sigma}{\kappa} \in [0, 1] \tag{8}$$

the scattering source function is obtained from the phase function φ by

$$J_\lambda^{sc}\left(\vec{s}, L\right) = \frac{\omega_\lambda}{4\pi} \int \varphi_\lambda\left(\vec{s}, \vec{s'}\right) L_\lambda\left(\vec{s'}\right) d\Omega' \tag{9}$$

Although being generally more complex, in case of local thermodynamic equilibrium the emission source function is given by

$$J_\lambda^{em} = \left(1 - \omega_\lambda\right) L_\lambda^B\left(T\right) \tag{10}$$

where $L_\lambda^B\left(T\right)$ is the black-body radiance at temperature T . Hence, the emission source function is independent of the direction $\vec{s}$ in this case.

If source terms are negligible ($J_\lambda = 0$), Eq. 7 reduces to

$$\frac{dL_\lambda}{L_\lambda} = -\kappa_\lambda ds \tag{11}$$

giving Beer-Lambert's law

$$L\left(s\right) = L_0 e^{-\tau(s)} \quad , \quad \tau\left(s\right) = \int_{s_1}^{s_2} \kappa\left(s\right) ds \tag{12}$$

that describes the exponential attenuation of incoming radiation L_0 due to extinction with τ being the slant optical density of the atmosphere corresponding to the given finite light path.

3.2 Remote sensing spectrometry

The practical way to measure the radiation transmitted through the atmosphere at different wavelengths is by separating the different spectral components using a dispersing element. Due to its elevated resolving power and its stability, the diffraction grating is the most common dispersing element used in atmospheric spectroscopy, together with Fourier Transform spectroscopes.

A grating is a reflecting or transmitting surface carved with several (n) grooves called *rules*, each of them independently diffracting light, at a distance g from each other. The different light waves coming from the different grooves then interfere with each other, and their interference maxima occur at angles α such that

$$\sin\alpha = \frac{m\lambda}{g} \tag{13}$$

where m is a whole number, the *diffraction order*. At different dispersion angles α then different wavelengths λ will have their interference maxima, and can then be dispersed on a surface.

Several detectors can be used then, to measure the dispersed radiation at different wavelengths, for example the photodiode array and the couple-charged device. A photodiode array is a linear detector formed by a series of adjacent photodiodes, that is semiconductor diodes with a surface exposed to the incoming photons. There are two kinds of photodiode arrays. In the first one, when photons are absorbed by the detector, they create an electron-hole pair that drifts to the next p-n junction and discharges it. After a time interval, called *exposure time*, the detector is read out by sequentially charging the capacitors corresponding to each pixels, and the current needed is proportional to the number of photons absorbed in the exposure time. The second kind instead works by having the junctions depleted of charge, and then measuring the current produced when the electrons created by photon absorption are read out. There are photodiode arrays with 256 to 2048 pixels, allowing to measure several wavelenghts at the same time.

Another kind of radiation detector that can measure several wavelengths is the charge-coupled device or CCD. It is a two-dimensional array of detector pixels (with size ranging from 256 to 4096 per each side), also exploiting the properties of semiconductors. When photons hit one of the pixels, the resulting electrons are collected in the corresponding uncharged depletion zone. The readout then consists in shifting the charges sequentially from row to row. The lowest row is then readout and digitized. The main advantages of this kind of detectors are the high sensitivity to radiation and its 2D shape, that allows to measure several wavelengths, on one axis, coming from different viewing angles, on the other axis, effectively creating a multispectral imaging sensor. A drawback is that the capacity of the single pixels is lower than that of other sensors, so shorter exposure times are needed not to fill the holes with electrons (saturate). Moreover, a long time is needed to read out sequentially each different pixel, that can last up to several seconds.

3.3 Inverse methods

Airborne spectroscopic measurements, like all remote observations, are inherently indirect measurements, that is the physical properties of the observed object (in our case, the atmosphere), must be inferred from other measured quantities. This inference is often complex, and belongs to the class of problems called *inverse problems.* Rodgers (2000) defines them as:

> the question of finding the best representation of the required parameter given the measurements made, together with any appropriate prior information that may be available about the system and the measuring device.

The general inverse problem can be regarded as a question of setting up and solving a set of simultaneous linear or non-linear equations, in the presence of experimental error of some of the parameters, the *measurements*, and quite possibly in the presence of approximations in the formulations of the equations.

The quantities to be retrieved can be represented by a state vector $\vec{x}$, with n elements $x_1, x_2, ..., x_n$. It could represent a profile of some quantity given at a finite number of levels, or any set of relevant variables, such as coefficients for another representation, or decomposition of the profile itself, or again, as in the case of MAMap, it may include a range of different types of parameters, like the vertical profile scaling parameter of different gases, a temperature profile shift, and polynomial coefficients for the low-frequency spectrum.

The quantities actually measured in order to retrieve $\vec{x}$ can be represented by a measurement vector $\vec{y}$, with m elements $y_1, y_2, ..., y_m$. This vector should include all the quantities measured that are functions of the state vector. Measurements are made to a finite accuracy; random error or *measurement noise* will be denoted by the vector $\vec{\epsilon}$.

For each state vector there is a corresponding ideal measurement vector $\vec{y}_{mod}$, determined by the physics of the measurement. The physical details are approximated by a *forward model* $\vec{F}(\vec{x})$, so that

$$\vec{y} = \vec{F}(\vec{x}) + \vec{\epsilon} \tag{14}$$

To construct a forward model we must of course understand how the quantity measured, that is the absorbed solar infrared radiation, is related to the quantity that is really wanted, in this case the vertical column of CO_2 or CH_4.

The quantities to be retrieved in most inverse problems are continuous functions, while the measurements are always of discrete quantities. Thus most inverse problems are formally ill-posed or underconstrained in this trivial sense. This is simply dealt with by replacing the truly continuous state function, corresponding to an infinite number of variables, with a representation in terms of a finite number of parameters. After discretisation the problem may or may not be underconstrained, depending on the information content of the measurement.

Linear least-squares method The simplest way to address a problem is to start with its linear form. A linearisation of the forward model about a reference state $\vec{x}_0$ is adequate provided that $\vec{F}(\vec{x})$ is linear within the error bounds of the retrieval. When we write

$$\vec{y} - \vec{F}(\vec{x}) = \left.\frac{\partial \vec{F}(\vec{x})}{\partial \vec{x}}\right|_{\vec{x}_0} (\vec{x} - \vec{x}_0) + \vec{\epsilon} = \mathbf{K}(\vec{x} - \vec{x}_0) + \vec{\epsilon} \tag{15}$$

we define a $m \times n$ weighting function matrix $\mathbf{K} = \partial \vec{F}(\vec{x}) / \partial \vec{x}$, not necessarily square, in which each element is the partial derivative of a forward model element with respect to a state vector element. If $m < n$ the equations are described as underconstrained (or ill-posed or under-determined) because there are fewer measurements than unknowns. Similarly if $m > n$ the equations are often described as overconstrained or over-determined, as long as all the equations are linearly independent, and carry enough independent information.

The term *weighting function* is peculiar to the atmospheric remote sensing literature, and it arised because in the early applications of nadir sounding for temperature the forward model takes the form of a weighted mean of the vertical profile of the Planck function.

For a fundamentally overconstrained problem, like that of the MAMap retrieval, where the measurement vector has considerably more elements than the state vector, and the algebraic form of the model is known from sound physical reasoning, an appropriate approach is the *least-squares method.*

In the case where there are more measurements than unknowns, an exact solution is not possible in general. Therefore we look for a solution that minimises the sum of the squares of the differences between the actual measurements and those calculated from the forward model using the solution. That is, we minimise:

$$\left[\vec{y} - \vec{F}(\vec{x})\right]^{\mathbf{T}} \left[\vec{y} - \vec{F}(\vec{x})\right] \quad or \quad (\vec{y} - \mathbf{K}\vec{x})^{\mathbf{T}} (\vec{y} - \mathbf{K}\vec{x}) \tag{16}$$

In the linear case a derivative with respect to $\vec{x}$ leads immediately to the normal equations:

$$\hat{x} = \mathbf{G}\vec{y} = \left(\mathbf{K^T K}\right)^{-1} \mathbf{K^T}\vec{y} \tag{17}$$

where $\mathbf{G}$ is the approximate inverse of $\mathbf{K}$.

If the measurement error $\vec{\epsilon}$ is known, it must be taken into account by weighting both the model and the measurement vectors by it, so that the resulting system of linear equation is balanced:

$$y_i = \sum_j K_{ij} x_j + \sigma_{y_i} \Rightarrow \frac{y_i}{\sigma_{y_i}} = \frac{1}{\sigma_{y_i}} \sum_j K_{ij} x_j + 1 \tag{18}$$

where $i \in [1, m]$, $j \in [1, n]$ and the σ_{y_i} are the errors on the single measurements, the elements of $\vec{\epsilon}$. Then a covariance matrix $\mathbf{cov}\left(\vec{y}\right)$ could be defined, that if the measured quantities are completely independent of each other will have the form $\mathbf{cov}\left(\vec{y}\right) = \mathbf{I}\vec{\epsilon}$, otherwise in general

$$\mathbf{cov}\left(\vec{y}\right) = \begin{pmatrix} \sigma^2_{y_1} & \sigma^2_{y_2,y_1} & \cdots & \sigma^2_{y_m,y_1} \\ \sigma^2_{y_1,y_2} & \sigma^2_{y_2} & & \vdots \\ \vdots & & \ddots & \\ \sigma^2_{y_1,y_m} & \cdots & & \sigma^2_{y_m} \end{pmatrix} \tag{19}$$

where $\sigma^2_{y_i}$ is the variance on the i-th measurement and and $\sigma^2_{y_i,y_j}$ the covariance of the i-th and the j-th measurement. The errors of the retrieved variables σ_{x_i} then can be easily calculated by the covariance matrix of the unknowns $\mathbf{cov}\left(\vec{x}\right)$, that is

$$\mathbf{cov}\left(\vec{x}\right) = \mathbf{G} \cdot \mathbf{cov}\left(\vec{y}\right) \cdot \mathbf{G^T} \tag{20}$$

In the case instead that there is no information on the uncertainties of the single measurements σ_{y_i}, the uncertainties on the parameters σ_{x_i} can still be estimated following Press et al. (1992). The covariance matrix of the unknowns $\mathbf{cov}\left(\vec{x}\right)$ expresses the dependence of each parameter x_j from the forward model, and it can be shown that it is equal to

$$\mathbf{cov}\left(\vec{x}\right) = \left(\mathbf{K^T K}\right)^{-1} \tag{21}$$

The relative weight of the error on any single parameter x_j is then proportional to the j-th element of the diagonal of the covariance matrix. To take into account instead the overall uncertainty on the parameters coming from the approximation of the least-square fit, they can be weighted by the fit residuum

$$\sigma^2_{x_j} = cov\left(\vec{x}\right)_{jj} \frac{\left\|RES\right\|^2}{m-n} \tag{22}$$

divided by $m - n$ that is the number of degrees of freedom. The fit residuum is defined as:

$$\|RES\|^2 = \sum_i \left(y_i - \sum_j K_{ij} x_j \right)^2 \tag{23}$$

This is the method used in the WFM-DOAS fit and in the preliminary MAMap retrieval algorithm, where the uncertainty on the measurements from each single spectral pixel is not estimated with sufficient accuracy.

Differential optical absorption spectroscopy One special method for the remote sensing of atmospheric trace gases in the atmosphere is the so-called *differential optical absorption spectroscopy* or DOAS. Its main difference from other measurement methods based on absorption spectroscopy in the infrared wavelength range is that, to avoid problems with extinction by scattering or changes in the instrument throughput, only signals that vary rapidly with wavelength are analysed (thus the differential in DOAS). The other, broadband structures - that are e.g. caused by a changing cloud cover and that are difficult to quantify - are approximated by a polynomial. Therefore, only those species can be observed that show significant and structured absorption in the near infrared wavelength range, such as CO_2, CH_4, H_2O, and CO. Unlike other techniques such as ozone sondes, LIDAR measurements or microwave radiometry, DOAS measurements provide little information on the vertical profile of the absorbers but rather the integrated column in the atmosphere. This disadvantage is compensated by the simplicity of the experiment and the relatively large number of species that can be measured simultaneously.

Figure 3, as an example, illustrates the procedure for a spectral measurement of Earth-reflected solar radiation. The Earth-reflected spectrum I_λ is first divided by the solar spectrum measured at the top of the atmosphere $I_{\lambda 0}$, to eliminate the structures of the solar spectrum itself, like the Planck blackbody shape and the Fraunhofer lines. The second step is to fit a low-order polynomial $P(\lambda)$ to the logarithm of the resulting spectrum, and divide the logarithm by the polynomial. The resulting differential absorption spectrum I^d_λ then contains only variation on the same order of the absorption by the trace gases of interest. They can be separated as a linear combination of the absorption spectra of the different species i :

$$\ln I^d_\lambda = \frac{1}{P(\lambda)} \ln \left(\frac{I_\lambda}{I_{\lambda 0}} \right) = \sum_i \alpha_{\lambda i} c_i \tag{24}$$

where $\alpha_{i\lambda}$ is the absorption cross-section of the gas i and c_i a linear coefficient proportional to the quantity of absorbers along the light path. Figure 4 is an example of a differential spectrum from a MAMap CH_4 measurement. The quantity of the different absorbers (in this example methane, carbon dioxide and water) is estimated with a least-squares fit, and their sum results in the differential spectrum, plus a difference called *residuum*.

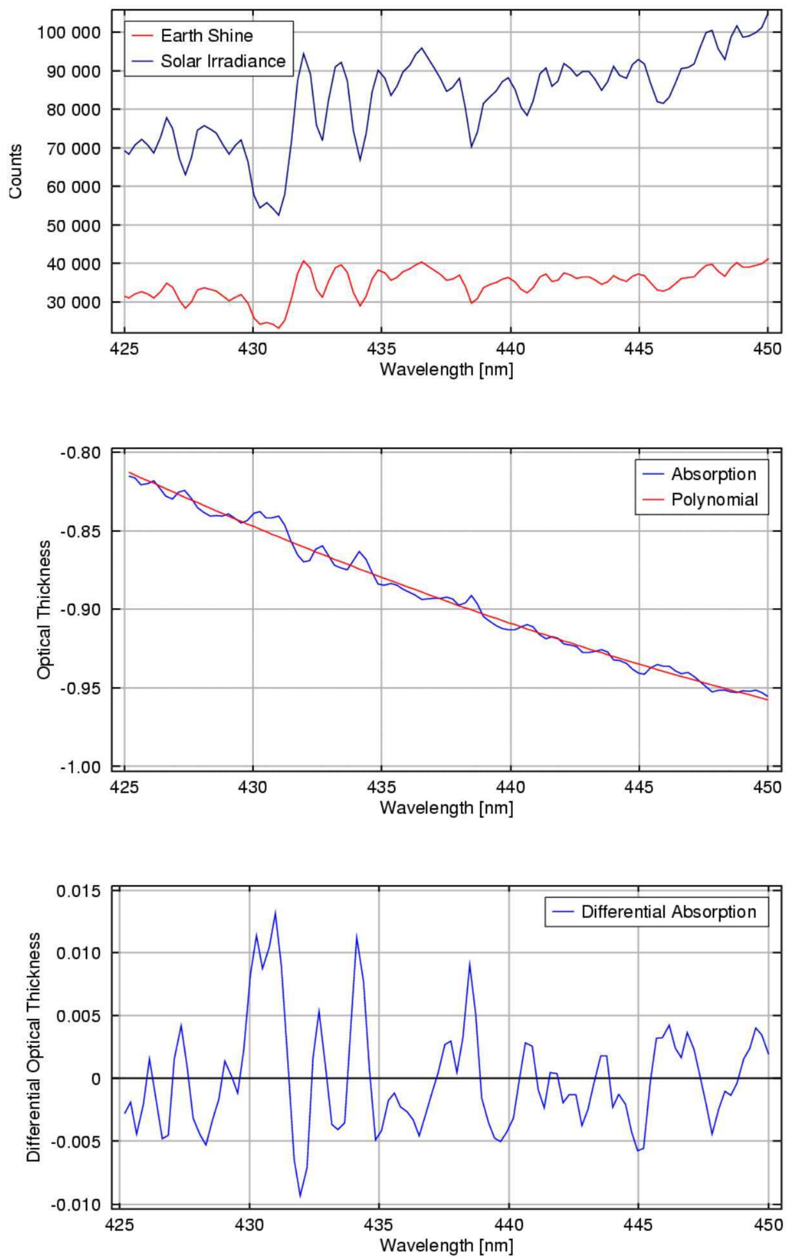

Figure 3: Structure of a DOAS fit: the measured Earth-reflected spectrum (”Earth-shine”) is divided by the solar emission measured at the top of the atmosphere (first panel). The resulting atmospheric absorption spectrum is divided by the low-order polynomial (second panel). The third panel then shows the differential absorption spectrum, that is the high-frequency variations that contain te trace gas spectra. Courtesy of Dr. Andreas Richter (IUP, University of Bremen).

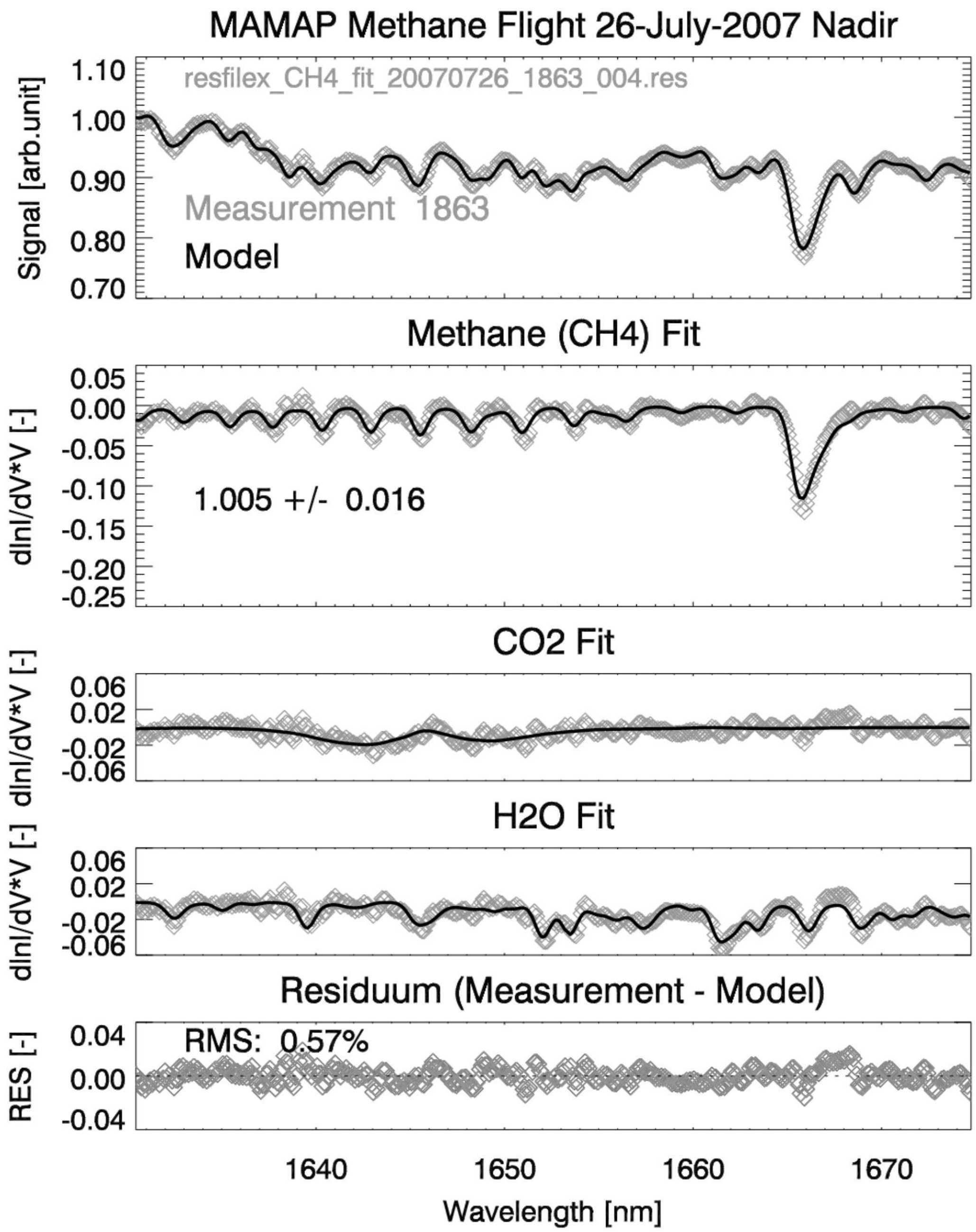

Figure 4: Structure of a MAMap WFM-DOAS fit in the spectral region used for the retrieval of the methane profile scaling factor: the measured spectrum is modelled as the sum of the contributions of the different absorbers. Courtesy of Dr. Michael Buchwitz (IUP, University of Bremen).

4 The MAMap project

The Methane Airborne Mapper (MAMap) project has been developed to provide information on the mixing ratios of CH_4 and CO_2 on an intermediate scale between ground-based local measurements and satellite-based global datasets. These greenhouse gases have physical properties that make them particularly suited to be detected by remote sensing from an airborne passive spectrometer.

First, the sources and sinks for these gases are located at the Earth surface, and the greatest spatial variations take place in the atmospheric boundary layer, that is in the lowest 1000m. Instead from the free troposphere above the vertical profile is almost constant in space and time. This means that most of the variability can be observed by an instrument carried by a small plane.

Second, CH_4 and CO_2 molecules absorb strongly the sunlight in the shortwave infrared (SWIR) spectral region. For this reason, the sunlight reflected by the Earth surface can be used as a source for a passive spectrometer. Moreover, by measuring alternately in zenith- and nadir-looking geometry it is theoretically possible to distinguish the contribution to the absorption due to the gas amount present directly under the plane from the absorption along the light path through the entire atmosphere. This light path could have a complex geometry due to multiple scattering by air moleules and the effect of clouds, aerosols and different surface albedos. In order to minimize the influence of those factors, the mixing ratio of oxygen (O_2) is also measured and used as a constant reference, since it is well-mixed at every location.

The ratio between the column number density of absorbing gas and the column number density of dry air (referred to as dry column mixing ratio) can be then retrieved from the detected spectra using a differential optical absorption spectroscopy (DOAS) inversion algorithm.

4.1 Technical description of MAMap

The MAMap instrument is a two-channel airborne NIR/SWIR grating spectrometer. Both channels have separate optics for zenith- and nadir-looking, and a fold-mirror allows to change between the two operating modes. The instrument can be installed in an airplane with a down-looking window for the nadir telescopes, and light can be fed to the zenith telescopes with diffuser plates and optical fibers.

The first channel (SWIR) is designed to detect the absorption lines of CO_2 (1590-1620 nm) and CH_4 (1630-1750 nm). The detector is an InGaAs linear photodiode array, with 1024 pixels, 25.6 mm long. Due to the dispersive properties of the optics this channel has an overall effective spectral resolution of 0.76 nm. The detector is cooled with liquid nitrogen to an operating temperature of -120°C, to strongly reduce the detector dark current. The signal-to-noise ratio varies then between 1000 (over land, albedo 0.18) and 350 (over water, albedo 0.01), when 10 single spectra are coadded for an overall exposure time of 1 s. The instantaneous field of view (IFOV) of the SWIR channel is 1.34° cross-track (CT) and 0.02° along-track (LT). For nominal flight parameters (altitude 1000 m, speed 200 km/h) and detection times (800 ms, albedo 0.18) the ground-projected IFOV is 25 m (CT) x 45 m (LT).

The second channel (NIR) is calibrated on the absorption line of O_2 in the near infrared spectral range at 760 nm. To make sure that both channels observe exactly the same ground scene, this channel is equipped with a two-dimensional detector, that produces a cross-track image of the ground (pushbroom imaging spectrometer). Since the NIR IFOV is 5.85° CT and 0.072° LT, it is more than 4 times wider, in CT direction, than the SWIR IFOV. Optimal co-alignment between the two channels is then possible by choosing, during the data analysis process, the right portion of the NIR window. An accurate matching of the ground-projected fields-of-view has not yet been implemented.

The 2D-detector is a frame transfer (FT) CCD, with 85 (binned) pixels on the imaging axis, and 256 (binned) pixels on the spectral axis. Due to the grating optical parameters, the spectral window detected is approximately 17 nm, with a spectral resolution of 0.4 nm. The signal-to-noise ratio obtained during test measurements is greater than 850 for a single imaging pixel, and greater than 4000 after 21 imaging pixels are averaged for the alignment with the SWIR channel.

The spectrometer system is integrated by an auxiliary device system called Observer, that provides information about the position of the aircraft and the ground scene during the measurement: a GPS positioning system provides accurate latitude, longitude and altitude measurements; a triaxial gyro sensor records the orientation of the aircraft; a digital imaging interlined CCD camera coaxial to the spectrometer captures visible images of the ground scene, which can be used to extract information about surface spectral reflectivity, vegetation biotype, cloud cover.

Both the spectrometer system and the Observer are activated by the same trigger signal to obtain optimal synchronicity. Three autonomous processing units manage the data readout and storage for the main subsystems (SWIR channel, NIR channel, Observer).

4.1.1 Operation Modes

Nadir-looking and zenith-looking The main goal of the instrument is to measure the concentration of greenhouse gases below the aircraft. This is performed by measuring the radiation emitted by the Sun and reflected by the surface of the Earth. The radiation, in fact, carries the information on the total number of molecules of each absorber it met along its path (called *light path*) from the top of the atmosphere

Table 1: MAMap instrument technical specifications and nominal performance.

	CH_4/CO_2	O_2-A	
Focal Length:	300 mm	80 mm	
Detector Type:	Focal Plane Array (FPA) detector	Charge Coupled Device (CCD)	
Cooling system:	Liquid nitrogen	Thermoelectric	
Number of pixels:	1024	512 x 512 (256 x 85 binned)	
Spectral Range:	1590 - 1690 nm	755 - 785 nm	
Spectral Resolution:	0.76 nm FWHM	0.4 nm FWHM	
Spectral Sampling:	8 pixels/FWHM	6 pixels/FWHM	
Signal-to-Noise Ratio:	1000	4000	exposure time 0.8 s, surface albedo 0.18
Instantaneous Field-of-View:	1.34º (cross track) x 0.02º (along track)	5.85° (cross track, divided into 85 pixel) x 0.072° (along track)	
Ground-Projected Co-Added Pixel Size:	50-80 m (along track) over land (surface albedo 0.18) 4-5 km (along track) over water (surface albedo 0.01)	50-80 m (along track) over land (surface albedo 0.18) 4-5 km (along track) over water (surface albedo 0.01)	4 km flight height, ground speed 300 km/h (DLR Do 228 aircraft)

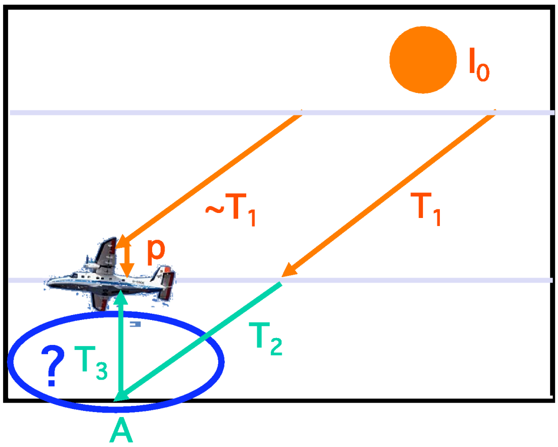

Figure 5: Zenith and nadir light paths and operation modes.

to the instrument. The problem is then how to separate the different contributions to the absorption, one by the molecules located under the aircraft and the other from all the rest of the atmosphere. This is done by measuring alternately with two different geometries: *nadir-looking* and *zenith-looking*.

In nadir mode, the instrument is pointed directly towards the surface. The majority of the photons coming directly from down below will have been emitted by the Sun (intensity I_0), gone through the atmosphere above the aircraft (with a transmissivity T_1), then through the atmosphere below the aircraft (transmissivity T_2), reflected at the surface (angular reflectivity A) in the direction of the instrument, again through the atmosphere (T_3) and then detected. The rest of the photons will have undergone multiple scattering and, as such, have a different light path, but in this case they are only a small fraction of the whole incoming radiation and can be neglected. The signal detected will be then $S_{down} = I_0 T_1 T_2 A T_3$. But only T_2 and T_3 are relevant for this research.

In zenith mode, instead, the instrument is looking directly above the aircraft. In this case, the largest contribution comes from those photons that are emitted from the Sun, are transmitted through the atmosphere (T_1) and scattered once (single-scattering) to meet the aperture angle of the instrument. Their light path then will result in $S_{up} = I_0 T_1 p$. We can assume that the transmissivity through the upper atmosphere T_1 is the same for nadir and zenith photons because solar rays run parallel, when the solar zenith angle is small. The factor p takes into account the scattering phase function and the absorption process by the optical fibers used to collect the light from the zenith direction (cfr. Figure 5).

By taking the ratio

$$\frac{S_{down}}{S_{up}} = \frac{I_0 T_1 T_2 A T_3}{I_0 T_1 p} = \frac{A}{p} T_2 T_3 \tag{25}$$

then the transmissivity below the aircraft $T_2 T_3$ is isolated. The factor A/p can be assumed as a variation with a low spectral frequency, and as such not relevant for the DOAS retrieval.

The zenith mode is currently not implemented in the WFM-DOAS v.HR-002 retrieval algorithm. All effects due to variations in I_0 and T_1 then are assumed to be compensated by the ratio between CO_2 and CH_4.

High-resolution and low-resolution The different components of the instrument have different operation times. Currently, in a measurement cycle of 2.00 seconds, the CH_4/CO_2 detector measures 10 spectra, the O_2A-band detector measures 2 spectra (because of the longer readout times of the CCD sensor), the Observer system records once the GPS and gyro information and a digital picture. The rest of the time is used to store the data on the on-board hard disks.

This structure has been chosen to have repeated, closely spaced measurements and have a better signal-to-noise ratio than would be possible with only one measurement. The 10 SWIR spectra, in fact, can be averaged together, and the resulting spectrum be used for the retrieval of the gas columns (*low-resolution retrieval*), or from each single spectrum a column value can be retrieved (*high-resolution retrieval*).

Both modes have advantages and disadvantages. In both cases, the data points (the spectra or the columns) have to be filtered for outliers and bad data, and then averaged, to reduce the background noise. Since the current method for the exclusion of unreliable data is based on the fit residuum, that is how different a measured spectrum is from the model, only the column factors can be filtered, and not the spectra before the fit. The high-resolution mode then allows to filter out single measurements, and the others can still be averaged together, instead of throwing away a full set of 10 spectra.

The exposure time can be changed to match the illumination (solar zenith angle) and the surface albedo: till now 58 ms has been chosen for the summer flights, over land, 78 ms for the autumn flights, over land, and 1.998 s for measurements over open water.

4.1.2 Pre-flight calibration

The instrument is calibrated before and during each flight by measuring the baseline signal offset (dark current measurement) and the efficiency of each detector pixel (white light source measurement).

Dark Current Measurement: During the flight dark current (DC) measurements are acquired for the SWIR spectrometer, with the detector shutter closed and the same exposure time as the open shutter measurements. For the NIR spectrometer, the same procedure is used, but for technical reasons the detector shutter is kept open. However, this doesn't affect the measurements because for the exposure times used the DC is essentially due to a constant electronic offset. For reference, an offset measurement is performed on ground, with a short exposure time, and used for the calibration.

During the flights on 23-07-2007, 26-07-2007 and 01-08-2007, due to failures in the setup no DC measurements in zenith-sky-mode were performed. The corresponding DC signal can be then determined either from the nadir-mode DC signal or from the WLS measurement: $DC_{zenith} = (DC_{nadir} - DC_{offset})^{\Delta t_{zenith}}/_{\Delta t_{nadir}} - DC_{offset}$.

White Light Source Measurement: Before or after each flight a white light source (WLS) measurement is performed, with the instrument in nadir-mode. A white-light quartz-tungsten-halogen (QTH) lamp is used to illuminate a transmissive volume diffuser. In zenith-sky-mode a small integrating sphere is used, since the instrument measures the incoming solar light through cosine-diffusers and glass fibers.

In each mode three measurements are performed:

- OPEN: lamp on, detector shutter open;
- CLOSED: lamp on, detector shutter closed;
- DC: background measurement, lamp off, detector shutter open;

so that the WLS signal used for the calibration is $I_{WLS} = I_{OPEN} - I_{DC}$ and the background light in the airport hangar is $I_{BG} = I_{DC} - I_{CLOSED}$.

4.2 The SCIATRAN radiative transfer model[1]

SCIATRAN is a radiative transfer program developed at the Institute of Remote Sensing (*ife*) / Institute of Environmental Physics (*iup*) at the University of Bremen.

It has been designed to allow fast and accurate simulation of radiance spectra as measured or expected to be measured from space with the passive remote sensing UV-Vis-NIR spectrometers GOME (Global Ozone Monitoring Experiment) and SCIAMACHY (SCanning Imaging Absorption spectroMeter for Atmospheric CHartographY). Due to the instrument similarities between MAMap and SCIAMACHY, SCIATRAN has been chosen to provide an accurate forward model for the MAMap retrieval. Moreover, SCIATRAN allows to simulate a wide range of different measurement scenarios, by the variation of its several internal parameters.

[1]This section is based on Buchwitz, 2003.

The wavelength range covered goes from 240 nm to 2400 nm, and several spectral windows can be selected. The sub-range fully supported is related to the GOME/SCIAMACHY spectral channels, i.e., 240-1750 nm (channels 1-6), 1940-2040 nm (channel 7), and 2260-2385 nm (channel 8).

Two different geometries can be adopted: plane-parallel and pseudo-spherical. The plane-parallel atmosphere approximation (neglecting all effects due to the sphericity of the Earth) is valid for solar zenith angles less than about 75 degrees. The pseudo-spherical mode instead has again a plane-parallel atmosphere but the (solar) source term is calculated in spherical geometry (including refraction). This gives accurate results for solar zenith angles less than about 92 deg in conjunction with a (satellite) "near-nadir" viewing geometry, i.e. about $\pm$ 35 degrees (top-of-atmosphere) line-of-sight zenith angle. Any altitude can be chosen for the viewing instrument, allowing the model to be used to simulate ground-based and airborne measurements, as well as satellite-based.

The absorption from the trace gases O_3, NO_2, ClO, OCLO, BrO, HCHO, SO_2, NO_3, O_4, O_2, and H_2O, CO, CH_4, and N_2O can be simulated, from spectroscopic line parameters like line position, line intensity, air-broadened half-width etc. (obtained from, e.g., the HITRAN spectroscopic data base). The broadening effects of temperature and pressure are taken into account.

Two program modes are implemented in order to accurately consider line-absorptions: (i) an accurate line-by-line and (ii) a significantly faster *correlated-k (c-k)* mode (cfr. Buchwitz, 2000).

Two aerosol parameterizations are implemented: The widely used LOWTRAN 7 aerosol scheme including Henyey-Greenstein phase functions or, alternatively, an aerosol parameterisation developed for GOMETRAN by R. Hoogen and J. Kauss.

The Earth surface is modeled as a Lambertian (isotropic) reflector with (wavelength dependent) albedo. The height of the surface w.r.t. the sea level can be specified.

Clouds can be treated in two different ways: either as scattering and absorbing layers of finite vertical extent ("Clouds As Layers" (CAL) scheme), i.e., similar to the aerosol parameterisation, and/or as reflecting lower boundary ("Cloud As Boundary" (CAB) scheme). The CAL scheme is accurate but rather slow, while the CAB scheme does not provide any information on the radiance field below the cloud top. The CAB scheme takes into account the angular dependence of the reflected light (i.e., the non-Lambertian reflectivity of clouds) and transmission losses through the cloud (using "escape functions"), but not absorption inside the cloud.

One of the most important features of SCIATRAN is that it calculates the full effect of multiple scattering (on both intensity and weighting functions). Rotational Raman scattering ("Ring effect") has also been implemented as well as thermal emission.

4.3 The MAMap WFM-DOAS v.HR-002 algorithm

The inversion method used to retrieve dry column mixing ratios of methane and carbon dioxide from the MAMap spectra is based on the Weighting Function Modified Differential Optical Absorption Spectroscopy (WFM-DOAS) algorithm developed for SCIAMACHY to retrieve analogous quantities. (Buchwitz et al., 2000)

The principle behind the DOAS inversion technique is the dependence of the absorbed solar radiance I_λ on the number densities $n_i(z)$ of the absorbing gases:

$$\ln\left(\frac{I_\lambda}{I_{0\lambda}}\right) = f(\sigma_{\lambda,i}(z), n_i(z)) \tag{26}$$

where $I_{0\lambda}$ is the Sun reference radiance and $\sigma_{\lambda,i}(z)$ the spectral absorption coefficient of the i-th gas. While in other spectral ranges this dependence can be accurately approximated with a linear model (Beer-Lambert's law) in the SWIR/NIR region this is not possible, for three reasons:

1. The spectral absorption coefficient $\sigma_{\lambda,i}$ has a strong dependence on temperature and pressure, which in turn vary with altitude z in a non-negligible way. It is not possible then to assume a constant value for $\sigma_{\lambda,i}$ along the slant column S, but an integral along the light path must be calculated. $\int \sigma_\lambda(z)n(z)dz \neq \bar{\sigma}_\lambda S$

2. Multiple scattering processes in the atmosphere introduce many different light paths, which then can't be described by a product of exponential functions like in the Beer-Lambert description with multiple absorbers: $I = I_0 \sum_k \exp(-\sigma_k S_k) \neq I_0 \exp(-\sum_k \sigma_k S_k)$

3. The presence of strong overlapping absorption lines due to the molecular roto-vibrational transitions of several absorbing gases on the same wavelength, and the inherent dependence of the resolving power of grating spectrometer systems on wavelength do not allow to distinguish exactly between each single absorption line, also due to different absorbers. This can be described by convolving the radiance spectrum with an instrumental slitfunction $\langle\cdot\rangle$, that does not commute with the exponential function (Frankenberg et al., 2005b). $\langle I_\lambda\rangle = \left\langle I_{0\lambda}e^{-\sigma_\lambda S}\right\rangle \neq I_{0\lambda}e^{-\langle\sigma_\lambda\rangle S}$

The multidimensional nonlinear function $f(\sigma_\lambda, n, p, T, z|i, k)$ can then be described using a simple Taylor linear expansion. The variables of the system are the atmospheric parameters like temperature T, pressure p and absorbing gas concentrations n_i (for CO_2, CH_4 and H_2O) that affect σ_λ and S, integrated then over the whole atmospheric column through k different light paths. Using an a-priori atmospheric profile $\bar{\mathbf{c}}$ as linearisation point, the a-priori absorption spectrum and the relative derivatives with respect to the atmospheric parameters $\mathbf{c}$ are computed through a radiative transfer model (SCIATRAN), and a low-order polynomial $P(\vec{a})$ is then added to account for all the other atmospheric factors (like cloud cover, aerosol concentration, surface albedo) and instrument calibration factors that have a weak spectral dependence:

$$\ln I_\lambda^{meas}(\vec{c}_{real}, \vec{a}_{real}) \approx \ln I_\lambda^{mod}(\vec{c}, \vec{a}) = \ln I_\lambda^{mod}(\vec{\bar{c}}) + \sum_j \left. \frac{\partial \ln I_\lambda^{mod}}{\partial c_j} \right|_{\bar{c}_j} (c_j - \bar{c}_j) + P_\lambda(\vec{a}) \tag{27}$$

The measured atmospheric scaling factors $c_{fit} = c/\bar{c}$ are then retrieved applying a least-squares fit to the observed experimental spectra:

$$\sum_\lambda \left(\ln I_\lambda^{meas}(\vec{c}_{real}, \vec{a}_{real}) - \ln I_\lambda^{mod}(\vec{c}_{fit}, \vec{a}_{fit}) \right)^2 \equiv \left\| R\vec{E}S \right\|^2 \to min. \tag{28}$$

To improve the matching between the modelled spectrum I_λ^{mod} and the observed one I_λ^{meas} a shift-and squeeze technique is then used; the wavelength range of the reference spectrum is adapted to each experimental spectrum by least-square fitting two parameters, wavelength displacement and interval width. An additional calibration is performed by subtracting a baseline dark signal spectrum periodically measured during each flight. To reduce the impact of the variable sensitivity of the detector pixels a ”white light” source signal is measured before each flight, and the nadir spectrum is divided by it.

The data product (level 2) generated in this work for each of the three spectral windows (CO_2, CH_4 and O_2 A-band) includes: three scaling factors (CO_2, CH_4 and H_2O columns for the SWIR channel; O_2 column, temperature and the first polynomial coefficient for the NIR channel), mean square residuum (RMS $= \left\| R\vec{E}S \right\|^2$), maximum radiance, flight time, GPS time and coordinates.

An initial version of the retrieval program had been developed by M. Buchwitz prior to this work. One of the weaknesses of this version (called vLR 004) is the highly simplified treatment of the radiative transfers in terms of the number of scenarios considered. In vLR 004 only one scenario is available: downlooking and uplooking from a constant aircraft altitude (700 m by default), constant solar zenith angle (default: 50°), constant temperature and pressure profiles (US Standard Atmosphere), constant aerosol depth, no cloud cover, constant surface albedo (default: 0.1).

Version LR 004 is considered a good starting point for this thesis, as it permits to analyse the measured spectra in detail and to get qualitative results (relative variations of the GHG scaling factors), but needs significant improvements in order to get highly accurate quantitative GHG results.

Part III

Results of pre-flight theoretical estimates

5 Methane variability and MAMap capabilities

The first step in the assessment of the real capabilities offered by MAMap is a comparison between its theoretical sensitivity (3% column enhancement for a 3 km column, see Section 4.1) and the observed range of natural variability. In particular, we need to be able to relate MAMap measurements with ground-based data, to validate the instrument measurement and to have the needed spatial resolution for a comparison. MAMap can, by the ratio of the nadir and the zenith observations, measure the relative variation in the vertical CH_4 column, that is the total number of molecules present on the whole light path between the ground and the instrument (for example, 3 km). Ground-based instruments instead measure CH_4 mixing ratios only at a single altitude level, near the ground. These two different quantities of different kind can't be then directly converted one into the other without making assumptions about the vertical profile of methane mixing ratio, and how this changes as a function of the ground mixing ratio. These assumptions must be based on the typical structure of the lowermost layer of the atmosphere, the planetary boundary layer. Section 5.2 will then present the results of upscaling ground mixing ratios to vertical column enhancements. These are then compared with observed ground mixing ratios from different European sites.

5.1 Boundary layer structure and atmospheric profiles

Every fluid moving in contact with an external surface builds up a thin layer where the interaction with this surface takes place. The kinetic energy of the fluid particles in laminar motion is gradually dispersed through turbulence to the point of contact with the surface, where the fluid speed is zero. Turbulence then causes a stronger mixing of momentum, heat and dissolved components than in the sections of the same fluid in laminar motion. The atmosphere of a planet is no exception: the thin portion of the Earth's atmosphere in direct contact with the surface, where friction effects dominate the air motion, is called the planetary boundary layer. In this layer most of the conductive and convective heat exchanges between the atmosphere and the land or the ocean occur, and most of the short-range variability we call weather.

The boundary layer itself can be divided in three vertical sublayers, where different effects dominate: the viscous sublayer, the surface sublayer and the Ekman sublayer. The viscous sublayer is the closest to the surface, few millimeters deep, and dominated by molecular friction. In the surface sublayer turbulent mixing prevail, while the Ekman sublayer marks the slow transition to the laminar flow of the free troposphere. The wind profile is then different in the three layers: no speed at the ground surface, then increasing gradually to the geostrophic speed and direction at the upper boundary of the Ekman layer.

The vertical extent (or depth) of the boundary layer depends then on two factors, through two different mechanisms: the wind speed in the free troposphere (and particularly its shear, or vertical gradient) determines the strength of the turbulent dissipation; the temperature profile controls the strength of convective vertical motions. It is observed, for example, that for the same wind speed, the boundary layer could be 50 m deep in the Arctic night, due to the strong stratification (the ground being colder than the air) or 2 km deep at the tropics, due to the strong cumulus convection. At mid-latitudes the temperature profile is mostly dependent on the daily cycle, with most convective motions (and subsequent mixing) occurring during the day.

The interest of this work lies in how the boundary layer structure affects the vertical diffusion of pollutants produced at the surface, like methane. They can accumulate under a temperature inversion cap, when strong stratification prevents vertical diffusion, or otherwise be diluted by convection. Methane vertical profile measurements, like those from Miller et al. (2007), show that enhanced values at the surface gradually decrease with height, to reach background values at an altitude between 1 and 2 km (see Figure 6, upper left panel).

Marques Filho et al. (2006) estimated with a Large Eddy Simulation model how a vertical profile (in this case constant up to 1 km, then zero) gets modified by vertical turbulent and convective diffusion. The upward drift of surface air is compensated by entrainment of air from the upper layer, and mixing occurs, again to an altitude between 1 and 2 km.

These results from the literature let us assume that the methane emitted from a source located at the surface gets diffused along the boundary layer only to a given height, above which the atmosphere is well-mixed and has then values close to the global background average.

5.2 Methane column estimate from ground concentrations

The upscaling calculation consists in summing the number of methane molecules in each altitude layer between 0 and 3 km height, so to obtain the vertical methane column VC_{CH_4}. The pressure profile $p(z)$ and temperature profile $T(z)$ are based

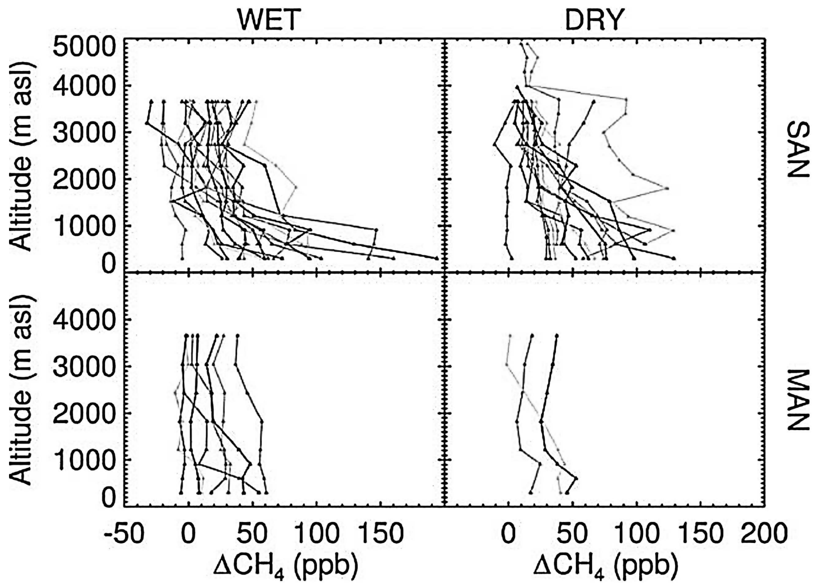

Figure 6: Methane vertical profiles from two different measurement sites in Brazil: Santarém (top) and Manaus (bottom) during the (left) wet and (right) dry seasons, differenced from a marine boundary layer reference. Different shades of gray represent profiles collected on different days and are included as a visual aid to separate profiles. From Miller et al. (2007).

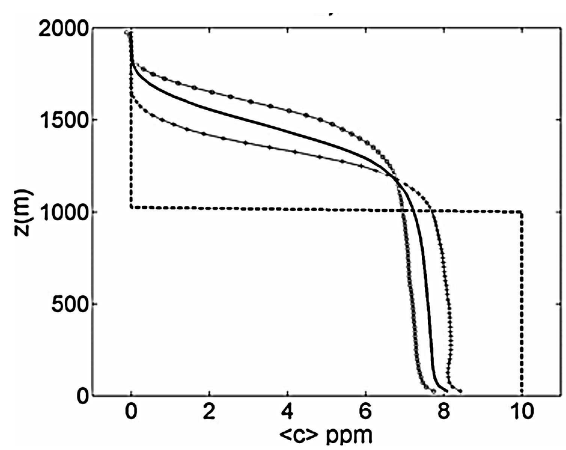

Figure 7: Pollutant concentration vertical profiles from a Large Eddy Simulation Model. The initial conditions are indicated by the dashed stepfunction line, the ensemble average by the thick line. From Marques Filho et al. (2006).

on the US Standard Atmosphere (McClatchey et al., 1972). For the background reference column, the methane mixing ratio $X_{CH_4}^{BG}$ is constant for any altitude z (due to turbulent mixing) and equal to 1750 ppb.

$$VC_{CH_4} = \int_{z_0}^{z_1} \frac{p}{k_B T} X_{CH_4} dz \tag{29}$$

In presence of a ground concentration above the average instead, the profile is modified so to model the turbulent mixing along the boundary layer. For simplicity, no detailed shape of the profile $X_{CH_4}(z)$ is assumed, but four simple scenarios, so to have a range of variability corresponding to different atmospheric conditions: in two of them the methane mixing ratio is constant and equal to the ground value up to a height z^*, then equal to the background value (stepwise profile), in the other two a linear mixing is assumed, with the mixing ratio decreasing linearly from the ground value to the background value at the height z^* (linear profile). Two different z^* are assumed, either 1 or 2 km (see Figure 8-above).

The results are given in percentage relative increase ($^{VC}/_{VC_{BG}}$) in Figure 8-below, and show that a 3% increase of the 3-km column can correspond to different ground mixing ratios, depending on the profile assumed, that is the strength of the vertical mixing, in a range between 1825 ppb (in case of a 2 km-deep stepwise profile) and 1980 ppb (for a 1 km-deep linear profile).

It can be concluded then that in worst-case-scenario, that is with low gas accumulation (linear mixing) and a shallow boundary layer (1 km deep) the instrument can observe, under the current requirements, methane enhancements corresponding to an increase from the background of the surface mixing ratio of 250 ppb and above. If the state is more favorable, that is due to an inversion cap stronger accumulation occurs (stepwise mixing) and the boundary layer height is larger, then also lower surface enhancements can be observed. It is therefore crucial for each quantitative study based on MAMap data to have a clear understanding of the meteorological conditions, so to have an estimate of the methane profile as accurate as possible.

It is also important to notice that this calculations are based on the instrument requirements, not on the actual sensitivity that can be assessed from the flight data, and as such the instrument actual detection capability could be different.

5.3 Comparison with ground data

It is useful to compare the estimated lowest detectable methane mixing ratio at ground level (250 ppb above the background, as a conservative estimate, or 75 ppb, as an optimistic estimate) with the natural variability observed by ground-based measurements.

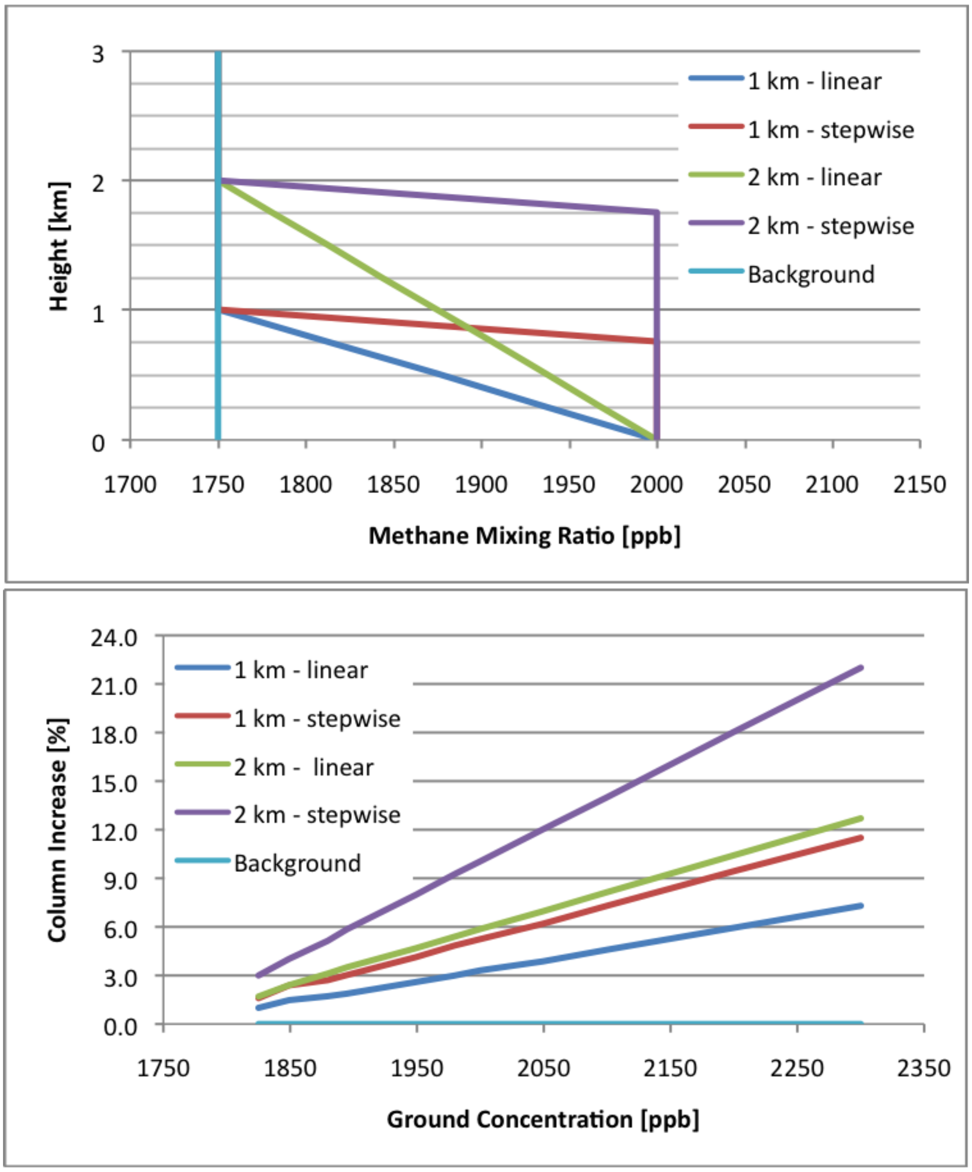

Figure 8: Atmospheric methane column estimate.
Above: assumed mixing ratio vertical profiles for the four different scenarios.
Below: relative enhancements of the 3 km methane column from upscaling of different ground concentrations.

Bergamaschi et al. (2005) reports the results of several ground stations belonging to different observation networks, such as Kollumerwaard (the Netherlands, World Data Centre for Greenhouse Gases - WDCGG), Zingst (Germany, Federal Environmental Service and WDCGG), Mace Head (Ireland, Advanced Global Atmospheric Gases Experiment - AGAGE). The graphs in figure 9 show in black the measurements from each station, daily averaged, with the error bars highlighting the daily variability, for September and October 2001. The Zingst and Kollumerwaard stations are both located in methane-producing regions, and most of the measured variability is due to advection from regional sources. Both show several values more than 250 ppb over the background, and most of the values are higher than the 75 ppb optimistic detection estimate. The Mace Head station instead show smaller deviations from the background (1780 ppb). This is to be expected, since the station is located close to the ocean, and as such far from direct methane sources.

Belikov et al. (2006) measured methane mixing ratios along the Trans-Siberian railroad during the Transcontinental Observations into the Chemistry of the Atmosphere (TROICA) project, between 1995 and 2004. Figure 10 shows the results of the experiment of March 2004 (winter) and July 2001 (summer). During the summer campaign several events have been observed when the methane levels were more than 250 ppb above the background, in correlation with the position of the major Siberian wetland regions and industrial zones. The average level was instead between 1750 and 1850 ppb. On the other side, during the winter campaign the number of events able to cross the detection threshold was much lower.

We can conclude that the required sensitivity for the instrument is suited to observe major methane enhancement events under the appropriate conditions. This means that the season and the meteorological conditions are crucial factors for the production of a methane enhancement signal strong enough to be detected.

6 Instrument signal-to-noise and retrieval precision estimates

The aim of this section is to estimate the magnitude of the uncertainties on the retrieved columns. This will be useful to check the coherence of the flight results with the planned specifications, and as a guideline for future experiments. The method chosen is to simulate the instrument signal and noise, based on technical specifications and the expected range of geophysical parameters, and then apply the inversion fit to obtain the relative uncertainties, as a function of ground surface reflectance and exposure time. These two parameters have actually the largest influence on the signal strength, so directly on the relative noise.

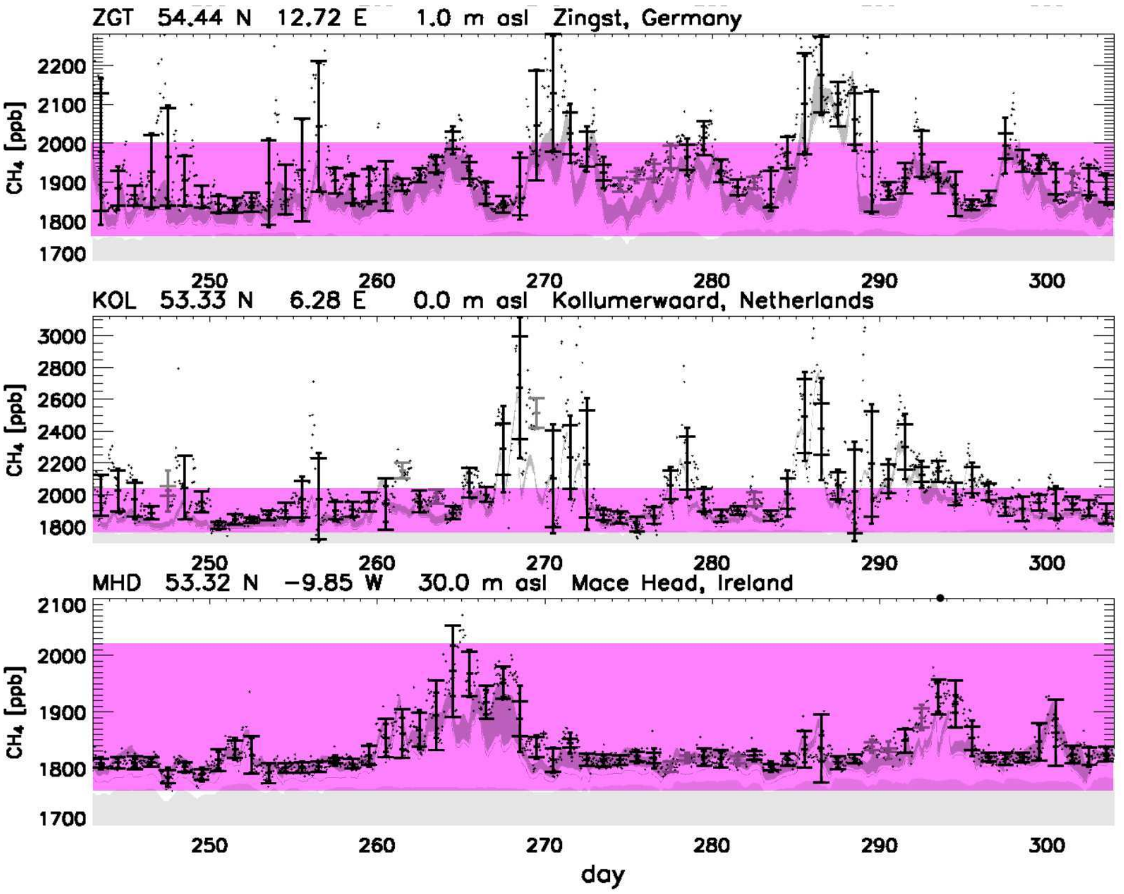

Figure 9: Observed methane concentrations at European sites for September and October 2001. Modified from Bergamaschi et al. (2005). The black dots with the error bars are daily average ground measurements. The purple range show the 250 ppb deviation from the background needed to cross the calculated sensitivity threshold for MAMap.

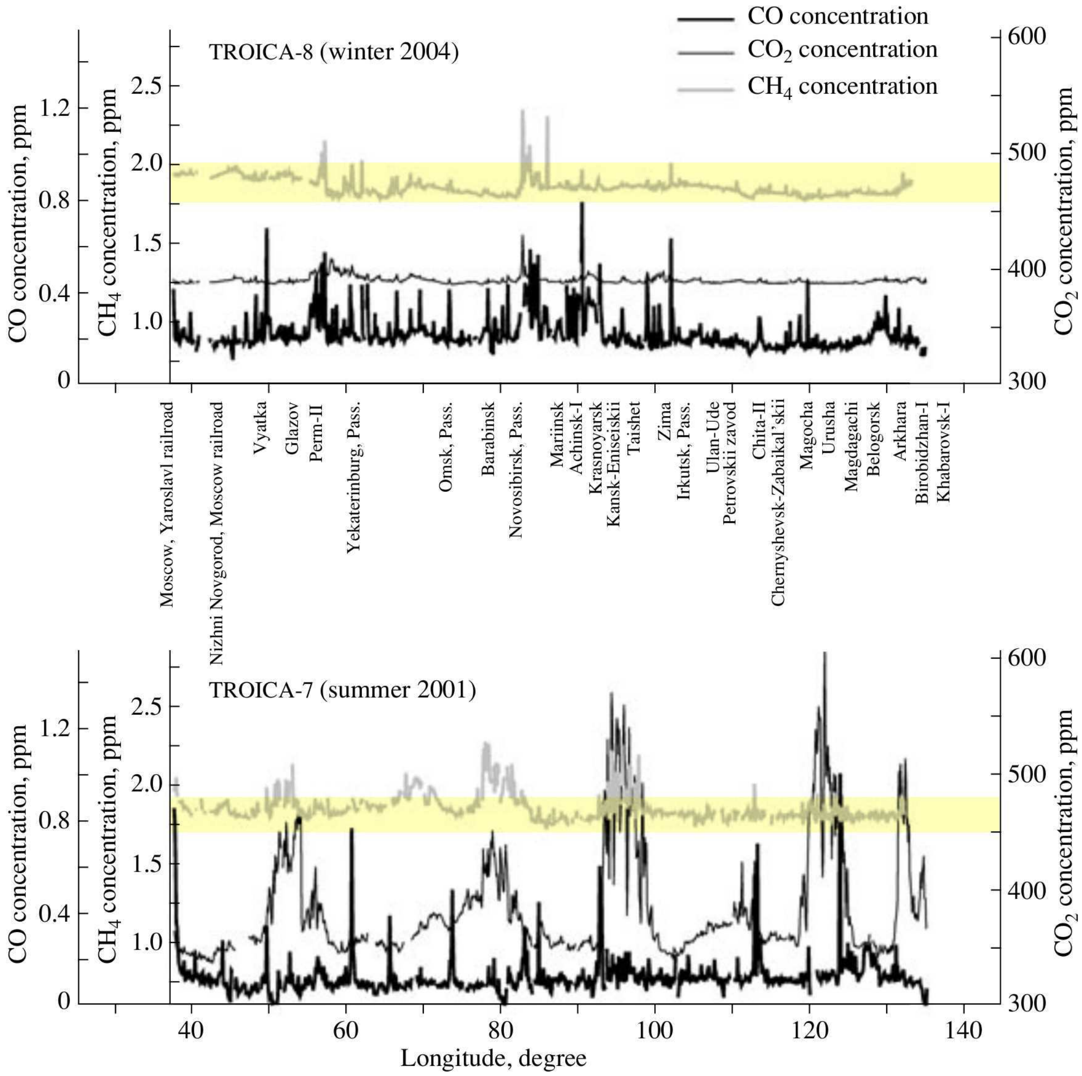

Figure 10: Carbon monoxide, carbon dioxide and methane concentrations measured in the back routes of the cold-season (TROICA-8) and warm-season (TROICA-7) expeditions. Modified from Belikov et al. (2006). The methane levels are plotted in grey, the yellow range show the 250 ppb deviation from the background needed to cross the calculated sensitivity threshold for MAMap.

6.1 Noise and random uncertainty

As shown in Section 3.3, the uncertainty on a fitted variable x_i (the relative gas column) depends on the uncertainties on the measured variables y_j (the radiance for each spectral pixel). Leaving aside systematic biases, the random uncertainty is a measure of the scatter of the individual measured data points from the "real" value, assumed as the mean of their distribution. This scatter is due to several sources of disturbance, that together form the so called *measurement noise*. An estimator of the relative relevance of the noise is the *signal-to-noise ratio* (SNR), defined as:

$$SNR = \frac{S}{N} = \frac{S}{\sqrt{\sum_i N_i^2}} \tag{30}$$

where S denotes the signal amplitude, and the N_i the different sources of noise specific to the experiment. The strength of the noise compared to the level of the signal will then give an estimate of the relative uncertainty:

$$\frac{1}{SNR} = \frac{N}{S} = \frac{\sigma_{y_i}}{y_i} \tag{31}$$

For an airborne remote sensing spectrometer (such as MAMap), S is the number of electrons gathered from the detector pixels in the wavelength range considered. S is given then by:

$$S = t_{exp}\, G\, T\, QE\, \Delta\lambda\, R \tag{32}$$

where

- $R[{}^{photons}/_{s\,nm\,cm^2\,sr}]$ is the incoming radiance as a function of wavelength λ, computed with a radiative transfer model, based on atmospheric gas profiles and spectroscopic data. Its value is highly dependent on several parameters, like the solar zenith angle ϕ_0 and the surface reflectance ρ assumed.
- $t_{exp}[s]$ is the exposure time for a single detected spectrum.
- $G[sr\,cm^2]$ is the étendue, i.e. the product of the aperture area and the solid angle of the instantaneous field of view of the spectrometer.
- $T[-]$ is the transmittance of the instrument optics.
- $QE[{}^{electrons}/_{photon}]$ is the quantum efficiency of the detector.
- $\Delta\lambda\,[{}^{nm}/_{px}]$, the pixel resolution, is the wavelength range covered by each detector pixel.

The different noise components N_i, on the other side, are due to spurious currents originating in the detection circuits. The first source, called *shot noise*, is due to the quantum behaviour of the detector photodiodes. Each time a photon hits a pixel surface, there is a given probability (the quantum efficiency) that it will be absorbed by the material and an electron will be freed. This can then cross the p-n junction of the diode, and be collected as a small current by the readout electronics. The absorption of photons by atoms is a random process, so that even when the photodiode is exposed to a constant photon flux, the number of electrons emitted will fluctuate randomly. In the given experimental conditions, the number of electrons generated is small enough for this random uncertainty to be significant. Given the nature of the process, it can be described by a Poisson statistics, where the variance is equal to the square root of the mean. This means that the shot noise N_S can be estimated as the square root of the signal S:

$$N_S^2 = S\left(t_{exp}\right) \tag{33}$$

The same principle must be applied to the dark current, that is the signal measured in absence of external exposure. Two different factors contribute to it: the infrared radiation S_T^* emitted by the system itself due to its temperature T, that in the wavelength range considered can't be neglected, and the current leakage through the p-n junction I_d due to the reverse bias tension. Both increase with the exposure time, contributing to the overall *dark current shot noise* N_{DC} :

$$N_{DC}^2 = t_{exp}\left(S_T^* + \frac{I_d}{q}\right) = \frac{t_{exp}}{q} I_{DC} \tag{34}$$

where q is the electron charge.

The third noise component is the *electronic readout noise* N_{RO}, the sum of all the noise contributions arising from the readout process and are independent from the exposure time, resulting in an offset of the measured signal:

$$N_{RO}^2 = const. \tag{35}$$

6.2 Instrument and retrieval simulation

For the the above calculations, the following values are assumed constant:

- Solar zenith angle (SZA) : 65º
- CH_4 column : $3.67150 \cdot 10^{19}$ ${}^{molecules}/_{cm^2}$
- CO_2 column : $8.18864 \cdot 10^{21}$ ${}^{molecules}/_{cm^2}$
- H_2O column : $4.77117 \cdot 10^{22}$ ${}^{molecules}/_{cm^2}$
- Surface temperature : 288.1 K

- Surface pressure : 1013 hPa
- Aircraft altitude: 700 m
- Wavelength range:
  1630.0 - 1675.0 nm (CH_4 fit)
  1593.0 - 1617.0 nm (CO_2 fit)
- $G : 6.38 \cdot 10^{-5}\, cm^2\, sr$
- $T : 0.4$
- $QE : 0.649997\, {}^{electrons}/_{photon}$
- $P_R : 0.0974121\, {}^{nm}/_{px}$
- $t_{exp} : 0.058\, s$
- $I_{DC} : 50\, fA$
- $N_{RO} : 1390\, electrons\, (r.m.s.)$

For given values of the surface reflectance (or albedo) ρ, a transmissive radiative transfer model was used to compute the mean radiances $\bar{R}$ in the two wavelength intervals (for CH_4 and CO_2 respectively). Since the signal is recorded by the instrument as counts on a digital 16-bit scale (0-65535), a factor K_e : 67.42 ${}^{electrons}/_{count}$ is used to relate each surface reflectance to the corresponding mean signal $\bar{S}$. The SNR is calculated as above, with a value of N_{DC} : 134.5 electrons. The relative error on the inverted columns x is then computed by the WFM-DOAS linear fit. All these results are shown in table 6.2.

Figure 12 shows the surface reflectivities in the SWIR infrared band (1500-1700 nm) of different terrain coverage types. Vegetation-covered areas have reflectivities in the range between 0.1 and 0.2. Bare soil and sand can reach reflectivities around 0.4. Open water, instead, has a reflectivity under 0.05.

The average ground scene is then expected to have a reflectivity around 0.15 (see figure 11), corresponding to retrieval errors of 0.76% for CH_4 and 1.1% for CO_2. For the ratio CH_4/CO_2 this gives $\sqrt{1.1^2 + 0.76^2} = 1.4\%$. The value of the retrieval errors are approximately inversely proportional to the reflectivities. So for a reflectivity of 0.05, the order of magnitude of the errors is a few percentages.

The same errors correspond to a RMS of the spectral fit ${}^{\sigma_y}/_y$ of 0.3%. It is important to notice that the instrument specifications require the results of 10 spectra to be averaged together (to an effective exposure time of 0.6 s). This would result in retrieval errors a factor of $\sqrt{10}$ smaller, namely 0.24% for CH_4, 0.35% for CO_2 and 0.42% for the ratio CH_4/CO_2.

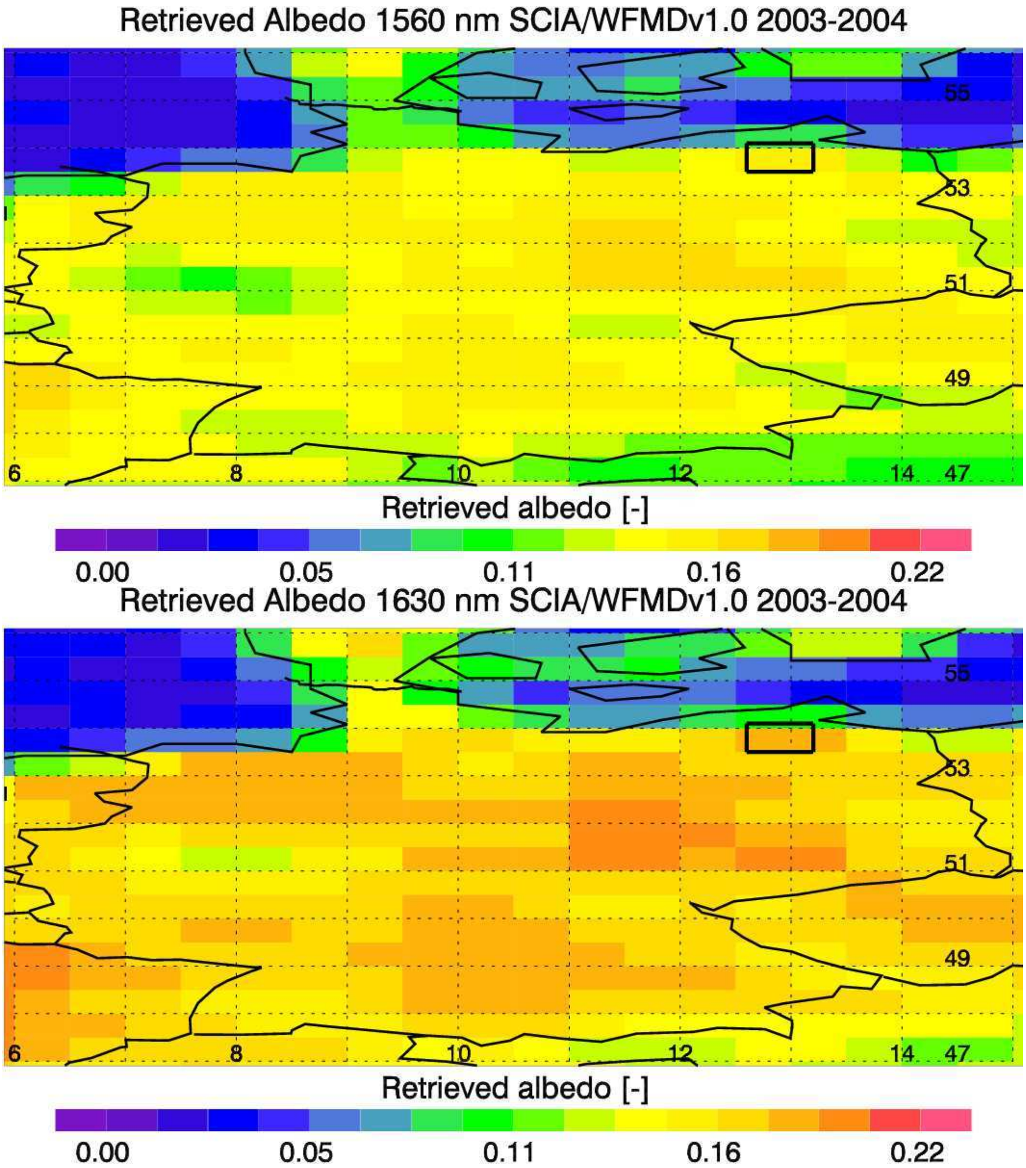

Figure 11: Ground reflectivity retrieved from SCIAMACHY. Above: 1560 nm (CO_2 wavelength range). From Buchwitz et al., 2007, Schneising et al., 2008a. Below: 1630 nm (CH_4 wavelength range). From Schneising et al., 2008b.

	ρ Surface Reflectance [-]	$\bar{R}$ Mean Radiance [photons/ s nm cm^2 ster]	$\bar{S}$ Mean Signal [counts]	$\bar{S/N}$ Mean SNR [-]	σ_x/x Relative Column Error [%]
$x = CH_4$	0.01	3.75E+11	821.08	24.93	10.24
	0.02	7.50E+11	1342.15	49.43	5.16
	0.05	1.87E+12	2905.31	120.47	2.11
	0.10	3.75E+12	5510.77	231.57	1.10
	0.15	5.62E+12	8116.08	334.81	0.76
	0.20	7.50E+12	10721.53	431.39	0.58
	0.40	1.50E+13	21143.07	767.14	0.33
$x = CO_2$	0.01	3.84E+11	833.63	25.53	14.75
	0.02	7.68E+11	1367.27	50.60	7.44
	0.05	1.92E+12	2968.15	123.25	3.05
	0.10	3.84E+12	5636.29	236.71	1.59
	0.15	5.76E+12	8304.58	342.01	1.10
	0.20	7.68E+12	10972.72	440.38	0.85
	0.40	1.54E+13	21644.89	781.68	0.48

Table 2: Signal-to-noise estimates based on instrument simulation.

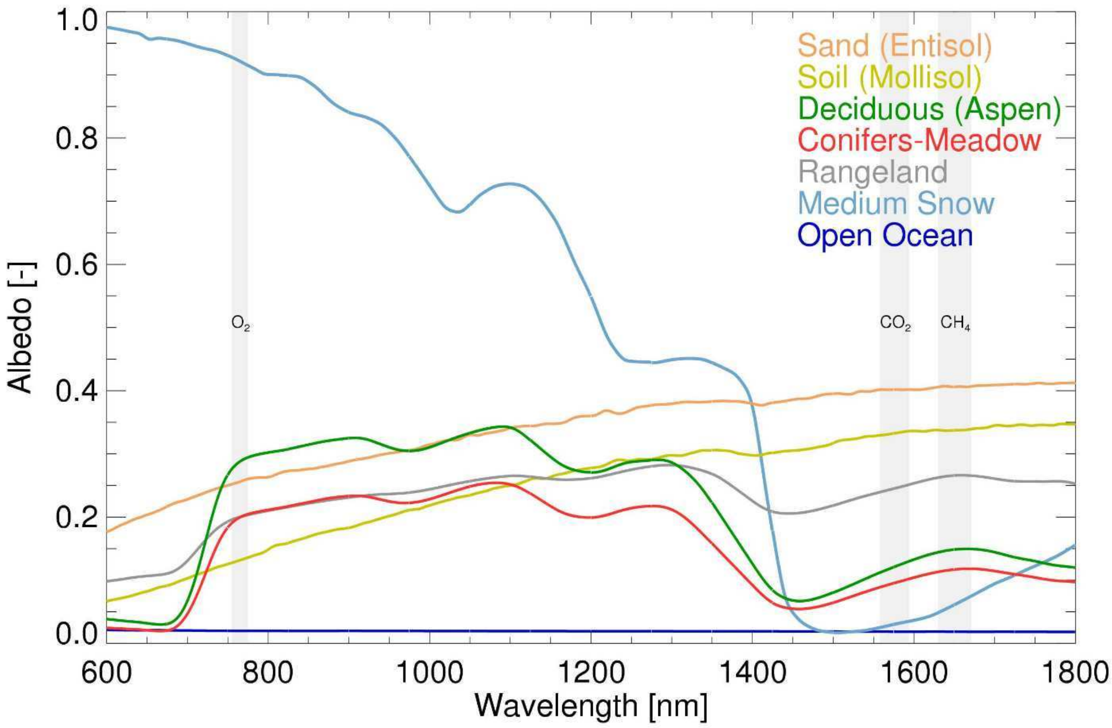

Figure 12: Spectral surface reflectivities for different terrain types. The wavelength ranges used for the retrieval of greenhouse gases from SCIAMACHY are highlighted. From Schneising et al., (2008b).

Part IV

Results of a first analysis of in-flight data

After initial technical test flights in autumn 2006, the MAMap instrument has completed two measurement campaigns in 2007 and one in 2008: overall 5 flights in summer (23-07-2007, 26-07-2007, 01-08-2007, 02-08-2007 and 24-06-2008) and 2 flights in autumn (28-10-2007, 31-10-2007). The flights were performed with Cessna Caravan aircraft, in cooperation with the Technische Universität Berlin and the GeoForschungZentrum Potsdam. Each of the flight targets has been chosen because of special CO_2 or CH_4 emissions as described in detail below (Sections 9 to 11 and Appendix A).

Target Area	23-07 2007	26-07 2007	01-08 2007	02-08 2007	28-10 2007	31-10 2007	24-06 2008
Coal Power Plants (Jänschwalde, Schwarze Pumpe)	-	x	-	-	-	x	-
CO_2 Storage Station (Ketzin)	x	x	x	x	-	-	-
Methane Bottle (Ketzin)	-	x	x	x	-	x	x
Wetlands (Zarnekow)	-	-	-	-	x	-	x
Open Coal Mines (Cottbus)	-	x	-	-	-	x	-
Wetlands (Paulin Aue)	-	-	x	x	-	-	-

Table 3: Targets surveyed in each flight.

The first two sections of this chapter describe analyses done on the calibration data, or on entire flight tracks. The information on the overall characteristics of the datasets is then used in the analysis on the data gathered on three special targets, discussed in Sections 9, 10 and 11. The description of these targets follows the same structure. The fit residuum distributions for the CO_2 and CH_4 fits are first presented, with a discussion of the filtering criterion based on the analysis of the distributions described in Section 8.1. The filtered inverted column values are then shown and discussed, in two different forms, as time series and as maps. To check the repeatability of the measurement, that is if the instrument can detect the same signal on different overpasses, segments of flight track, either parallel or over the same trajectory, are selected, and the column values displayed as a function of a flight spatial coordinate. To assess instead the ability of the instrument to observe a two-dimensional spatial pattern, the column values are drawn as latitude-longitude maps.

7 Inter-flight stability from calibration spectra

The data gathered during the 2007 flight campaigns is used to determine if MAMap complies with the declared specifications (see Table 1), and if significant changes in the calibration occur between different flights. This analysis is needed in order to exclude biases in the retrieved parameters due to instrument malfunction. Two parameters are chosen to verify the functioning of the SWIR detector: the DC and WLS signals collected during each in-situ calibration (see 4.1.2). The acquired spectra are analysed directly, excluding 60 ”bad” pixels that show abnormal behaviour (like high dark current) and are left out of the column retrievals.

7.1 SWIR Detector Stability

The analysis of the calibration spectra (dark current and white light source) provides information on the detector performance. The SWIR spectra are provided in counts between 0 and 65535, and the filling factor for each pixel is defined as the pixel value divided by the maximum value, thus spanning between 0.0 (no signal) and 1.0 (saturation). Since the summer and the autumn flights had different exposure times due to the different illumination conditions (respectively 58 and 78 ms), it is useful also to investigate the DC spectra in terms of counts per second. In Figure 13 the DC spectra are shown as counts, counts per second and ratio with a reference spectrum (26-07-2007).

The dark signal is nearly constant for all the pixels, with filling factors between 0.009 and 0.014, that is between 600 and 800 counts. This value is on the same order of the signal expected when flying over low-albedo (0.01) scenes, like water, with an exposure time of 0.058 s. This justifies the choice of a longer exposure time when flying over water.

The expected dark signal I_{DC}, as described in Section 6, is a sum of two factors:

$$I_{DC} = I_{const} + \left(\frac{\Delta I}{\Delta t}\right) t_{exp} \tag{36}$$

one (I_{const}) due to electronic offset, is equal for each measurement, the other instead

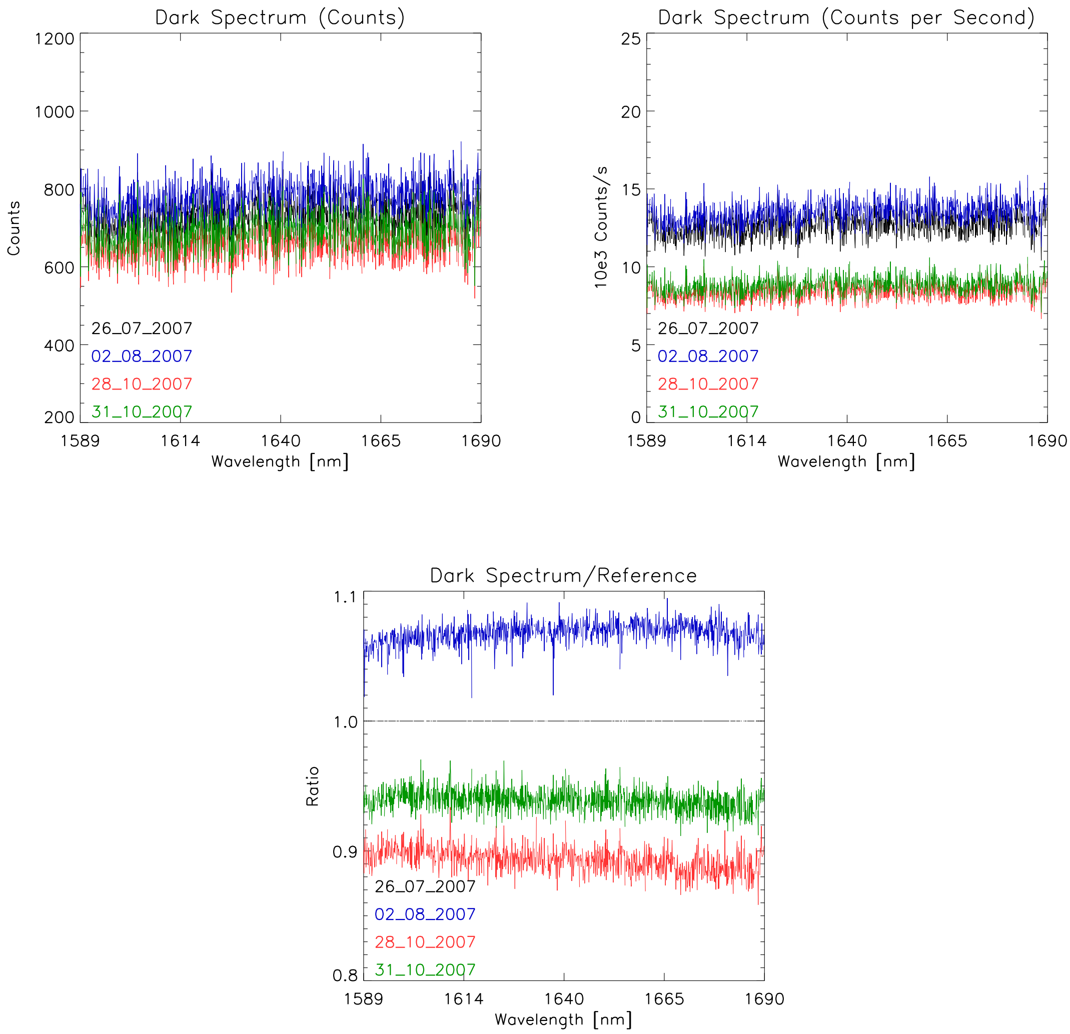

Figure 13: Dark current signals for the four flights:
(26-07-2007, 02-08-2007, t_{exp} = 0.058 s; 28-10-2007, 31-10-2007, t_{exp} = 0.078 s). Upper Left: Number of counts (on the scale 0-65535). Upper Right: Counts per second (counts divided by the exposure time). Lower: Ratio with a reference DC spectrum (26-07-2007). The difference between the different seasons is due to the manual setting of the temperature stabilization of the optical bench (see text).

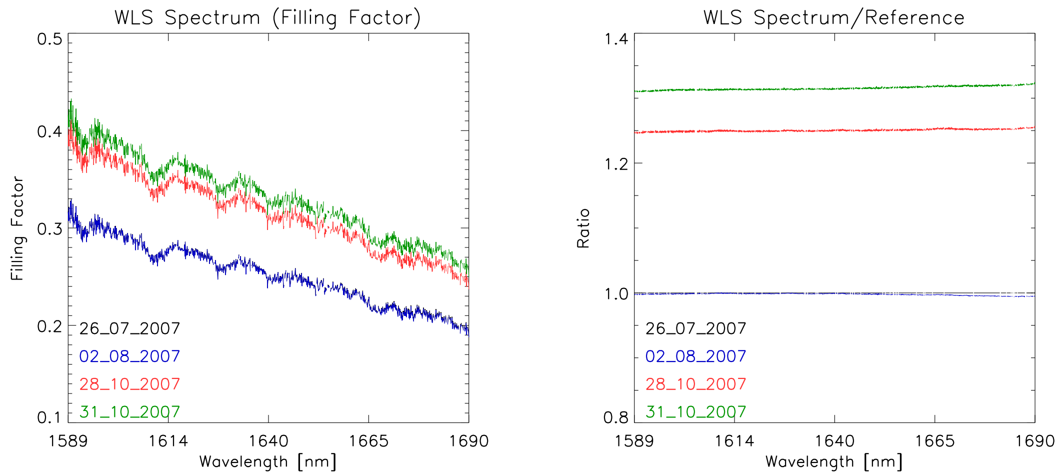

Figure 14: White light source signals for the four flights.
Left: Filling factor (0 - no signal, 1 - detector pixel saturation)
Right: Ratio with a reference DC spectrum (26-07-2007).
The measurement is not performed against a calibrated source. As such it can't be interpreted in terms of its absolute value, but only for its relative spectral dependence.

depends on the exposure time. The relative weight of the constant and the time-dependent factors can be assessed by dividing the dark signal by the exposure time (counts per second). The following table shows the possible cases:

$I_{const} \ll (\Delta I/\Delta t)$	$I_{const} \gg (\Delta I/\Delta t)$
$I_{DC} \propto t_{exp}$	$I_{DC} \propto I_{const}$
$I_{DC}/t_{exp} = const$	$I_{DC} = const$

If the time-dependent part is much larger than the constant part, then the signal levels from different flights will be significantly different, but the ratio signal/exposure time will be constant. If instead the constant part is larger, the signal levels will be similar from flight to flight.

It can be seen, then, that while the average dark filling factor is remarkably stable from flight to flight, the dark signal in counts per second has different values for the summer and the autumn flights. Both the summer flights show values around 13000 counts/s, the autumn flights around 8500 counts/s. The two flights of the same season instead show little or no difference. The time-dependent contribution to the dark current is then smaller than the constant one. The third plot shows the ratios between each dark signal spectrum and the first one (26-07-2007) taken as reference. The two summer flights have larger values (1.0 - 1.05) than the autumn flights (0.9 - 0.95). This signal was not divided by the exposure time, so the reason for the discrepancy is most likely the different temperature chosen during the measurements

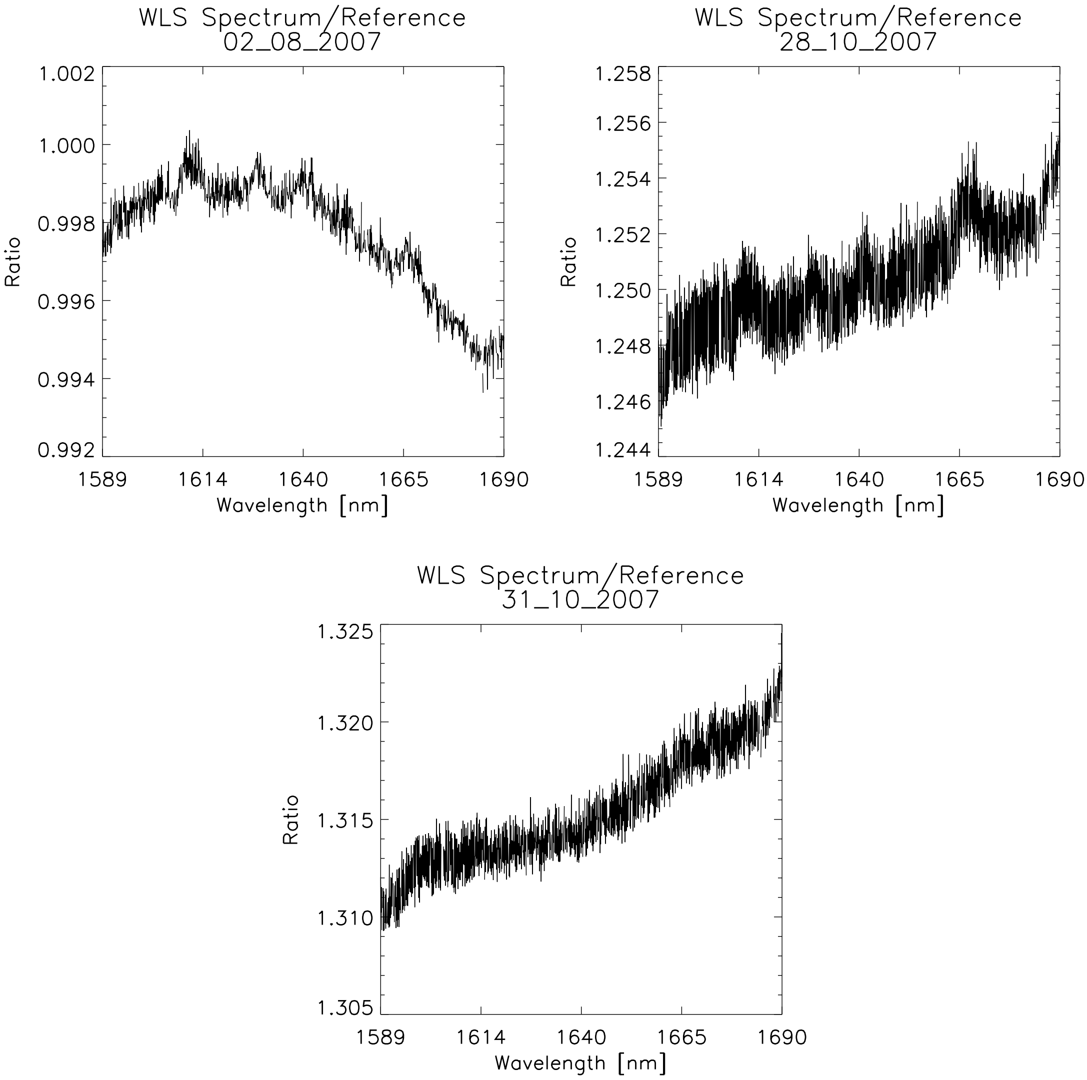

Figure 15: White light source signals divided by the reference (26-07-2007).

to keep the optical bench thermally stable (35ºC in summer, 29ºC in autumn), which then directly affects the thermal emission part of the dark signal (Eq. 34).

The white light source spectra (Fig. 14) also show remarkable stability between different flights. The offsets between the different spectra are explained by the setup of the QTH lamp, that was different for each measurement. The white light calibration is not an absolute calibration, but only a measurement against a flat spectrum to eliminate the effect of the different sensitivity of the detector pixels. As such, the measurement setup and position, and the brightness and temperature of the lamp are not stable between different measurements.

Some spectral features can be observed, and can be explained by etalon-like effects in the spectrometer system, but these are also stable for all the flights. The variations relative to the reference spectrum, as shown in Fig. 15 are on the order of 0.2 %, adding thus a minor contribution to the noise level.

8 Fit residua: inter-flight stability and impact of illumination

This section describes the analysis performed on the fit residuum distributions of the 2007 flight datasets. The goals are to check the stability of the retrieval algorithm on different datasets, and to establish proper thresholds for the filtering of unreliable data. Moreover, an interesting pattern emerged comparing the data gathered in different seasons, with different meteorological conditions, that led to detailed multidimensional analysis for one of the flight days, 28-10-2007.

8.1 Inter-flight stability and filtering

Previous analyses of the retrieved columns demonstrated the need for a filtering criterion, in order to exclude outliers from the dataset and highlight the detected spatial signals. This procedure is also based on the experience gathered with the retrieval of greenhouse gases from SCIAMACHY (Schneising et al., 2008). The parameters chosen for the filtering were the fit root mean square (RMS) residua $\|RES\|^2$ for the CH_4 and CO_2 column fits and the maximum signal I_{max}. The RMS residuum (eq. 37) is the relative difference between the measured spectrum and the one modeled (the sum of the weighting functions multiplied by the fit parameters), summed on the N spectral pixels.[2] As such it is an indicator of the reliability of the column value retrieved from that spectrum, and it is proportional to the inverted column errors themselves. The maximum signal (eq. 38) is an indicator of the saturation level of the detector, and the overall strength of the signal.

$$RMS = \sum_{i=1}^{N} \sqrt{\left(\frac{I_i^{meas} - I_i^{mod}}{I_i^{mod}}\right)^2} \tag{37}$$

[2]It is important to note that the residuum used in the MAMap data elaboration is a dimensionless, relative quantity. This is a direct consequence of performing the fit on the logarithm of the spectrum, rather than on the spectrum itself, as seen in Section 4.3.

$$\ln I_i^{meas} - \ln I_i^{mod} = \frac{I_i^{meas} - I_i^{mod}}{I_i^{mod}}$$

when $I_i^{meas} - I_i^{mod}$ is small. Proof:

$$I_i^{meas} - I_i^{mod} = \Delta \Rightarrow I_i^{meas} = I_i^{mod} + \Delta$$

$$\ln I_i^{meas} - \ln I_i^{mod} = \ln\left(I_i^{mod} + \Delta\right) - \ln I_i^{mod} = \ln\left(\frac{I_i^{mod} + \Delta}{I_i^{mod}}\right) = \ln\left(1 + \frac{\Delta}{I_i^{mod}}\right)$$

$$\lim_{\Delta \to 0} \ln\left(1 + \frac{\Delta}{I_i^{mod}}\right) = \frac{\Delta}{I_i^{mod}} = \frac{I_i^{meas} - I_i^{mod}}{I_i^{mod}}$$

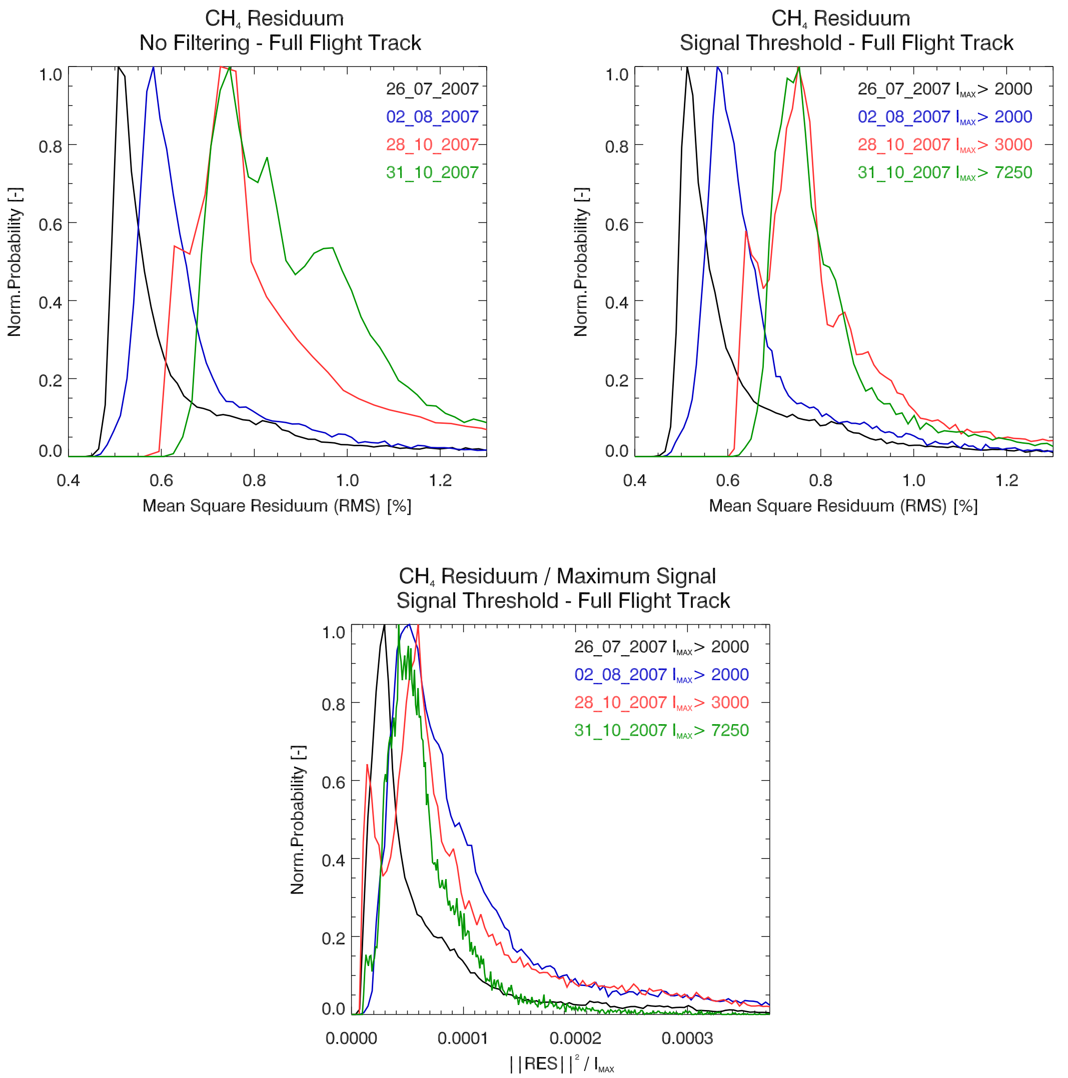

Figure 16: CH_4 Fit residuum histograms for the four 2007 flights. Left: Complete flight track dataset. Center: The data points with maximum signal lower than the threshold have been excluded. Right: Fit residuum normalized by the maximum signal value.

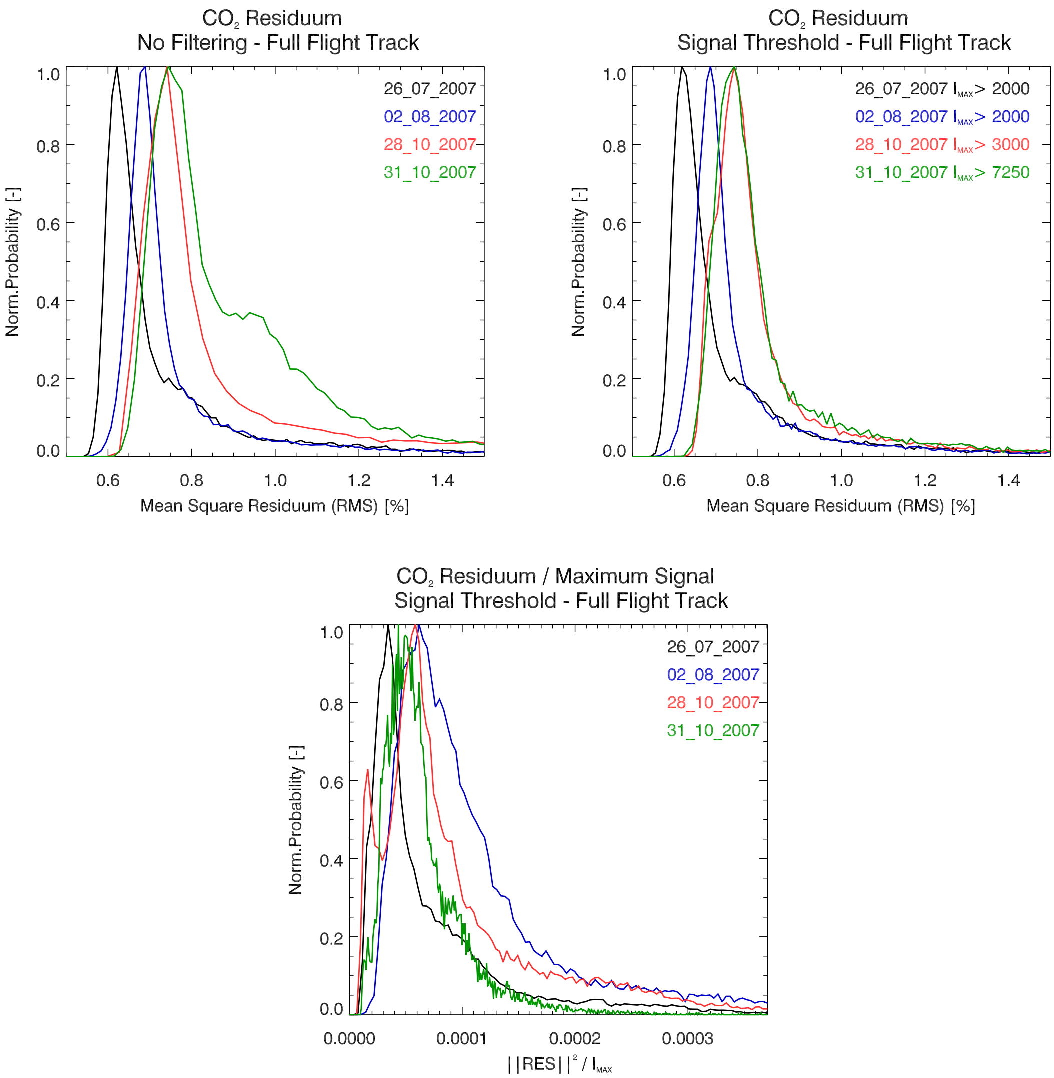

Figure 17: CO_2 fit residuum distributions for the four 2007 flights. Left: Unfiltered flight track dataset. Center: The data points with maximum signal lower than the threshold have been excluded. Right: Fit residuum normalized by the maximum signal value.

$$I_{max} = max_i\, I_i\ ,\ i = 1...N \tag{38}$$

As seen in Figures 16 (upper left) and 17 (upper left), the mean residuum distributions differ strongly between the summer and the autumn flights. The difference in the means would suggest a strong dependence on the solar zenith angle and the exposure time, both determined by the different season. In addition, the summer flights show a smooth and regular distribution, while the autumn flights present several peaks. This shape is typical of a sum of several distributions corresponding to different sets. In this case, the nonuniform cloud coverage conditions over the flight area in the autumn season could have led to distinct subsets, while the summer flights, performed in clear-sky conditions, would not have been affected. Detailed discussion follows in the next section.

Figure 16 (upper right) and 17 (upper right) show the results of a filter based on a threshold on the maximum signal: all the data points with $I_{max} < I_{max}^{thres}$ are rejected. I_{max}^{thres} is chosen ad hoc to isolate the main peak of the distribution, also by analysing the three-dimensional distribution in the I_{max} - $\|RES\|^2_{CH_4}$- $\|RES\|^2_{CO_2}$ space, according to the classification procedure introduced by Lillesand and Kiefer (2000). For the single target scenes instead three different thresholds on all three parameters are defined and used for the filtering.

The result is minimal on the summer flights, but a sharp narrowing occurs in the shape of the autumn RMS distributions, where most of the points with residuum higher than the main peak are excluded.

When the ratio between the fit residuum and the maximum signal is taken (cfr. Figs. 16 and 17, lower panel), the four histograms overlap, regardless of the season, and have very similar values for the peaks. From this it can be concluded that the most significant factor in determining the value of the fit residua is indeed the radiance level, as foreseen in the pre-flight noise analyses presented in Section 6. In addition, changes in the instrument performance between the flights can be excluded.

8.2 Multidimensional analysis and data classification: an example

To investigate further the origin of the different overlapping distributions in the CH_4 fit residuum, the three-dimensional distribution in the I_{max} - $\|RES\|^2_{CH_4}$- $\|RES\|^2_{CO_2}$ space is analyzed. The 31-10-2007 flight is chosen because it shows the most complex structure, and is an example of how the multidimensional analysis is performed on each dataset studied.

The first feature to be noted in the residuum - maximum signal scatterplots (Figure 18) is that the data is scattered along a hyperbole branch, highlighting the inverse proportionality between signal strength and fit error (cfr. Eq. **??**). Both the signal and the residuum distributions have lower boundaries larger than zero, as expected, because the dark current keeps the signal always larger than 800 counts, and random and systematic errors keep the residuum values above 0.6% for both variables. The two residua (upper right panel) show high correlation, but two different clusters can be observed, alignes along two different lines.

Clustering appears also in both residuum - maximum signal scatterplots, corresponding to the different peaks from the residuum histograms. The maximum signal then seems to be a good variable to separate the superimposed distributions observed in the residuum histograms. For example, in the CO_2 residuum - signal scatterplot two large clusters are evidently divided along the maximum signal axis, with the separation line at I_{max} = 7250 counts. The left cluster (with the lower signal values) in addition shows two "tails" with similar shape but different signal levels.

To isolate the different clusters the data points can be classified based on the three variables in the following way:

- Set B: $I_{max} > I_{max}^{thres}$
- Set R: $I_{max} < I_{max}^{thres}$ and $\|RES\|_{CO_2}^2 > a\ \|RES\|_{CH_4}^2 + b$
- Set G: $I_{max} < I_{max}^{thres}$ and $\|RES\|_{CO_2}^2 < a\ \|RES\|_{CH_4}^2 + b$

where I_{max}^{thres} = 7250 counts, a = -0.714 and b = 1.5.

The separation between the clusters is illustrated in Figure 19, with set B plotted in blue, set R in red, set G in green. This marks how set B on one side and the sets R and G on the other, separated by a threshold in the maximum signal axis, correspond to the two clusters in the CH_4-CO_2 residua scatterplot, where instead they overlap. Dividing the sets R and G along a line in the CH_4-CO_2 residua space, where the separation between the clusters is more evident, makes the internal structure visible also in the residuum - signal plots, where the set R corresponds to the tails, and the set G to the center of the cluster.

Figures 20 and 21 show how the three sets correspond as well to the three overlapping distributions visible in the histograms, that could not have been separated without recurring to a third variable.

What can be deduced from this analysis is that there is a variability in the noise levels, that can be observed in the fit residua. Its origin is still uncertain, but the influence of the maximum signal level, that is the detected radiance, points to physical processes along the light path. This constrains the possible causes to terrain reflectivity and absorption/scattering in the atmosphere. The fact that only the autumn flights show such structure and variability can suggest an influence of weather and illumination, rather than of ground type. This is also supported by the observation (cfr. Figure 22) that the three clusters isolated show a strong spatial pattern: most of the data points belonging to set R were measured in the Ketzin area, while most of the data collected on the other two targets (the power plants Jänschwalde and Schwarze Pumpe) is classified in set B. In the enlarged plot for Jänschwalde can be seen that the pixels downwind of the power plant are also classified as set R. This could be related to the cloud plume produced by the power plant exhausts. Since the data in the set R have a lower maximum signal than set B, this could then be caused by cloud shadows.

It can be tentatively affirmed than set B corresponds to clear-sky illumination conditions, and set R to lower illumination due to cloud shading. Confirmation of this hypothesis can be found by comparing the spatial pattern discovered with satellite imagery of water vapour content and cloud coverage, and by examining the images taken during the flight by the Observer system camera.

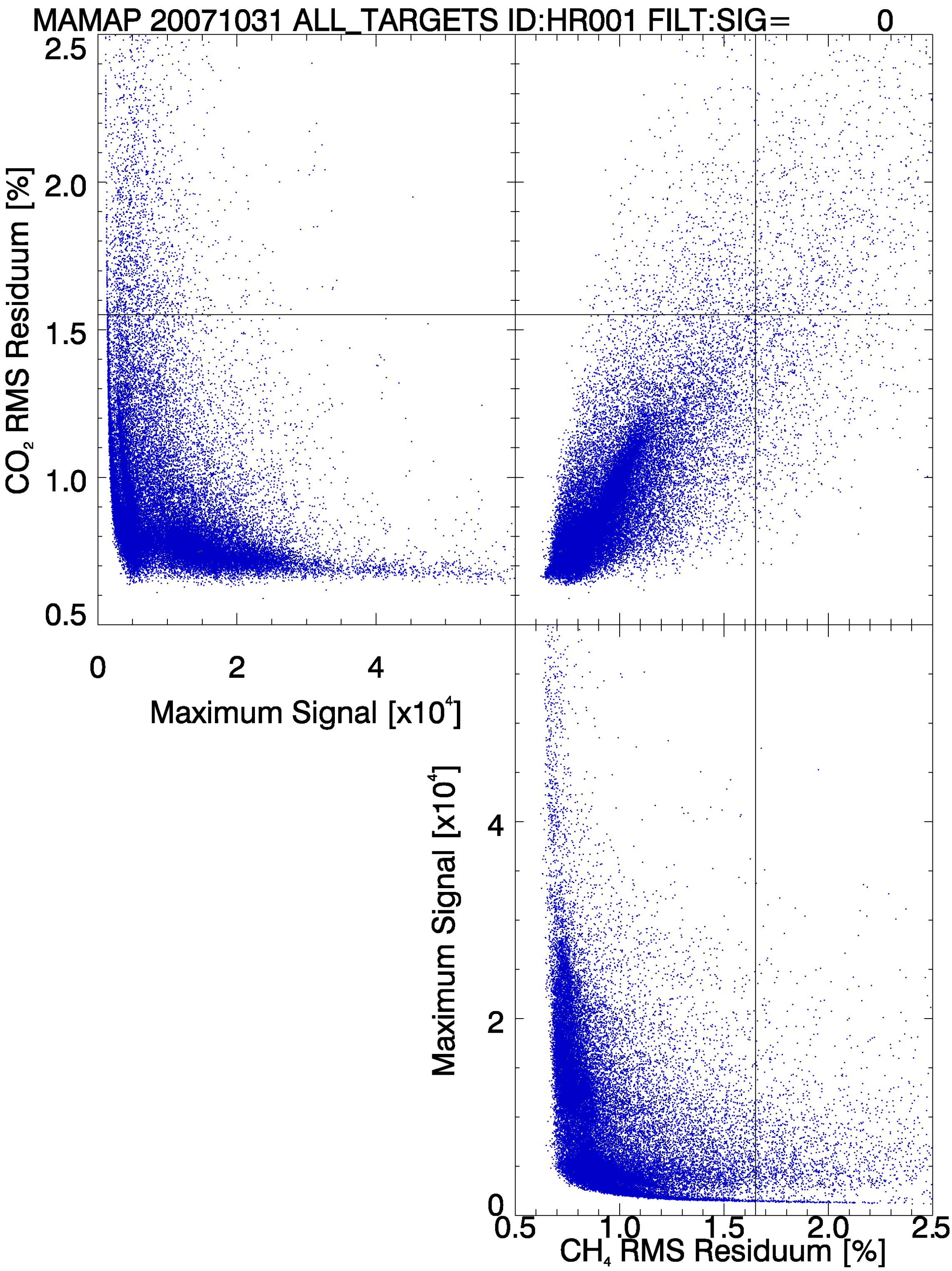

Figure 18: Three-dimensional scatterplot: CH_4 fit residuum - CO_2 fit residuum - Maximum Signal for the 31-10-2007 flight. The whole dataset is plotted in blue.

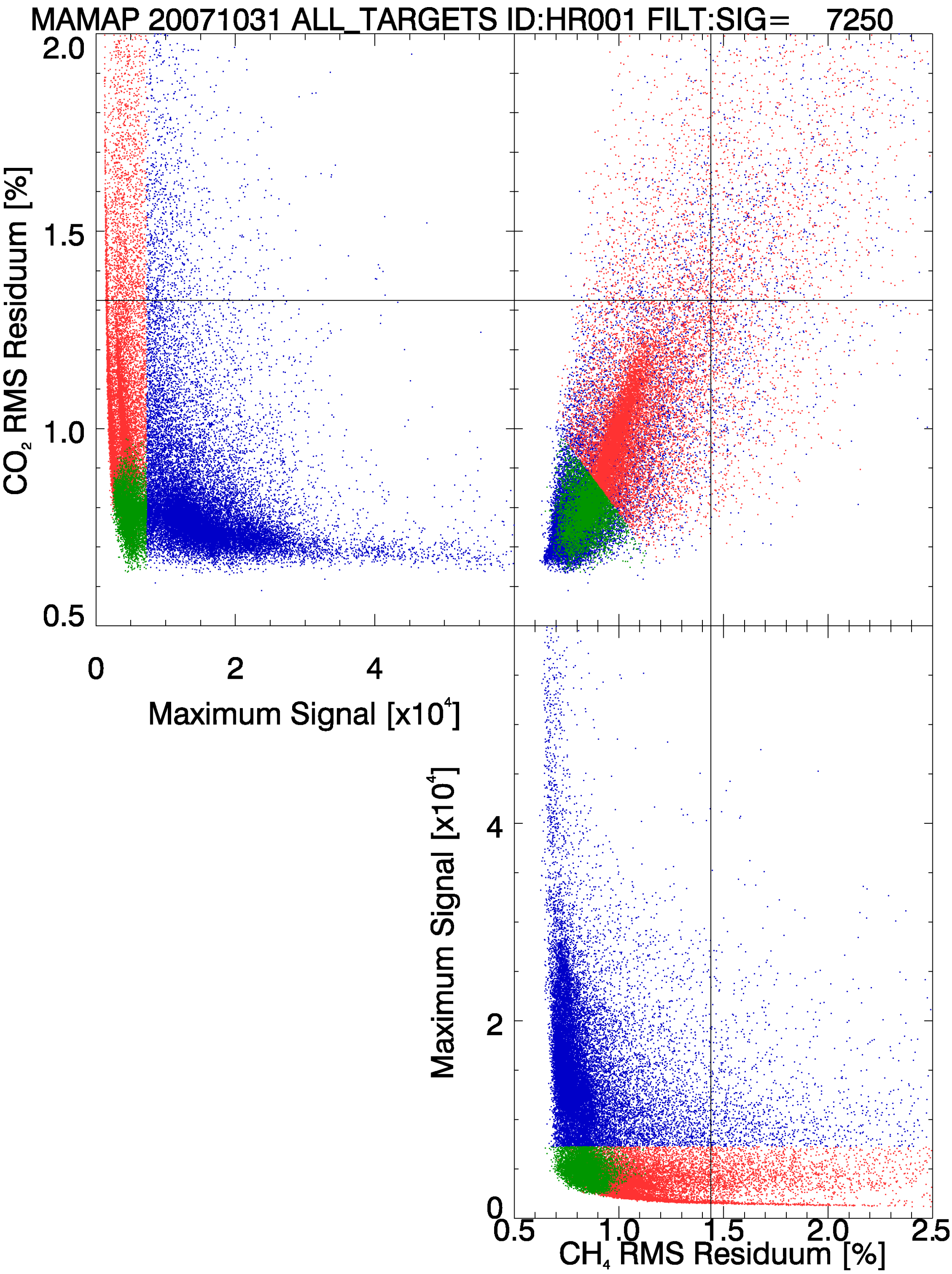

Figure 19: Three-dimensional scatterplot: CH_4 fit residuum - CO_2 fit residuum - Maximum Signal for the 31-10-2007 flight. The sets B, R and G are plotted respectively in blue, red and green (see text for details).

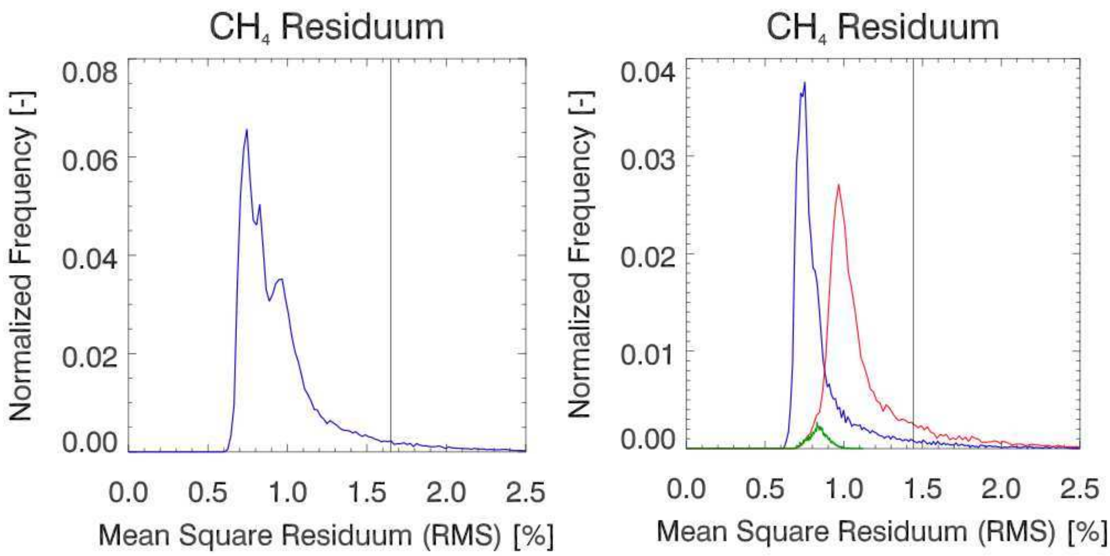

Figure 20: CH_4 residuum histograms for the 31-10-2007 flight. Left: histogram for the whole dataset. Right: histograms for the sets B, R and G are calculated separately.

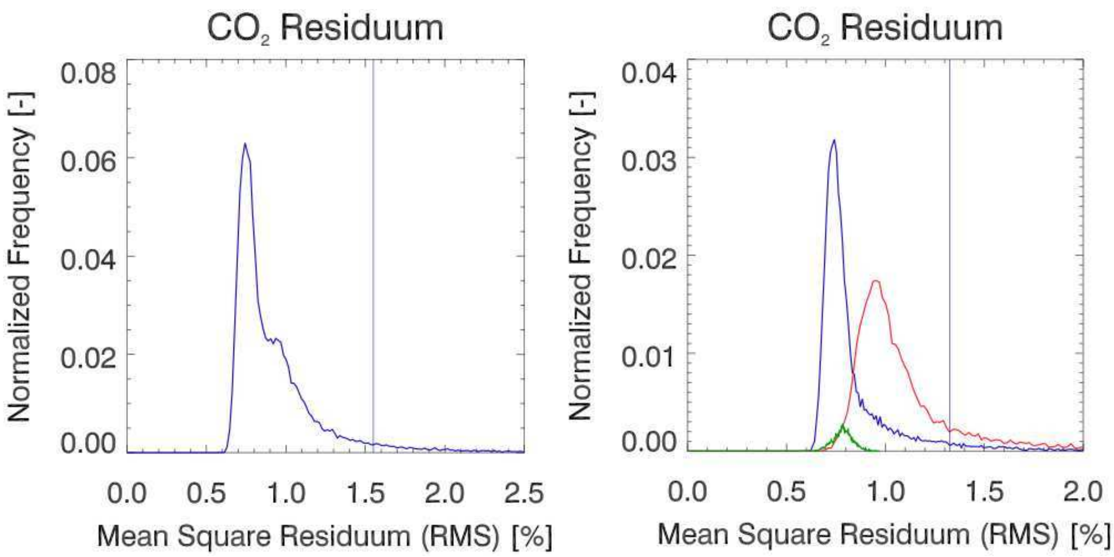

Figure 21: CO_2 residuum histograms for the 31-10-2007 flight. Left: histogram for the whole dataset. Right: histograms for the sets B, R and G are calculated separately.

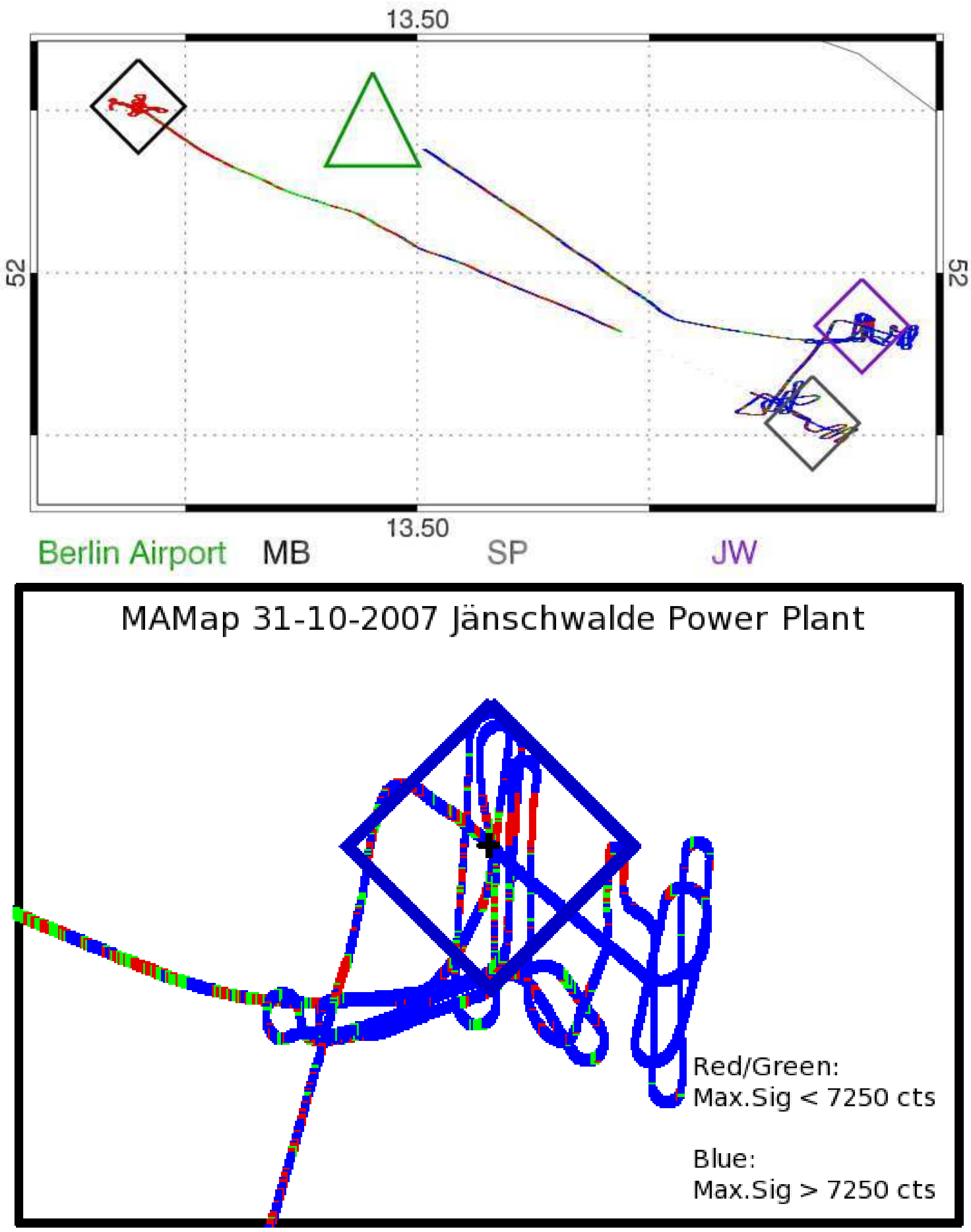

Figure 22: 31-10-2007 flight track. The colors (blue, red and green) correspond to the sets B, R and G (see details in Section 8.2). The Ketzin site is labeled as MB (methane bottle). The other two targets in the upper map are the power plants Schwarze Pumpe (SP) and Jänschwalde (JW). The lower panel shows a zoom of the Janschwälde power plant area. The power plant itself is marked by the black cross.

9 An anthropogenic carbon dioxide source: the Schwarze Pumpe coal power plant

The flight over the power plants Jänschwalde and Schwarze Pumpe, performed on 26-07-2007, has been planned to test the ability of the instrument to accurately scan a localized anthropogenic source of greenhouse gases. Both targets present a strong predictable signal, the CO_2 emission plume downwind from the power plant chimneys. In this work only the analysis of the flight over Schwarze Pumpe is presented, because the flight pattern is the most suitable to test the repeatability of the measurement, having several parallel tracks over the downwind plume (transects), nearly perpendicular to the wind direction. The goal is then to observe the CO_2 enhancement signal as clearly separated from the natural background.

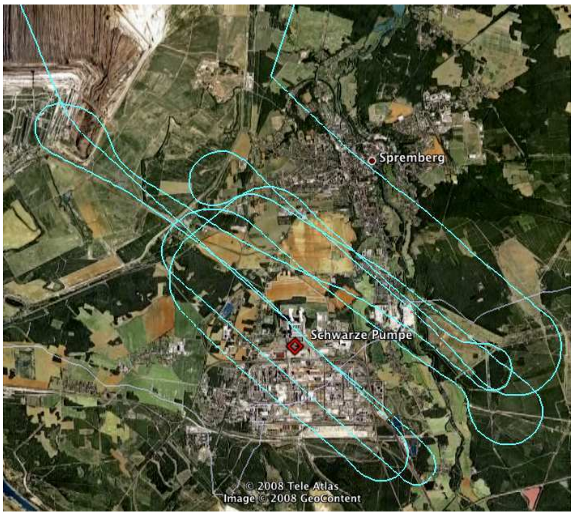

Figure 23: Schwarze Pumpe power plant. Flight track of 26-07-2007.

9.1 Target description

Position: Jänschwalde Power Plant: Near Cottbus, Spree-Neisse District, Brandenburg, Germany, approximately 9 km W of the Polish border, 105 km SE of Berlin.
Schwarze Pumpe Power Plant: Near Spremberg, Spree-Neisse District, Brandenburg on the border with Sachsen, Germany, approximately 70 km NE of Dresden, 130 SSE of Berlin.

Coordinates: Jänschwalde Power Plant:
Lat 51°50'11.94" N Lon 14°27 '31.12" E
Schwarze Pumpe Power Plant:
Lat 51°32'14.34" N Lon 14°21'07.45" E

Features: The Jänschwalde and Schwarze Pumpe are two coal power plants, property of Vattenfall Europe Mining and Generation. According to a report by Öko-Institut/WWF, Jänschwalde is the fourth most polluting coal power plant in Europe, the second in Germany, Schwarze Pumpe the 14th in Europe and the 7th in Germany (WWF, 2007). WWF and Vattenfall independently report the same CO_2 emission rate for both power plants, namely 1200 g CO_2 / kWh with a power generation of 3000 MW for Jänschwalde and 1000 g CO_2 / kWh with an power generation of 1600 MW for Schwarze Pumpe.

Flights: The 26-07-2007 flight covered Schwarze Pumpe with a windward overpass and several downwind overpasses at different altitudes (830 and 1250 m) between 10.10 and 10.45, and Jänschwalde at an altitude of 1250 m between 10.55 and 11.20. The high visibility due to the low humidity allowed an accurate observation of the targets. The reported wind speed during the flight was 8 knots, direction 250°. Vattenfall reported for Jänschwalde an average power generation between 8.30 and 11.30 of 2369 MW and an average CO_2 emission of 765 kg/s, and for Schwarze Pumpe of 1473 MW and 429 kg/s, respectively. This corresponds to average emission rates of 1162 g CO_2 / kWh (Jänschwalde) and 1048 g CO_2 / kWh (Schwarze Pumpe).
The 31-10-2007 flight also had several overpasses over these targets, but with low visibility conditions and a partial cloud coverage. Vattenfall reported an average power generation between 12.00 and 14.30 of 2911 MW and an average CO_2 emission of 936 kg/s (Jänschwalde), 1458 MW and 434 kg/s (Schwarze Pumpe). This corresponds to average emission rates of 1158 kg CO_2 / kWh (Jänschwalde) and 1071 g CO_2 / kWh (Schwarze Pumpe).

9.2 Expected signal strength

The relative enhancement of the total CO_2 column can be estimated from the known emission rates of the power plant. Let's assume that the power plant has a constant emission E (equal to 429 kg/s). According to the Verband der Elektrizitätswirtschaft (VDEW, 2000), the Schwarze Pumpe power plant has filters that allow the exhaust gases (for example CO_2) to be expelled through the cooling towers. They have a surface $L_1 L_2$ of 350 x 150 m, resulting in a CO_2 flux F equal to $8.17 \cdot 10^{-3}\ {}^{kg}/_{s\,m^2}$, that is $1.12 \cdot 10^{19}\ {}^{molecules}/_{cm^2\,s}$.

$$F = \frac{E}{L_1 L_2} = \frac{E}{L^2} \tag{39}$$

It is useful to define an effective length L, in this case $L = \sqrt{L_1 L_2} = 230$ m. A column of air moving with wind speed v spends over the power plant a time τ

I_{max}	$>$	2000 counts
$\|RES\|^2_{CH_4}$	$<$	1.628 %
$\|RES\|^2_{CO_2}$	$<$	1.575 %

Table 4: Filter specifications for the Schwarze Pumpe target, 26-07-2007 flight.

(accumulation time), during which CO_2 molecules get added to the column. For a wind speed of 8 knots, that is 4.11 m/s, the accumulation time is equal to L/v. The resulting time τ is 56 s. The CO_2 enhancement over the power plant is then $\Delta C = F\tau = 6.23 \cdot 10^{20}\ ^{molecules}/_{cm^2}$. Since the total atmospheric CO_2 column C has a value of $8.32 \cdot 10^{21}\ ^{molecules}/_{cm^2}$ (calculated from Trenberth et al., 1988) this results in a relative enhancement directly over the emission source of 7.5%.

$$\frac{\Delta C\,(S)}{C} = \frac{E}{CvLS_r} \tag{40}$$

It must be considered, however, that advection and diffusion mix the CO_2-enhanced air downwind of the power plant, so that the relative enhancement in the plume will be lower, roughly inversely proportional to the relative spread S_r of the plume. It can be defined as

$$S_r = \frac{S}{L} \tag{41}$$

where S is the spread, or width of the plume, and at the emission point $S = L$. Typical spreads for the signal detected during the flight (cfr. Fig. 26) are between 500 and 1000 m, so enhancements between 1.7% and 3.5% are to be expected.

9.3 Data selection and filtering

After selecting the target scene (coordinates 51.50º - 51.60º N, 14.26º - 14.45º E), the dataset has 9789 points. The fit residuum distributions are regular, even if highly asymmetrical, with a sharp peak at the median value (0.59% for CH_4, 0,68% for CO_2). The shape of the distribution can then be identified as only one cluster. This is consistent with the observation that the flight track doesn't cross any water body with a low surface reflectance. A maximum signal threshold of 2000 counts is chosen, a factor 2.5 larger than the average dark signal. The threshold for each of the fit residua corresponds to the 95th percentile, that is the 5% of the data with the largest residuum is excluded, so to exclude all the data points whose spectra differ significantly from the model. These criteria (thresholds on the signal and the residua) then exclude 7.0% of the data points. Cfr. Fig. 24.

9.4 Spatial analysis and comparison with ground type information

The flight track has been planned to accurately characterize the emission plume, with several overpasses at different distances. The best way to observe the shape of the plume in the data sequence is then to handle it as a time series, rather than as a two-dimensional map. According to the instrument design, at least 10 spectra must be averaged together to have the needed signal-to-noise ratio. A running average on 25 data points, then, has been chosen to smooth out the random noise components and highlight the plume shape. Figures 26 and 27 show the results for the CO_2 and CH_4 column factors, the CO_2/CH_4 ratio and the maximum signal.

Figure 28 instead features data interpolated and averaged on a square longitude-latitude grid with a 0.0035º cell size. The results have been superimposed on aerial photographs using the Google Earth software. This technique has been chosen to highlight the correlation between the collected data values (for example, the maximum signal) and the underlying terrain type.

9.4.1 Maximum signal

An analysis of the maximum signal levels is useful to check if the results are comparable with the pre-flight estimates, and the effect of terrain reflectance. The variability of the measurements, as seen in figure 27, ranges from 4000 to 20000 counts. This is coherent with the expected number of counts for albedos from 0.1 to 0.4. Moreover, the different signal levels correspond to different land covers: low signal levels (4000-8000 counts) are observed on forests, high levels (16000-20000 counts) are observed on sand and bare soil, while the other land covers (urban, agricultural) fill the middle range. It is also important to notice that in the transects area downwind from the power plant the signal is mostly constant, and as such large albedo effects on the column factors are not to be expected.

9.4.2 CO_2, CH_4 column factors, ratio CO_2/ CH_4

The first feature to be noticed by comparing the CO_2 and the CH_4 maps is that they are strongly correlated. This is due to all the processes influencing the light path (absorption, scattering, albedo, changing airplane geometry) that affect the spectra of CH_4 and CO_2 in the same way.

The CH_4 map show a large data scatter on short distances, that is a large spatial high-frequency component. In absence of evident localized sources, this variability may be attributed then to natural fluctuations in the gas mixing ratio. In the CO_2 map instead the signal changes much more smoothly, with a lower spatial frequency.

The signal from the plume is very well defined, stronger than any other variation in the series. Its position is also coherent with the measured wind direction, that is 250º (WSW), and stretching for at least 4 km from the emission point. It is indubitable that the power plant is the source of the signal, also because the flight track upwind from the target don't show any significant enhancement.

The map of the ratio CO_2/CH_4 doesn't show the data scatter from the two previous maps, that can be attributed to light path and geometry effects, but some still remains, due to the large spread in the CH_4 channel. The signal from the power plant is anyway evident.

9.5 Transects over the exhaust plume

The repeated overpasses downwind from the target are analyzed as data series. Five of these transects are chosen, being perpendicular to the exhaust plume. A new coordinate system is defined, with the target at the center, and the plume direction as one of its axes, so that the position of the plume is constant at zero, even for transects of different length. The axis and the positions of the transects are shown in Figure 24. The first three plots (Figures 29 to 31) show each filtered value of the relative anomaly (difference from the mean) for the CO_2, CH_4 columns and the CO_2/CH_4 ratio without averaging. This is to compare the data scatter to the fit error and the expected instrument noise.

In the CO_2 transects, a significant enhancement can be seen at the position of the plume, but it is on the same level of the random scatter along the whole transect. No enhancement is present in the CH_4 transects, but the same large scatter seen in the maps is evident here, with many outliers with deviation from the mean larger than 10%, and propagated to the CO_2/CH_4 transects. It is interesting to note how in all three cases the scatter is much lower in coincidence with the plume signal. The amplitude of the signal is between 3% and 6%, in accord (or even slightly higher) with the column enhancements calculated in Section 9.2.

As expected for single measured spectra with an exposure time of 58 ms, the fit errors are larger than the deviation from the mean for most of the points. The CH_4 fit has namely a smaller error (∼2%) than the CO_2 fit (3.2-3.4%), and the CO_2/CH_4 ratio (∼4%). This is also coherent with the pre-flight estimates. The fit errors from the flight data, however, are 2 to 3.5 times larger than the ones estimated from instrument noise. This may be attributed to many systematic biases affecting the retrieval fit, mainly inaccuracies in the modeled spectra.

To reduce significantly the errors, the transect values x_i can be averaged on a constant grid (with a size of 0.0035º). The error of the averaged values $\bar{x}$ then can be calculated as:

$$\sigma_{\bar{x}} = \frac{1}{N}\sqrt{\sum_{i=1}^{N}\sigma_{x_i}^2} \approx \frac{\sqrt{N}}{N}\sqrt{\sigma_x^2} = \frac{\sigma_x}{\sqrt{N}} \tag{42}$$

where the approximation is valid if the errors have similar values ($\sigma_{x_i} \approx \sigma_x;\ \forall\, i = 1...N$). The results are shown in Figures 32 to 34. The errors of the gridded data are about 5 times smaller than for the single measurements, namely ~0.7% for CO_2, ~0.4% for CH_4 and ~0.8% for the ratio CO_2/CH_4.

The plume signal is now more evident in both the CO_2 and the ratio transects, and well above the error range. It can be seen how the signal gets repeated over several transects in a coherent way, and changes amplitude and spatial extension with the distance from the target. The shape of the plume can then be recognized.

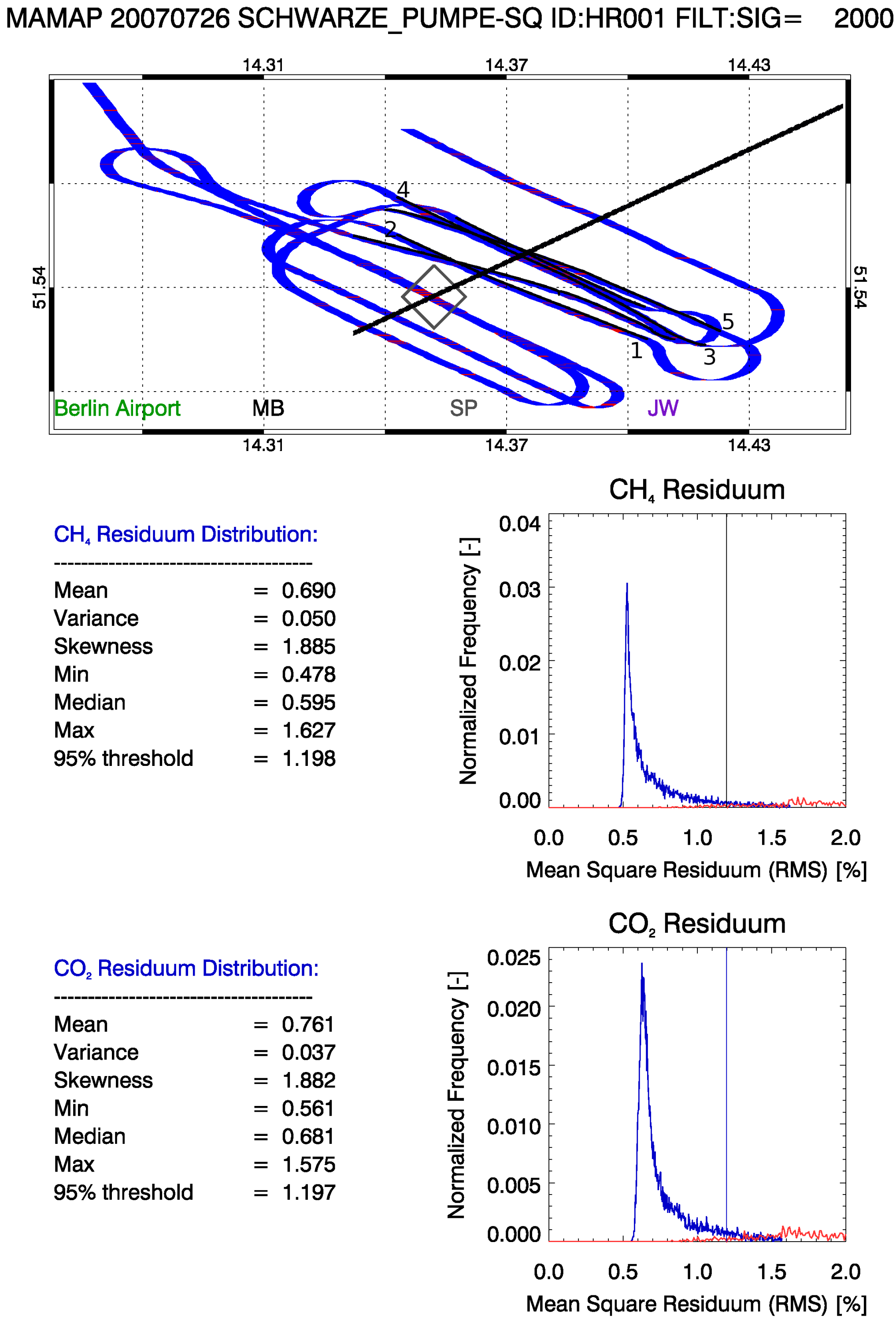

Figure 24: Filtering for the Schwarze Pumpe target, flight of 26-07-2007. Red represents the data filtered out. On the top, map of the flight track. The numbered sections of the flight track are the transects described in Section 9.5. The axis of the coordinate system is also marked. On the right, frequency histograms of the fit residua. On the left, statistics of the dataset used for the analysis, post filtering.

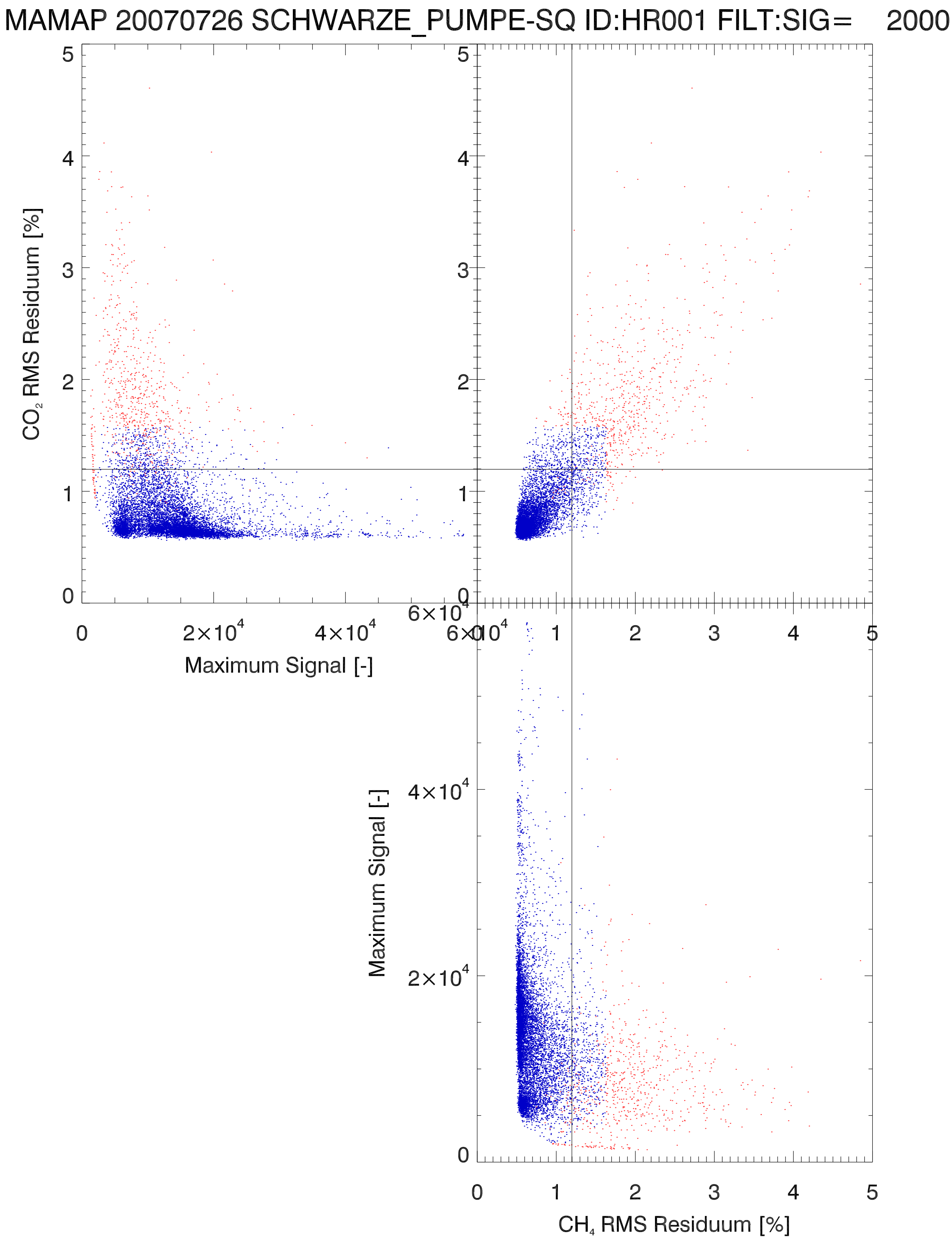

Figure 25: Three-dimensional scatterplot for the Schwarze Pumpe target, flight of 26-07-2007. The valid data points are displayed in blue, the ones filtered out in red.

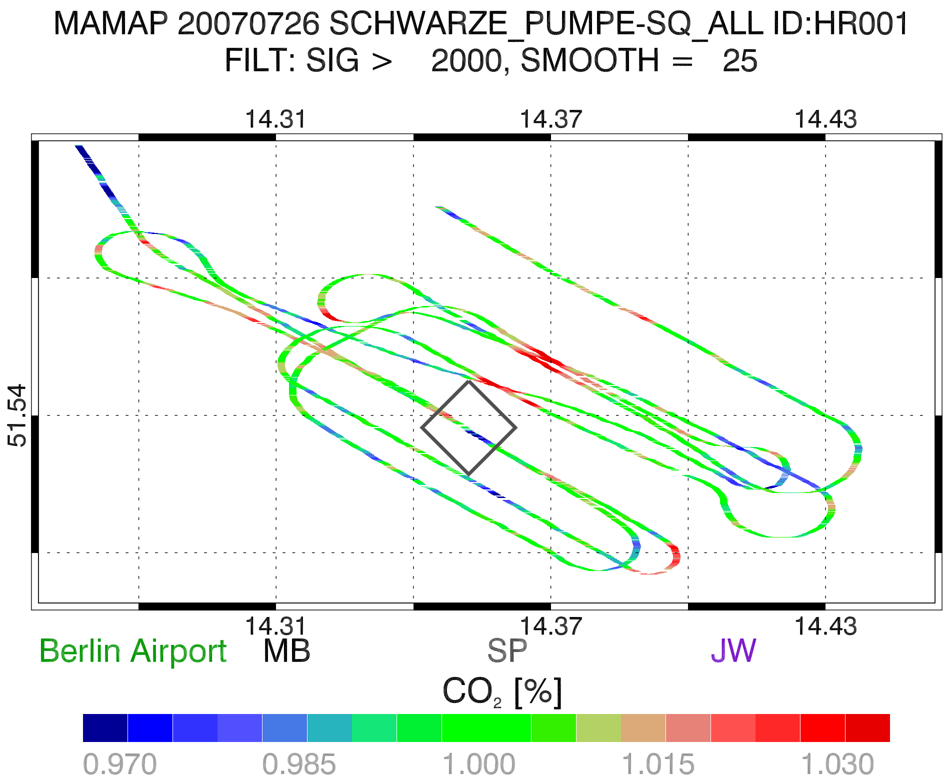

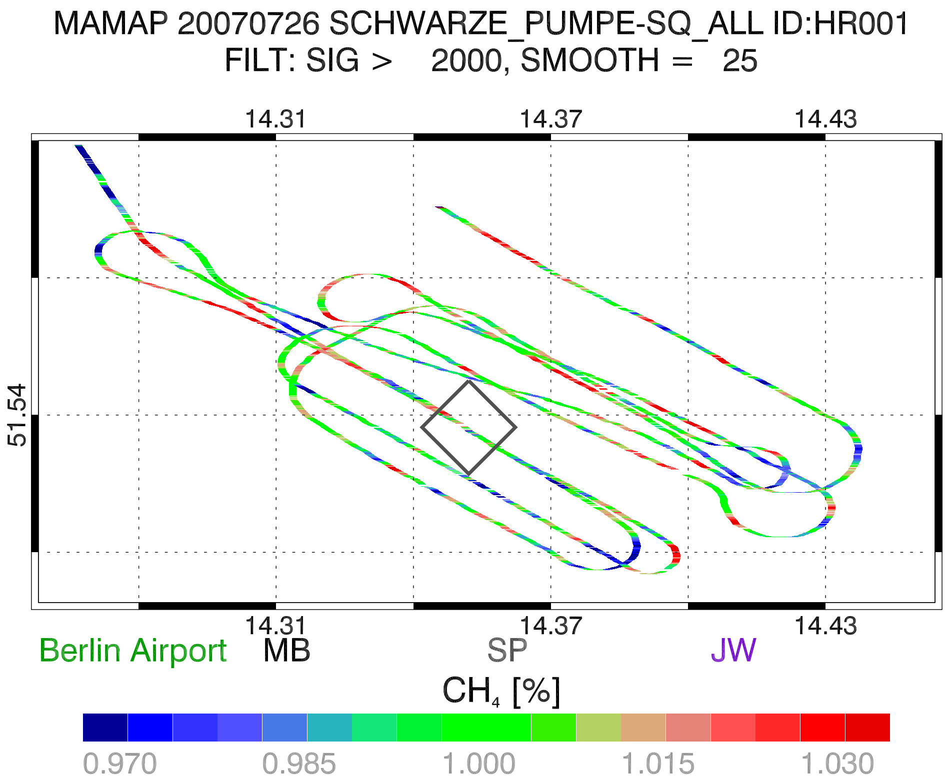

Figure 26: Schwarze Pumpe - 26-07-2007. Above: CO_2 column factor map. Below: CH_4 column factor map. Both column factors are expressed as relative to the mean value for the whole flight.

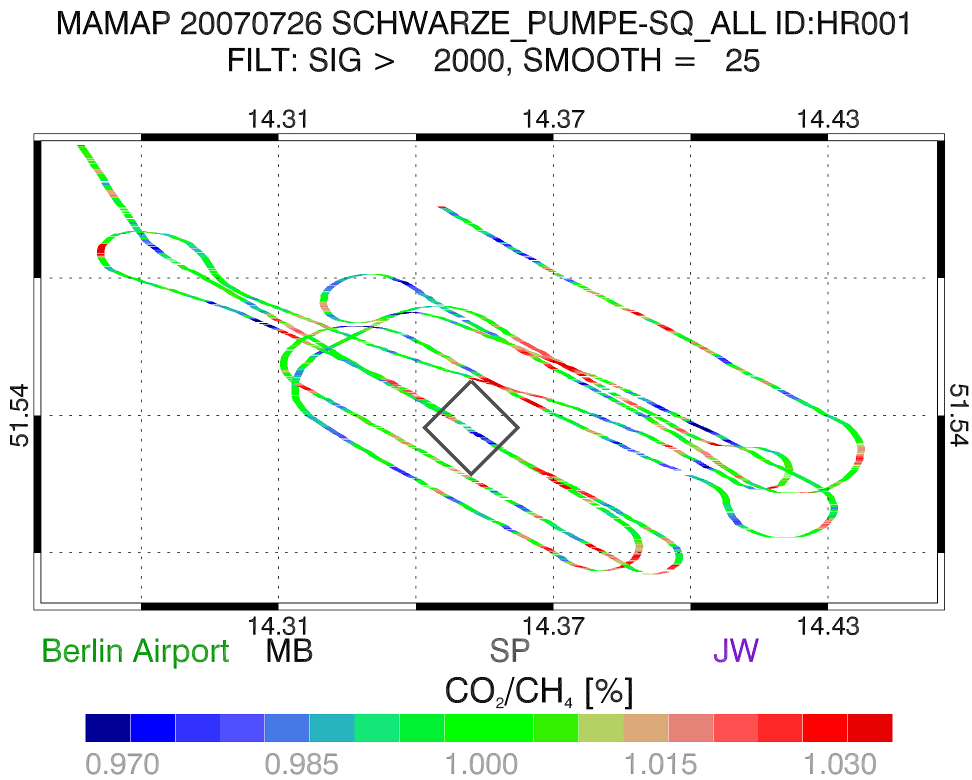

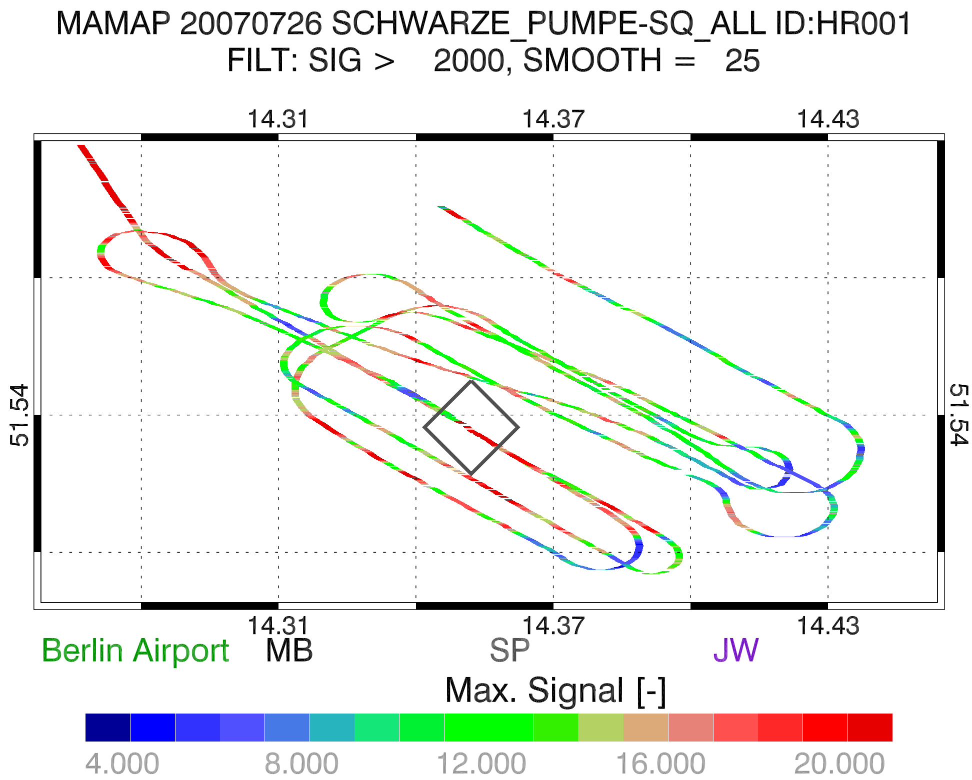

Figure 27: Schwarze Pumpe - 26-07-2007. Above: CO_2/CH_4 column factor ratio map, expressed as relative to the mean value for the whole flight. Below: maximum signal map.

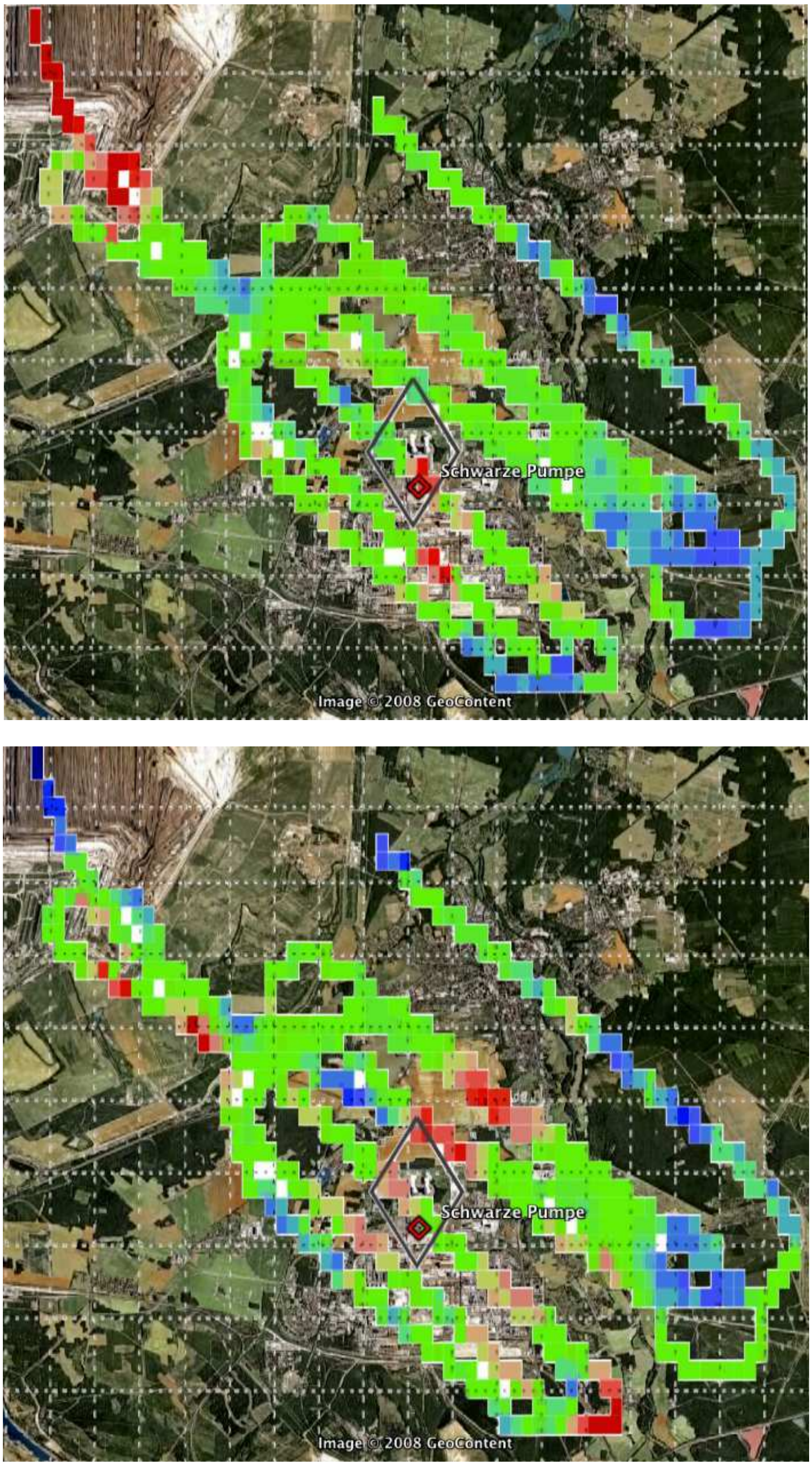

Figure 28: Schwarze Pumpe power plant. Flight of 26-07-2007. MAMap data superimposed on aerial imagery.
Above: Maximum signal. Scale: 4000-20000 counts.
Below: CO_2 column. Scale: $\pm$ 3 %

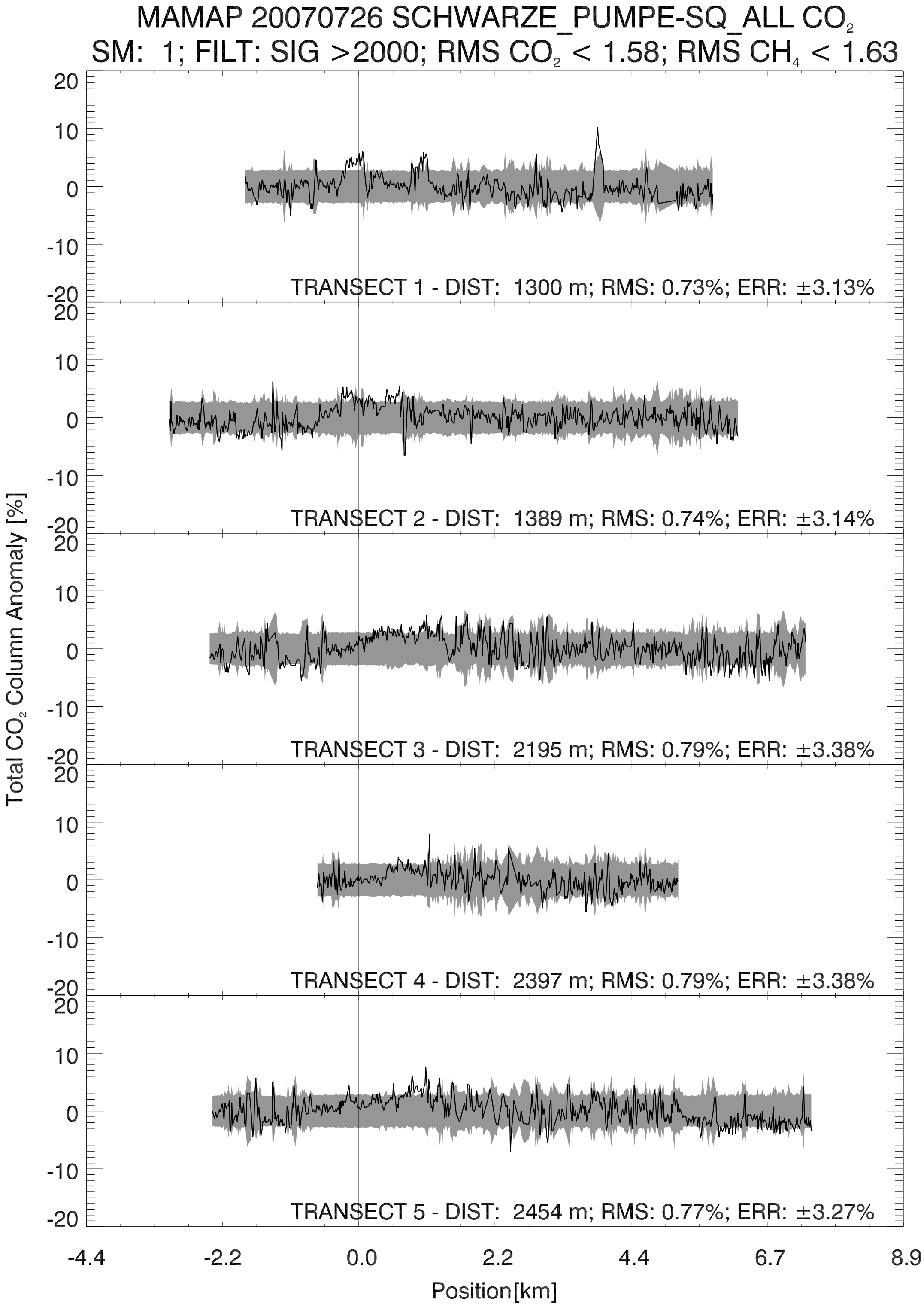

Figure 29: Schwarze Pumpe power plant. Flight of 26-07-2007. Relative anomaly in the CO_2 column factor over the exhaust plume. No data averaging, all the valid data points are displayed. The scale of the position variable starts from the plume itself. The error range from the average value is displayed in grey.

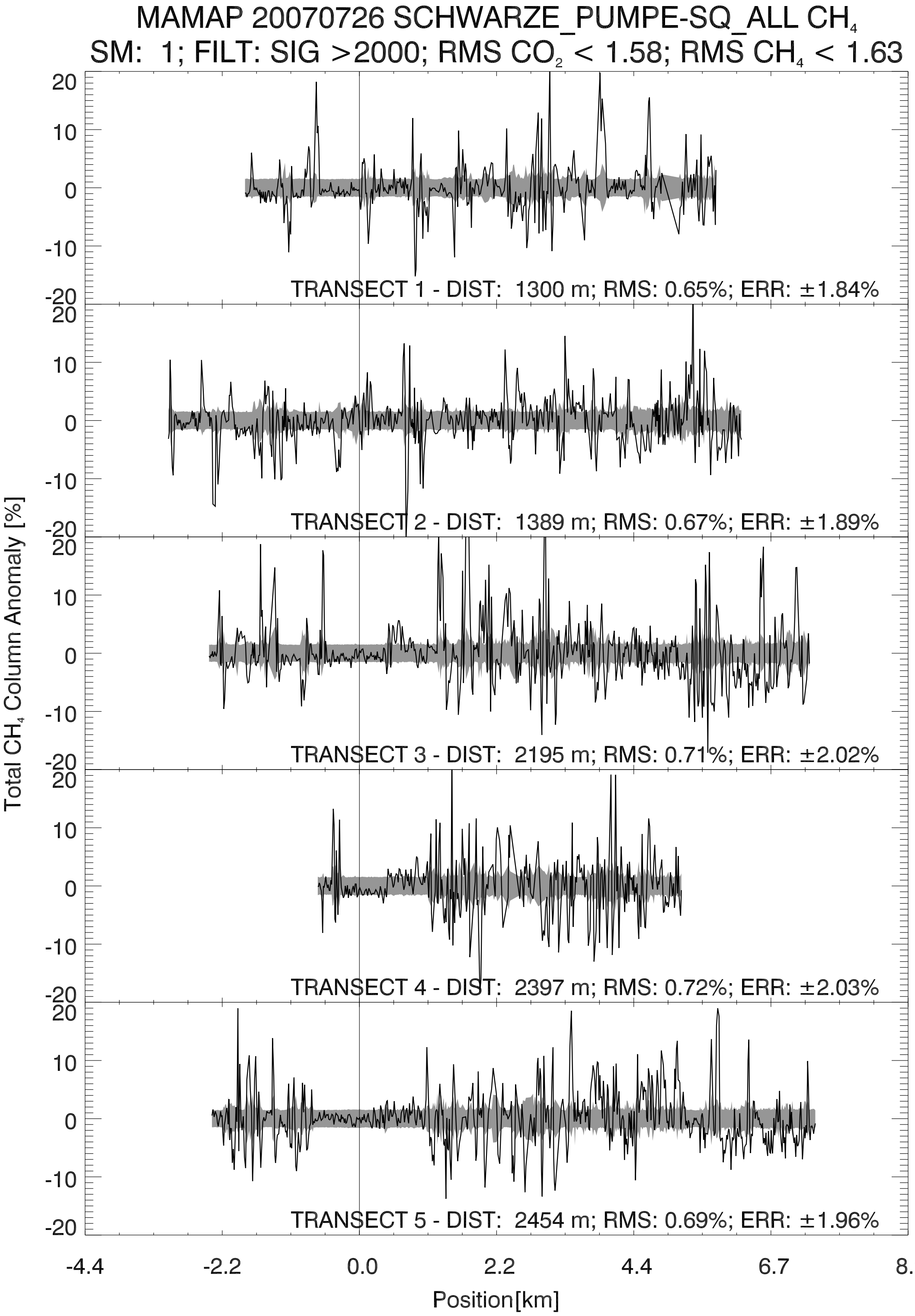

Figure 30: Schwarze Pumpe power plant. Flight of 26-07-2007. Relative anomaly in the CH_4 column factor over the exhaust plume. No data averaging, all the valid data points are displayed. The scale of the position variable starts from the plume itself. The error range from the average value is displayed in grey.

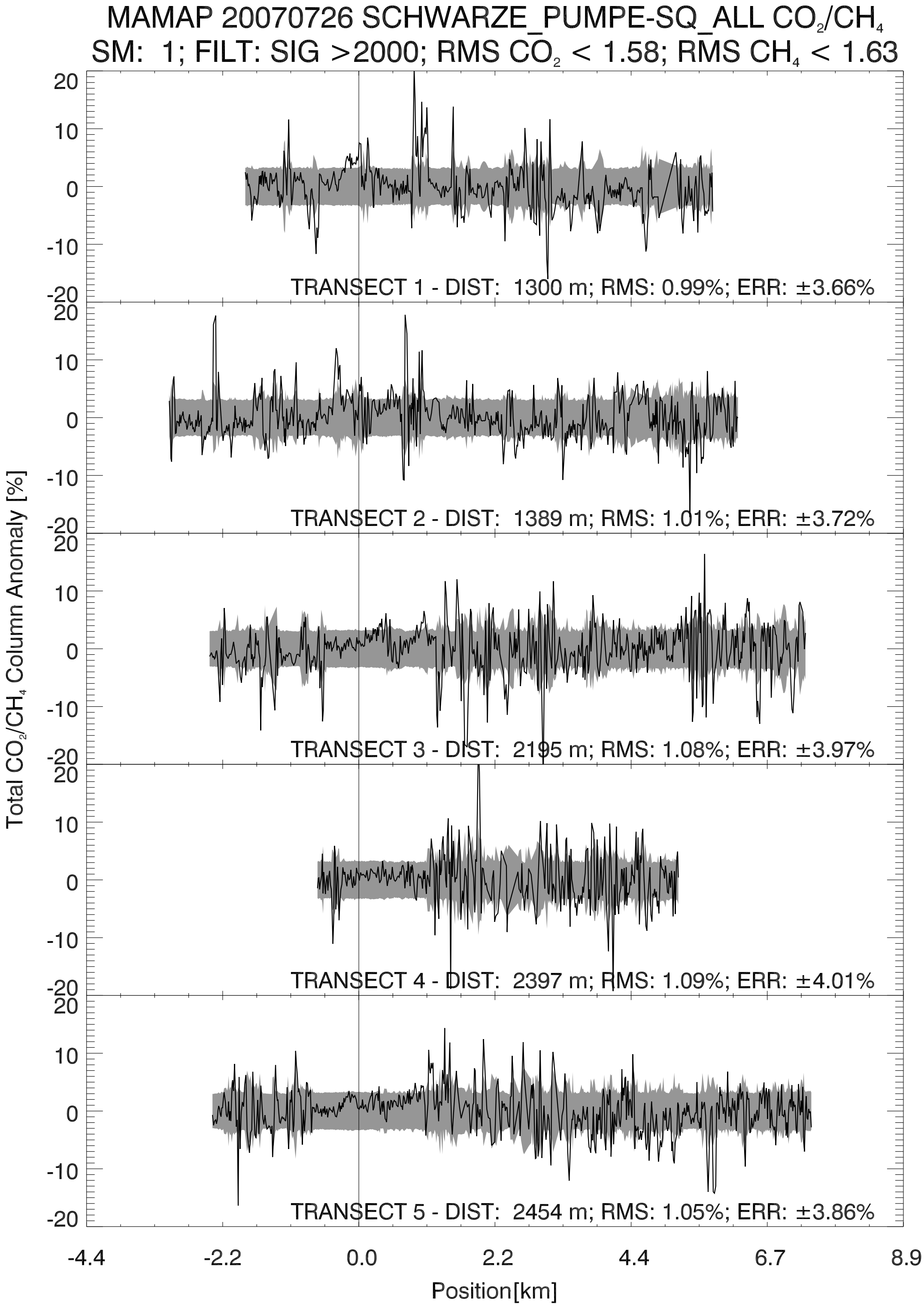

Figure 31: Schwarze Pumpe power plant. Flight of 26-07-2007. Relative anomaly in the CO_2/CH_4 column factor ratio over the exhaust plume. No data averaging, all the valid data points are displayed. The scale of the position variable starts from the plume itself. The error range from the average value is displayed in grey.

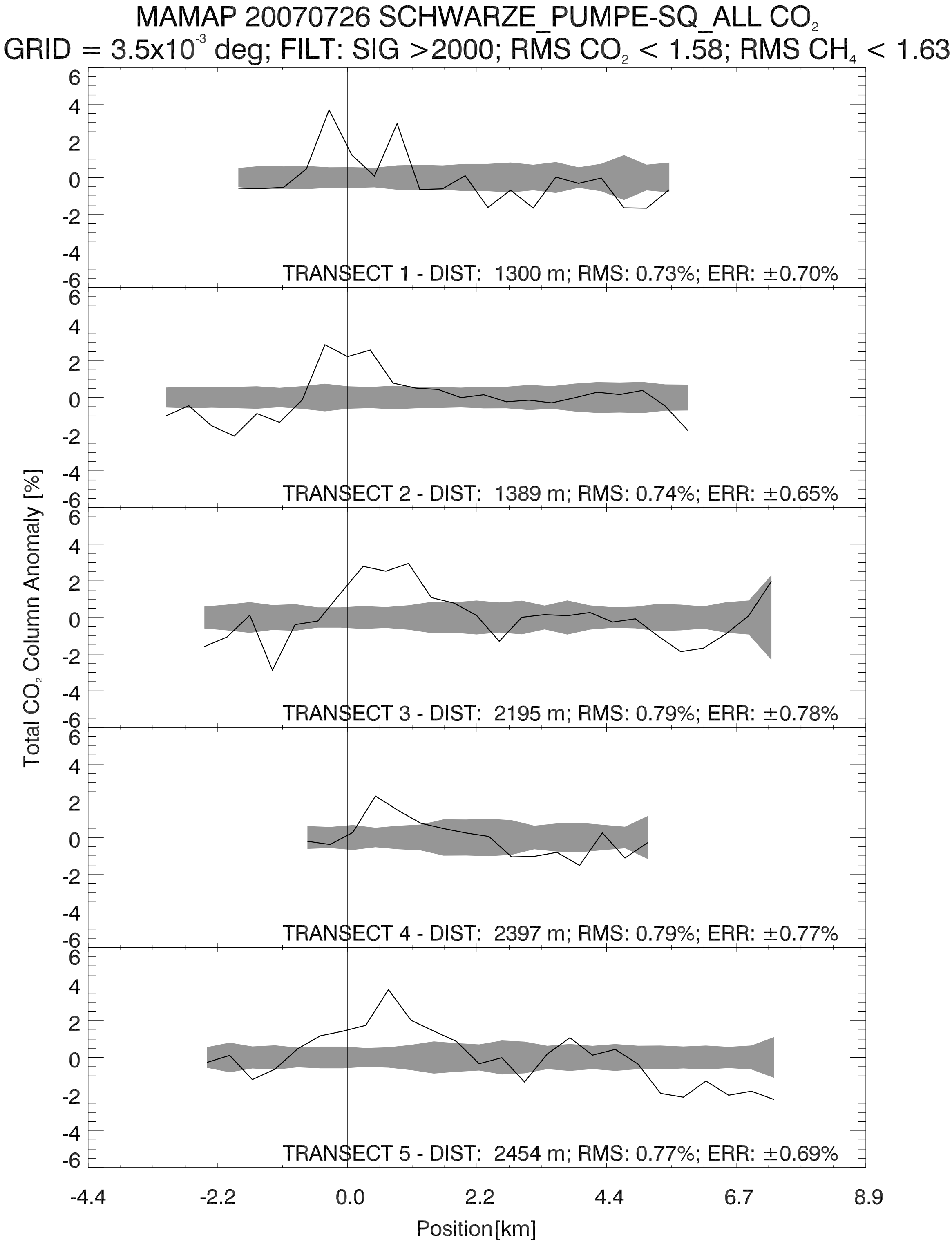

Figure 32: Schwarze Pumpe power plant. Flight of 26-07-2007. Relative anomaly in the CO_2 column factor over the exhaust plume. Data averaged on a constant grid of 0.0035º size. The scale of the position variable starts from the plume itself. The error range from the average value is displayed in grey.

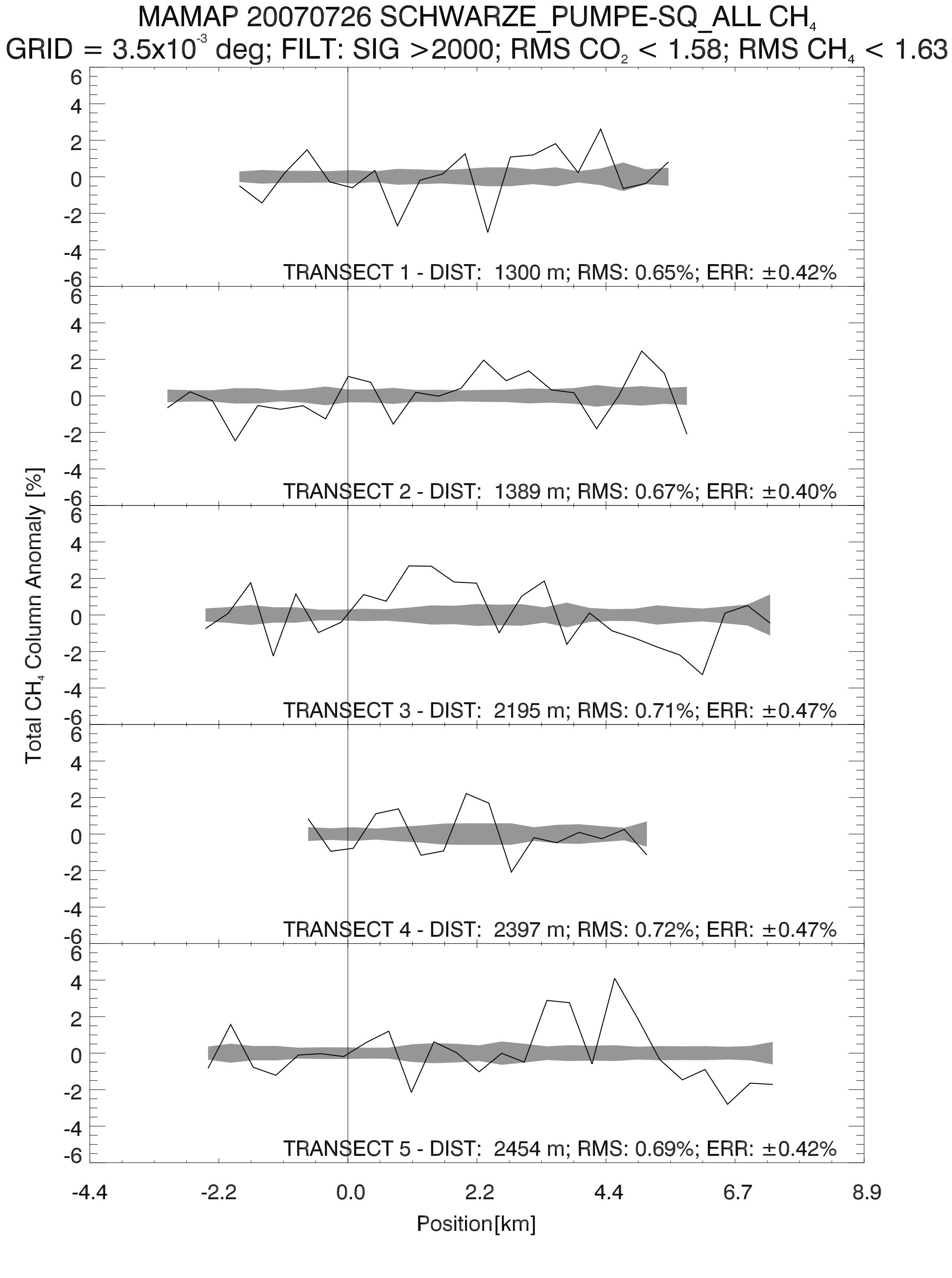

Figure 33: Schwarze Pumpe power plant. Flight of 26-07-2007. Relative anomaly in the CH_4 column factor over the exhaust plume. Data averaged on a constant grid of 0.0035º size. The scale of the position variable starts from the plume itself. The error range from the average value is displayed in grey.

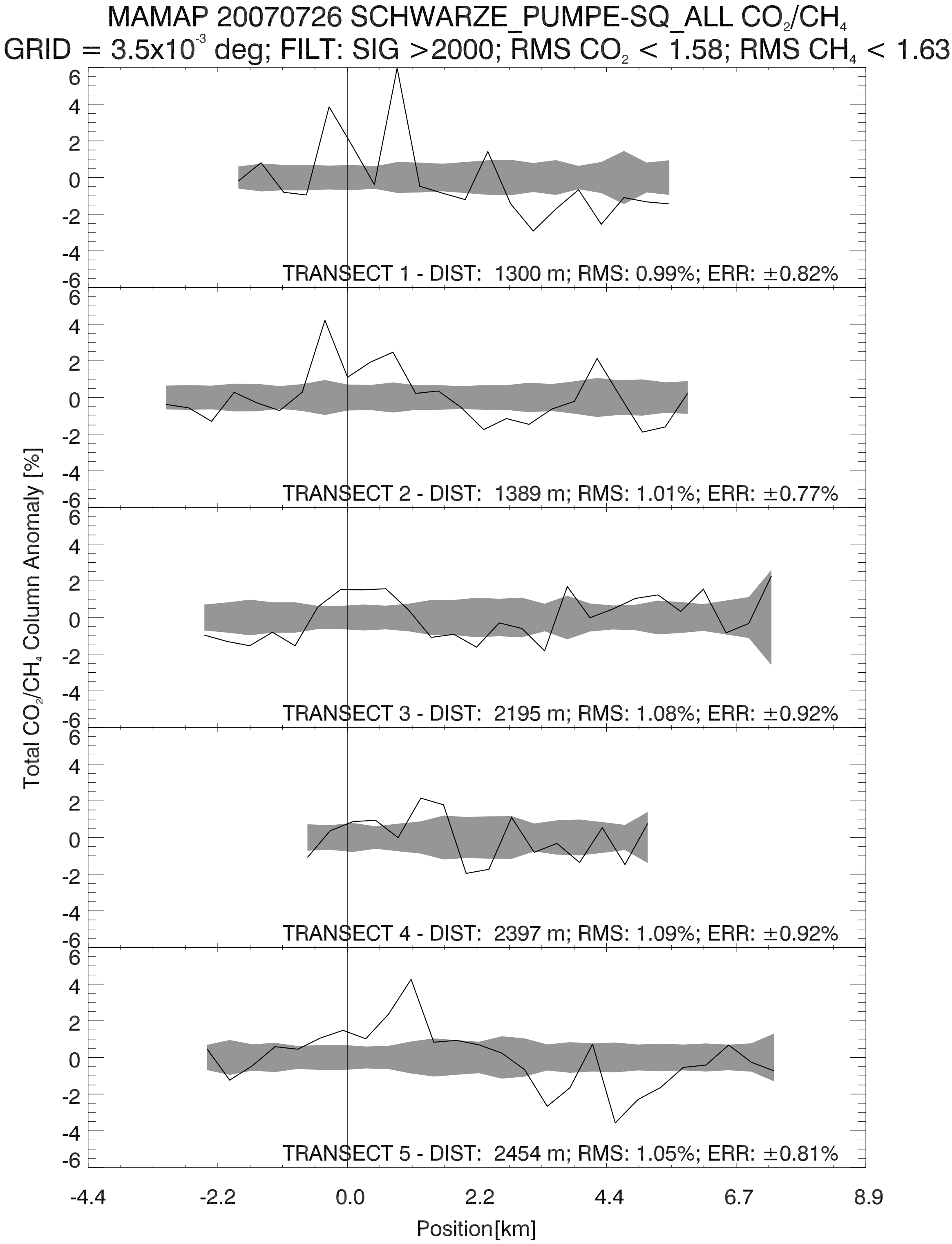

Figure 34: Schwarze Pumpe power plant. Flight of 26-07-2007. Relative anomaly in the CO_2/CH_4 column factor ratio over the exhaust plume. Data averaged on a constant grid of $0.0035^{\underline{o}}$ size. The scale of the position variable starts from the plume itself. The error range from the average value is displayed in grey.

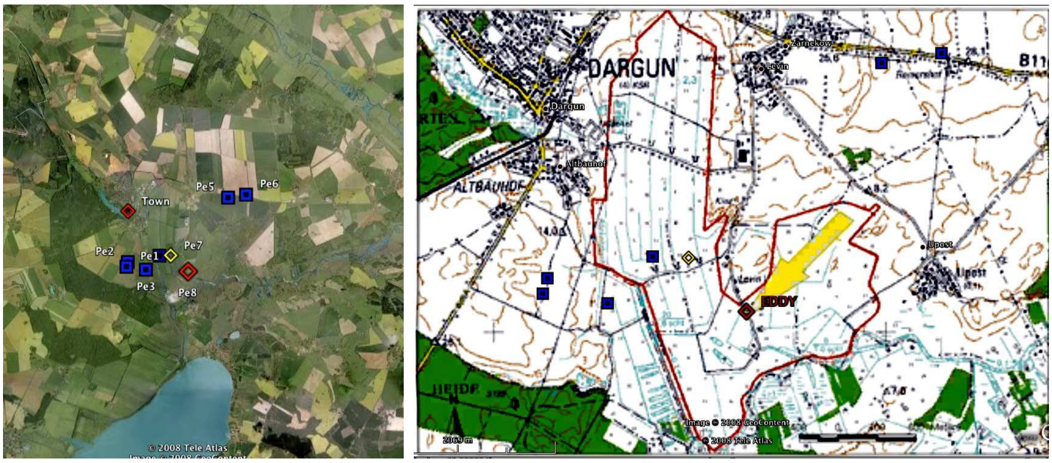

Figure 35: The Peenetal /Zarnekow wetland area, with the targets of the 24-06-2008 flight. The left panel is an aerial photograph of the region. Measurement sites 1 to 8 are marked. The right panel is a topographic map with (in red) the extension of the marshland.

10 A natural methane source: the Zarnekow wetland

The MAMap project has as its main goal the characterization of natural methane sources. The first target chosen to test the capability of the instrument to observe and characterize such a source is the Zarnekow wetland site. In June 2008, the Institute of Environmental Physics (Bremen) and the Helmholtz Centre Potsdam - German Research Centre for Geosciences conducted a joint experiment with the Leibniz Centre for Agricultural Landscape Research (ZALF - Müncheberg), and the University of Greifswald to correlate the MAMap observations with ground-based measurements. This work presents the results of the flight performed on 24-06-2008, with two main goals for the analysis. The first is to verify if methane enhancements, even of small magnitude, follow a consistent spatial pattern correlated with the land cover. The second is to test the repeatability of the measurements, by following several times the same flight trajectory.

10.1 Target description

Position: Near Dargun, Demmin District, Mecklenburg-Vorpommern, Germany, approximately 55 km SEE of Rostock, 155 km NNW of Berlin.

Features: The target is a flooded marshland in northeastern Germany. The Leibniz Centre for Agricultural Landscape Research (ZALF - Müncheberg) support two permanent micrometeorological measurement sites (Site 7 and 8, see below). At

Site	Latitude [º]	Longitude [º]	Altitude [m]
1	53.87799670	12.85665745	60.18
2	53.87947136	12.85738626	54.80
3	53.87706718	12.86710518	41.72
4	53.88153919	12.87440169	38.91
5	53.89998143	12.91142995	64.62
6	53.90090320	12.92111559	69.14
7	53.88133536	12.88012893	–
8	53.87623453	12.88952489	–

Table 5: Geographical coordinates of the measurement sites at the Zarnekow wetland target.

Site	Land cover	CH_4 Emissions	CO_2 Emissions
1	Wheat, in maturation	weak sink	weak sink
2	Corn, green	weak sink	strong sink
3	Dry marsh grassland, cut	weak sink	strong source
4	Wet marsh grassland, cut	weak source	weak source
5	Wheat, in maturation	weak sink	weak sink
6	Corn, green	weak sink	strong sink
7	Dry marsh grassland, uncut	weak sink	strong sink
8	Flooded marsh grassland	very strong source	very weak source

Table 6: Land cover and expected greenhouse gas emission balance for the measurement sites at Zarnekow. (ZALF, 2008)

each site an automatic closed-dome gas detector system measures the mixing ratio of methane and carbon dioxide close to the ground. In addition, the University of Greifswald maintains an eddy-covariance system for the estimate of methane and carbon dioxide fluxes at Site 8. For the June 2008 campaign six additional measurement sites (Sites 1-6) have been selected according to their vegetation and their expected emissions of methane and carbon dioxide (cfr. Tables 5 and 6).

Flights: Two flights have been performed on this target. The first has been on 28-10-2007 between 12.30 and 14.30 (local time). According to the flight plan, the gas columns over the two sites should have been measured separately with different overpasses, parallel and perpendicular to the wind direction. The prevalent wind direction was about 210°, so SWS, while the average windspeed was between 1 and 2.5 m/s. A good visibility was reported. It is worth noting that during this flight measurement over an open water area were performed, useful to investigate the behavior of the instrument with low albedo scenes, and over a complete cloud cover,

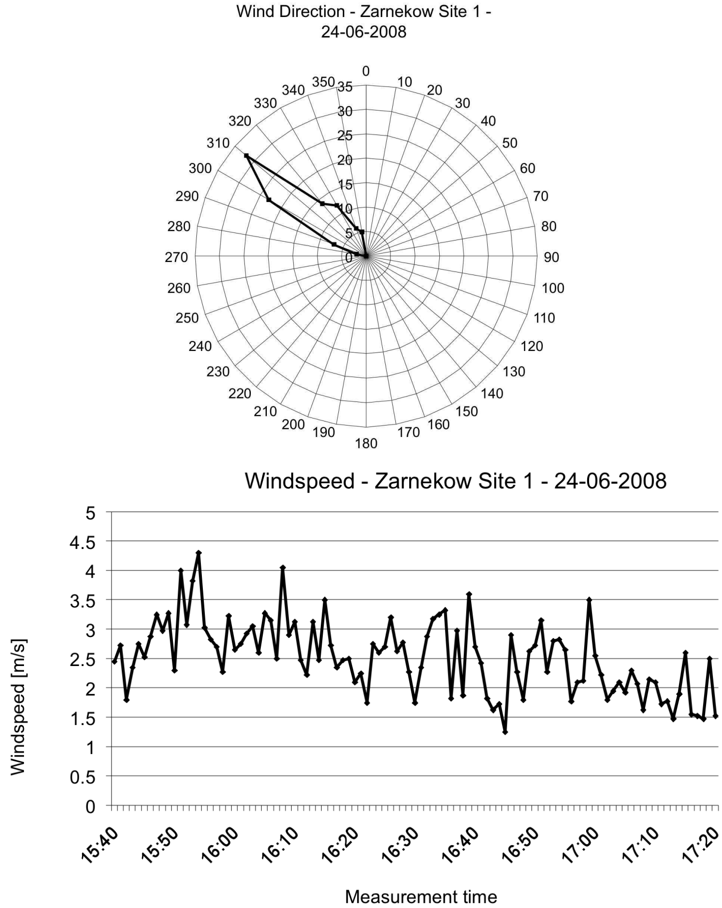

Figure 36: Wind parameters at the Zarnekow site 8 during the 24-06-2008 flight.

also useful to investigate the spectral response with a scenario radically different from the one considered by default.

The second one, covered in this work, took place on 24-06-2008 between 15.40 and 17.20 GMT. The averaged windspeed decreased during the flight from 3 to 1.5 m/s. The average wind direction was 310º (NW). The presence of small cumulus formations has been reported and documented. The flight track has been chosen to cover uniformly the small region around the target, in order to detect the presence of stable methane enhancements. Moreover, to explicitly test the repeatability of the measurements, the same trajectory has been repeated several times.

10.2 Expected signal strength

The strength of the CH_4 signal can be estimated based on data previously collected.

On 13-07-2007 methane ground concentrations and fluxes have been measured on Site 7 and 8. The two sites differ for morphology and methane production rate. Site 8 is in a newly flooded wetland, with permanent water cover, with a high methane flux (the carbon flux from CH_4 measured was 3-20 mg C_{CH_4} / (m^2h)). Site 7 is in a seasonally flooded wetland, that during the campaign in autumn 2007 was only

	Ground-level CH_4 mixing ratio
Site 7	1750 - 2000 ppb
Site 8	1790 - 3000 ppb

Table 7: Ground level CH_4 mixing ratios measured at the Zarnekow wetlands on 13-07-2007.

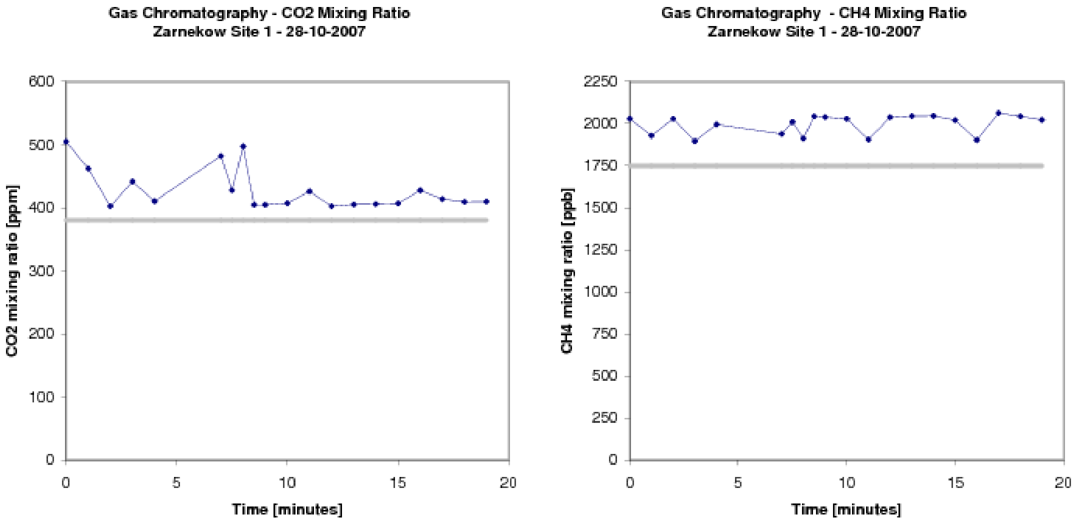

Figure 37: Gas chromatography measured mixing ratios of CO_2 and CH_4 at Zarnekow Site 1, on 28-10-2007. Time is expressed in minutes since 13:00. In grey is shown the mean global mixing ratio (380 ppm for CO_2 and 1750 ppb for CH_4).

partly flooded. This causes a smaller methane production rate, flux and ground mixing ratio (see Table 7).

During the flight on 27-10-2007 a scientific team of the University of Greifswald, measured the CH_4 emission from Site 8, with a value of 4.80 mg C_{CH_4} / (m^2h). The CH_4 mixing ratio in the air blown from Site 8 was around 1850 ppb (Lars Kutzbach, personal communication). The gas chromatography measurements performed in-situ at Site 8 report for the time interval between 13:00 and 13:20 a mean CO_2 mixing ratio of 428 ppm and mean CH_4 mixing ratio of 1998 ppb (Jürgen Augustin, personal communication).

These ground measurements can be upscaled using the estimates from Section 5.2. Against a background of 1750 ppb, the expected total column enhancements range from 0.5 to 3%, depending on the meteorological conditions, that is the possibility of accumulation. The actual background value, however, could be higher due to advection of methane from neighbouring regions, or the presence of diffuse

I_{max}	$>$	2000 counts
$\|RES\|^2_{CH_4}$	$<$	3.54 %
$\|RES\|^2_{CO_2}$	$<$	3.30 %

Table 8: Filter specifications for the Zarnekow target, 24-06-2008 flight.

natural sources. For this reason, the relative enhancement could be even smaller, due to the small difference with the background.

10.3 Data selection and filtering

In the target area (coordinates 53.81 - 53.96 N, 12.77 - 13.06 E) have been collected a total of 27161 valid spectra. The three-dimensional fit residuum scatterplot (Fig. 39) shows that both the CH_4 and CO_2 residuum distributions are regular, but with a very long tail, that is fit residua up to 18%, for very low values of the signal. When all the spectra with a maximum signal lower than 2000 are excluded, it appears evident how most of them were measured over the lake south of the target (Cfr. Fig. 38).

After selecting then only the data points with a residuum lower than the 95% percentile for both variables, as reported in Table 8, the number of data points reduced to 23510, so the percentage of excluded data is 13.8%.

10.4 Spatial analysis and comparison with ground type information

10.4.1 Image manipulation and enhancement

As mentioned before, since the position and the nature of this target is not clear in advance, the choice is to analyze it with a full two-dimensional approach, so to interpolate the data on a regular longitude-latitude grid, with a cell size of 0.0035º.

The first test to assess whether some systematic methane enhancements are present above the noise is to filter the resulting map with a two-dimensional neighborhood averaging, so to smooth out the variability below a given size, and check if any stable patterns remain. A moving window of 3x3 pixels is chosen for this purpose.

Since the flight took place in the late afternoon, the change in the solar zenith angle during the flight itself had a significant influence on the gas columns, so strong to mask every other source of variability acting on shorter time-scales. To minimize the impact of the slowly-changing illumination, a high-pass filter is applied to the data series, using a running average with window equal to 2000 spectra (approximately 100 s) and dividing the series by the averaged one. All quantities then are expressed as relative enhancements, that is relative to the average of a 2000 points neighbourhood.

10.4.2 Maximum signal

As can be seen in Fig. 39, the measured counts range from 2000 (lower boundary set with the threshold) to around 28000. The largest part of the dataset, however, assumes values under 13000 counts. This observation is in agreement with the assumed albedo for the target scene, that is between 0.1 and 0.2. Figures 41 and 42 show how the flight track over the lake was excluded by the filtering process due to its low reflectance. The pixels with a low signal (blue in the maps) correlate with the wooded areas. It is not clear instead which land cover correlates with the pixels with a higher signal level. This is due to the fact that the aerial imagery used for comparison was not taken at the same time of the measurements. Further information can be retrieved by the analysis of the Observer CCD camera pictures.

10.4.3 CO_2, CH_4 column factors, ratio CO_2/ CH_4

After the moving average filtering, most of the variability with a high spatial frequency is smoothed out. This is particularly evident in the CH_4 and CO_2 maps, that bear such a striking resemblance to let think that only the light path effects are emphasized. Since the smoothing was applied after taking the ratio, the CH_4/CO_2 map carries most of the relevant information.

First of all, it must be noted that the variability of the smoothed ratio has a smaller amplitude, ranging from -1% to +1%. Then, averaging together several different overpasses over the same point seems to shift the pixels toward a mean value. This can be explained by assuming a low correlation in time of the values of the same pixel, that is that natural mixing and wind advection change the local gas mixing ratio between one measurement and the next. A stable enhancement can be observed in the area southwest of Sites 7 and 8, that is in the marshland between the two branches of the Peene river. This seems to confirm the expected high methane emissions from the flooded area.

To explain thoroughly the full observed variability, however, a comparison would be needed with the gas mixing ratios measured at the ground, and the expected emissions for each of the measurement sites.

10.5 Comparison of repeated overpasses

According to the campaign plan, the airplane flew five times in a row over Site 8 on the same southwest-northeast trajectory, at two different altitudes. This allows to compare the different transects with each other, and eventually with the ground data. Figures 43 to 48 show the values for CH_4, CO_2 and the CH_4/CO_2 ratio along each of the transects, first for each single spectrum, then interpolated on a regular longitude grid (size 0.0025º). The altitudes of the transects are significantly different: 0.4-0.5 km for transects 1-3, 1 km for transect 4, 1.7 km for transect 5.

As seen by the analysis of the maps, the CH_4 and CO_2 series taken separately have a very similar shape, due to the light path effects. As for the Schwarze Pumpe flight (Section 9), however, the data scatter for the CH_4 fit is higher than for the CO_2 fit. By calculating the standard deviation of the data points from the mean, he scatter along the transects can be estimated between 4% and 5% for CH_4 and between 2% and 3% for CO_2. Compared to the expected error from the measurement noise, it shows that the measured variability is 3-4 times larger than the noise. It is still difficult, however, to establish how much of this is due to an effective variation in the gas concentration in the atmosphere and how much is due to biases, like light path effects. In the case of CH_4, in particular, the repeated variations both as increase and as decrease of the column on the order of 20% can be hardly explained as physical fluctuations. The scatter of the CH_4/CO_2 ratio is lower than for CH_4 alone (4%), because some light path effects get canceled. The fit error ranges for the gas columns are slightly higher than for the Schwarze Pumpe flight (CH_4 2.3-2.9%, CO_2 3.7-4.3%), and increase with the increasing altitude.

The CH_4/CO_2 averaged plot (Fig. 48) is the most significant, since it shows clearly the presence of repeated patterns and the impact of flight altitude. Transects 1 to 4, for example, show the same dip in the ratio at longitude 12.885º. The same peak appears in transects 1 and 4 at 12.94º, and in transects 2 and 4 at 12.84º. Transect 5 instead doesn't seem to correlate in any way with the other, lower ones. This could indicate that the CH_4 and CO_2 enhancements didn't propagate up to 1.7 km altitude, but were damped by atmospheric mixing.

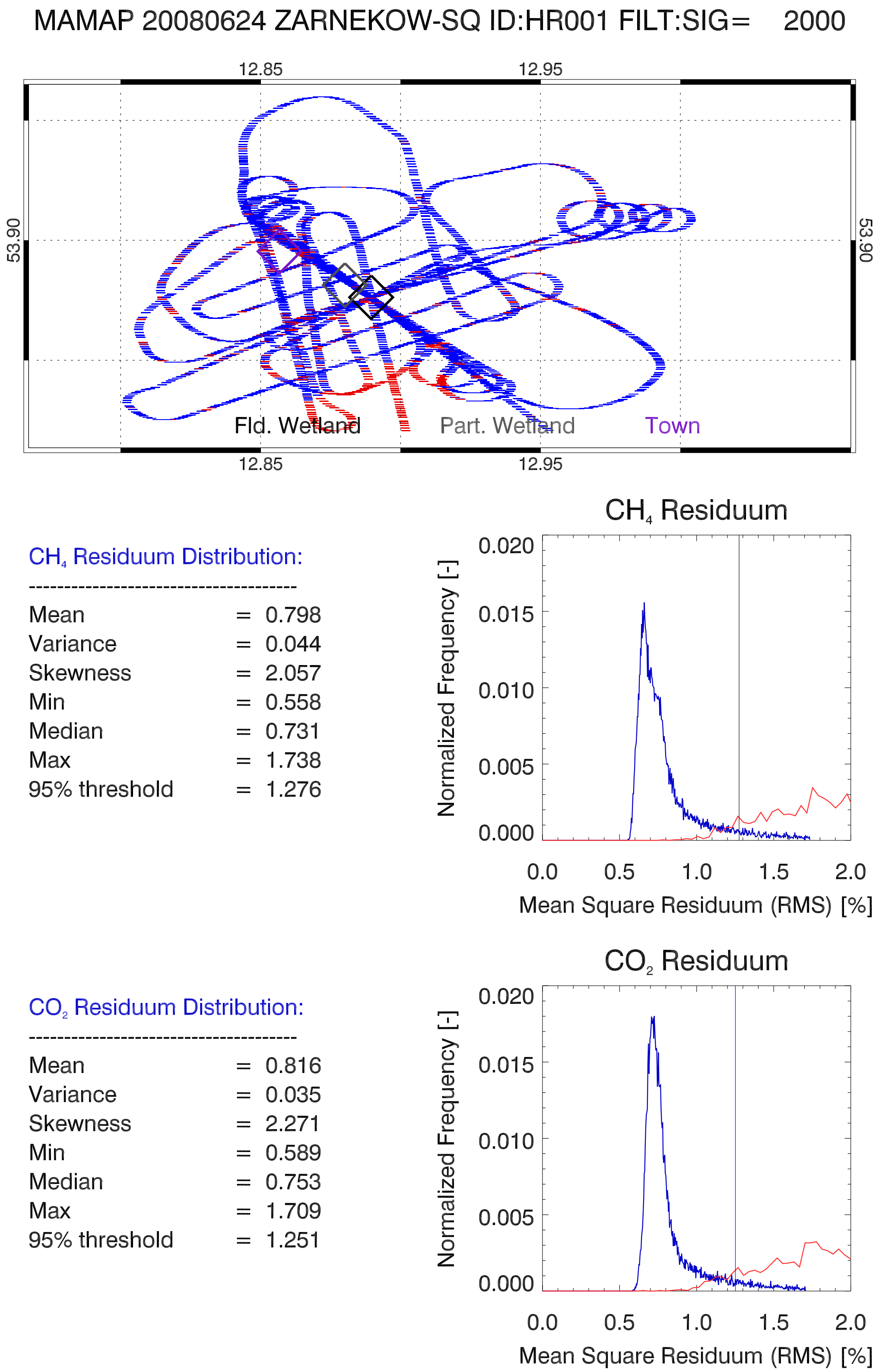

Figure 38: Filtering for the Zarnekow target, flight of 24-06-2008. Red represents the data filtered out. On top, map of the flight track. On the right, frequency histograms of the fit residua. On the left, statistics of the dataset used for the analysis, post filtering.

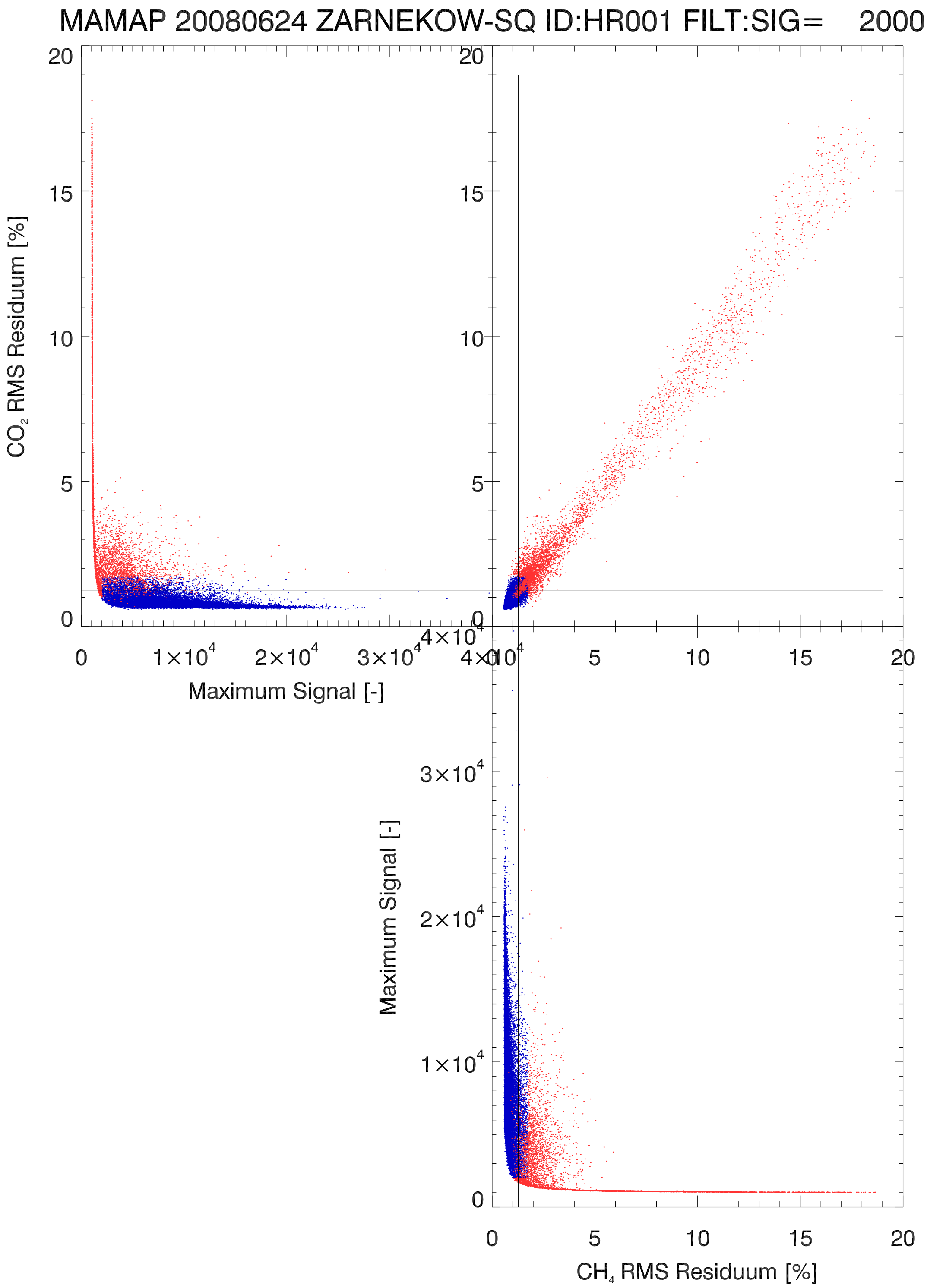

Figure 39: Three-dimensional scatterplot for the Zarnekow target, flight of 24-06-2008. The valid data points are displayed in blue, the ones filtered out in red.

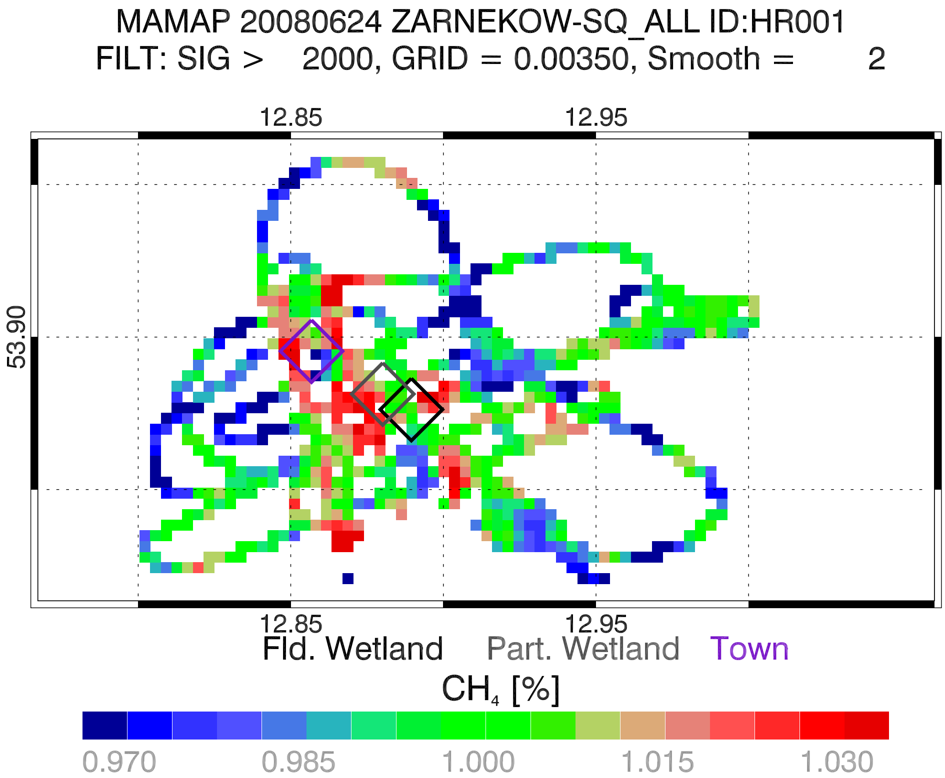

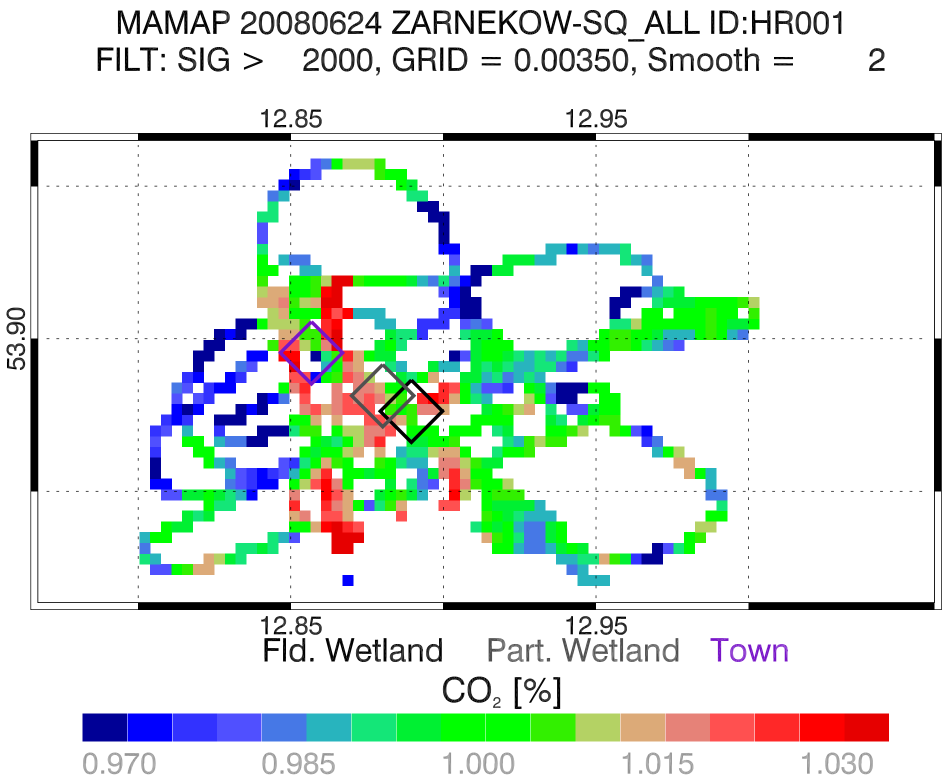

Figure 40: Zarnekow - 24-06-2008. Above: CH_4 column factor map. Below: CO_2 column factor map.

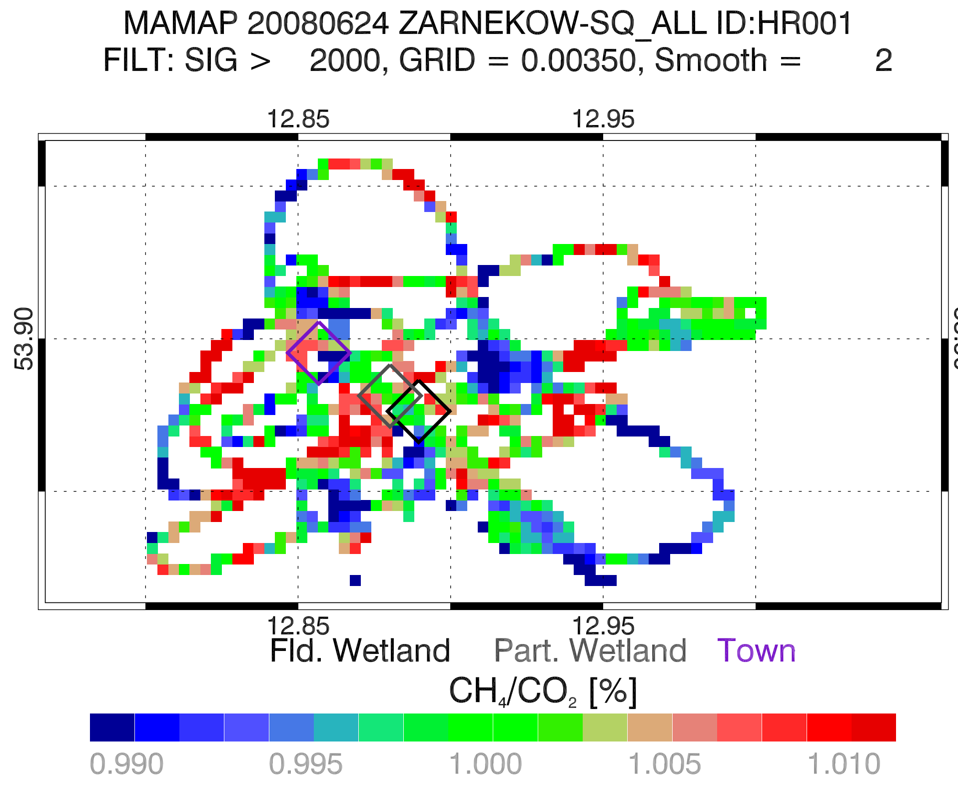

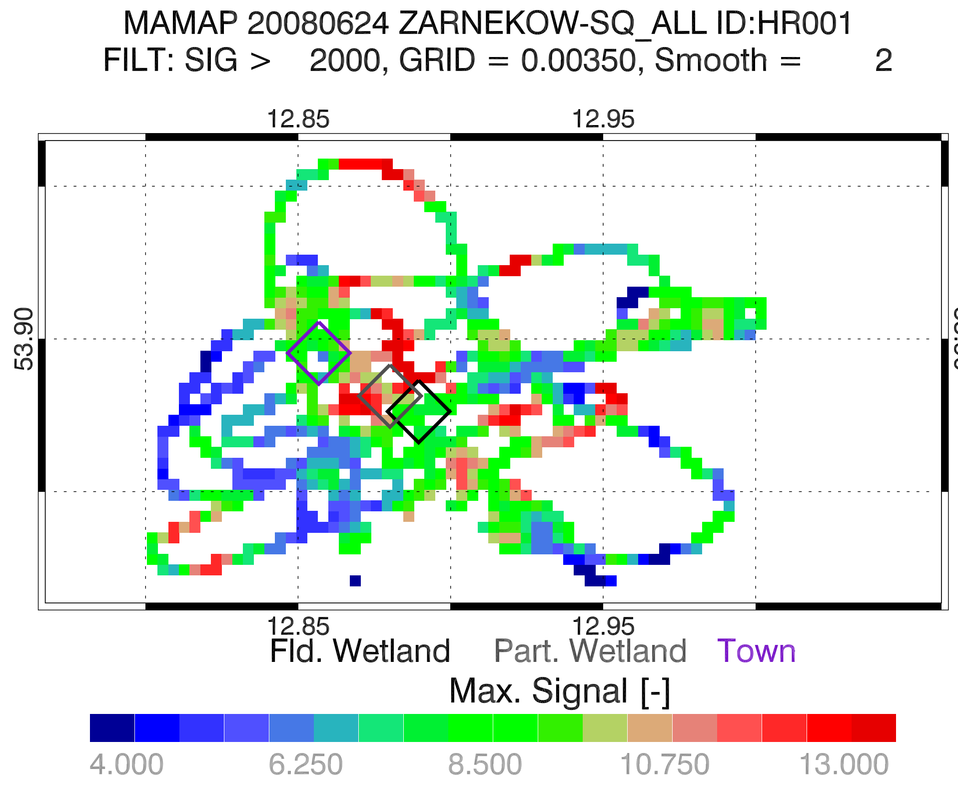

Figure 41: Zarnekow - 24-06-2008. Above: CH_4/CO_2 column factor ratio map. Below: maximum signal map.

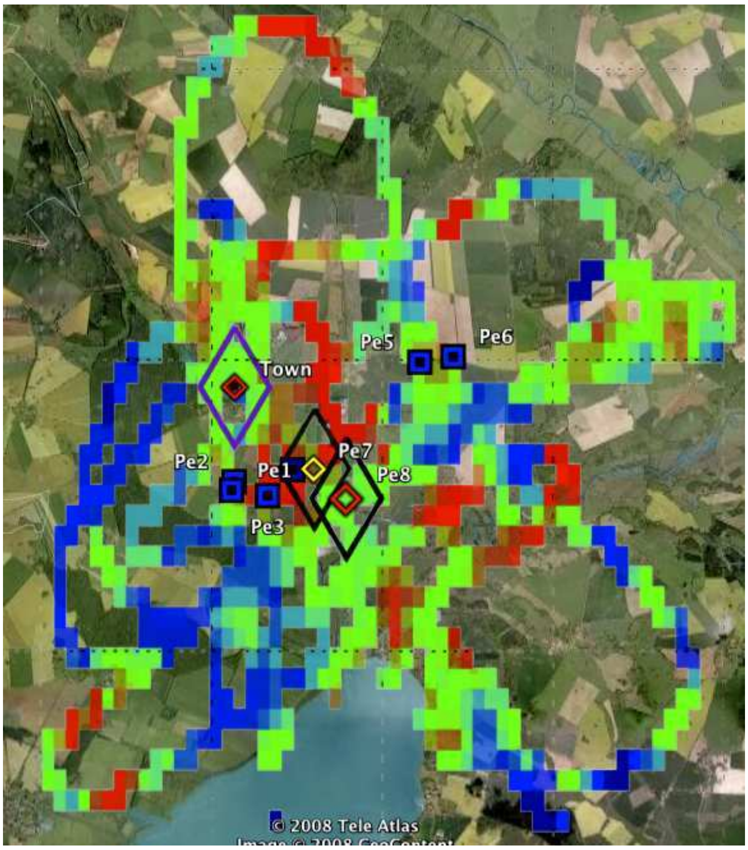

Figure 42: Zarnekow 24-06-2008. MAMap data superimposed on aerial imagery. Maximum signal. Scale: 4000-13000 counts.

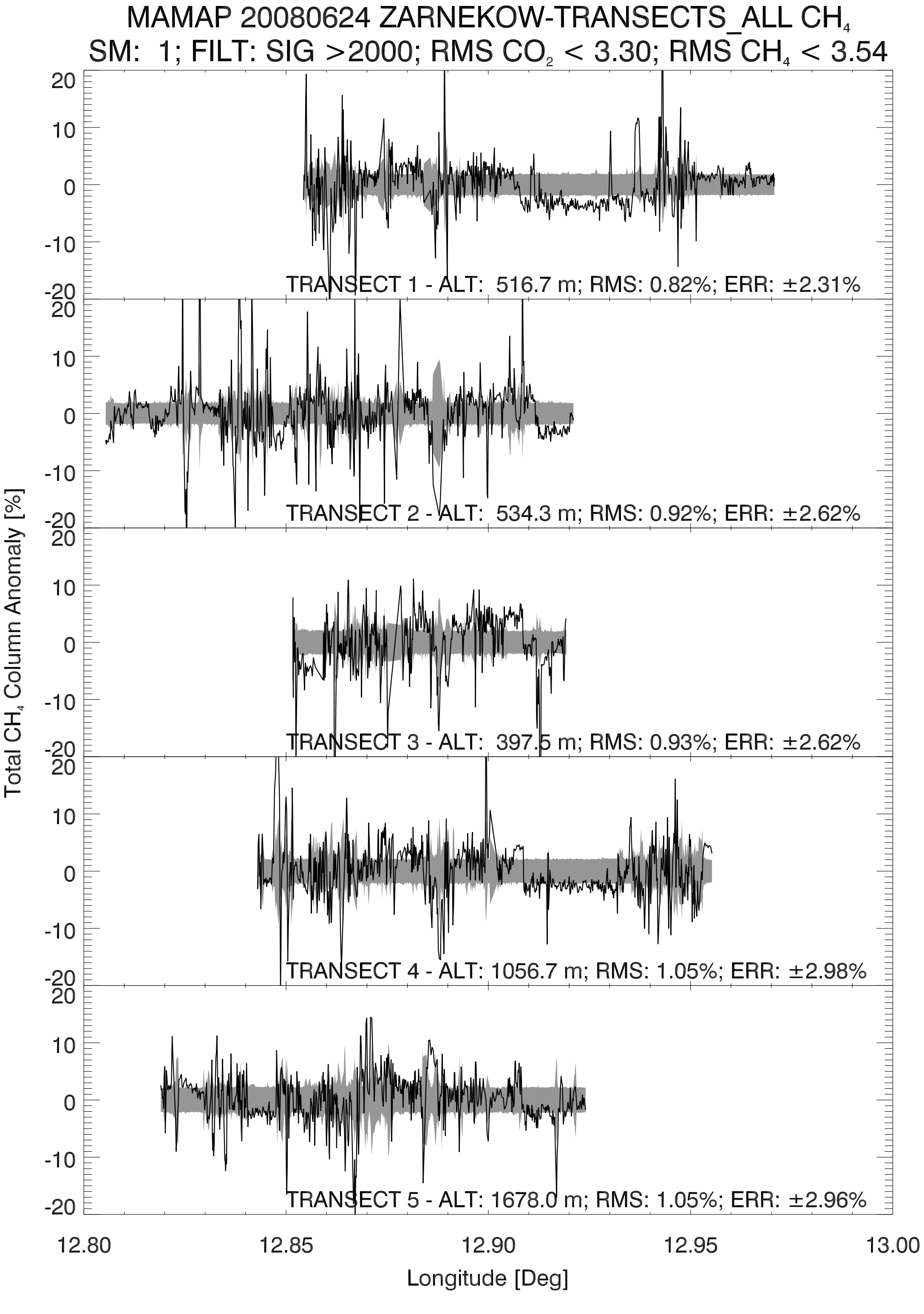

Figure 43: Zarnekow wetlands. Flight of 24-06-2008. Relative anomaly in the CH_4 column factor over Site 8. No data averaging, all the valid data points are displayed. The error range from the average value is displayed in grey. The scatter (standard deviation) of the values in the different transects ranges between 4.3% and 5.8%.

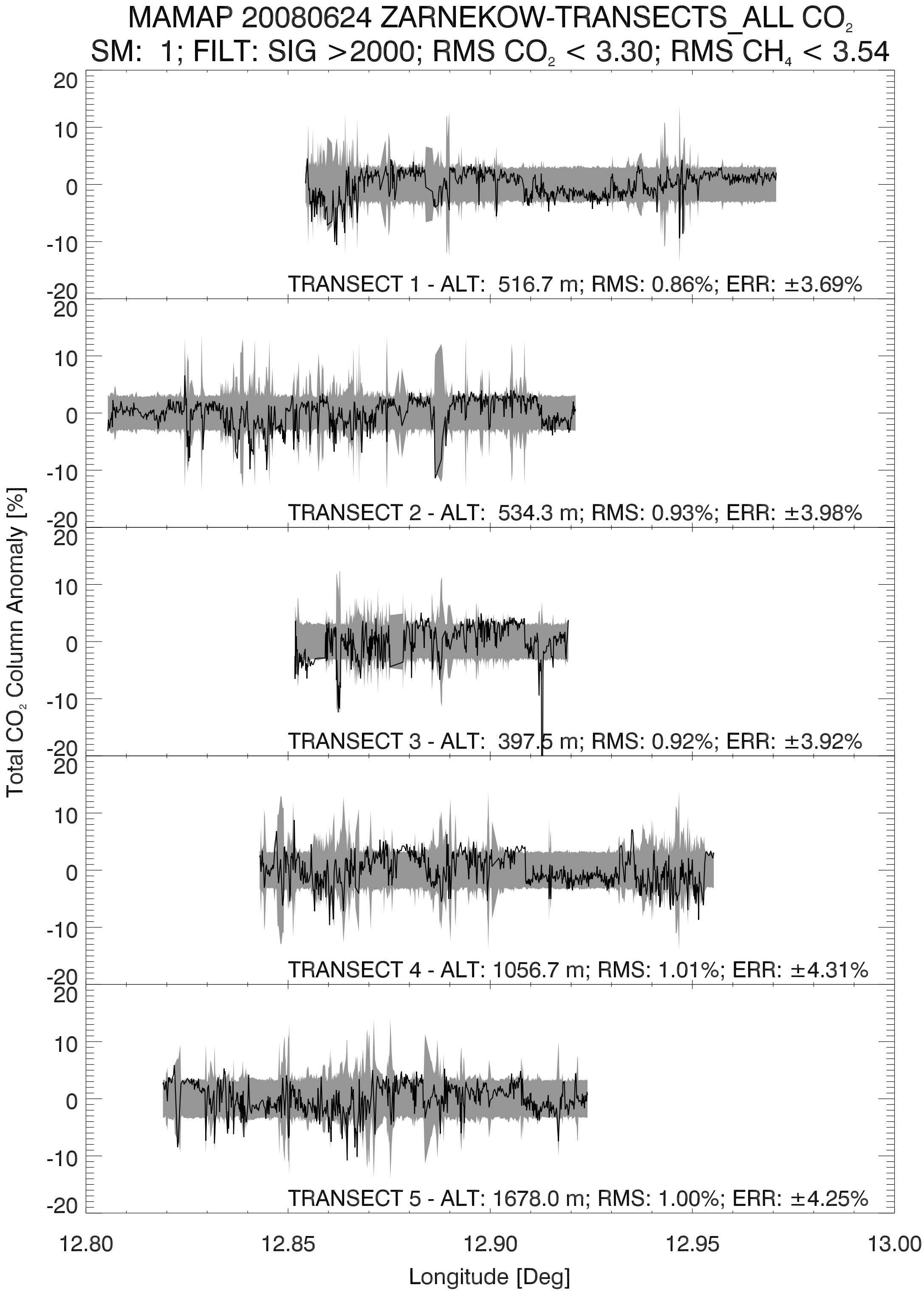

Figure 44: Zarnekow wetlands. Flight of 24-06-2008. Relative anomaly in the CO_2 column factor over Site 8. No data averaging, all the valid data points are displayed. The error range from the average value is displayed in grey. The scatter (standard deviation) of the values in the different transects ranges between 2.2% and 3.5%.

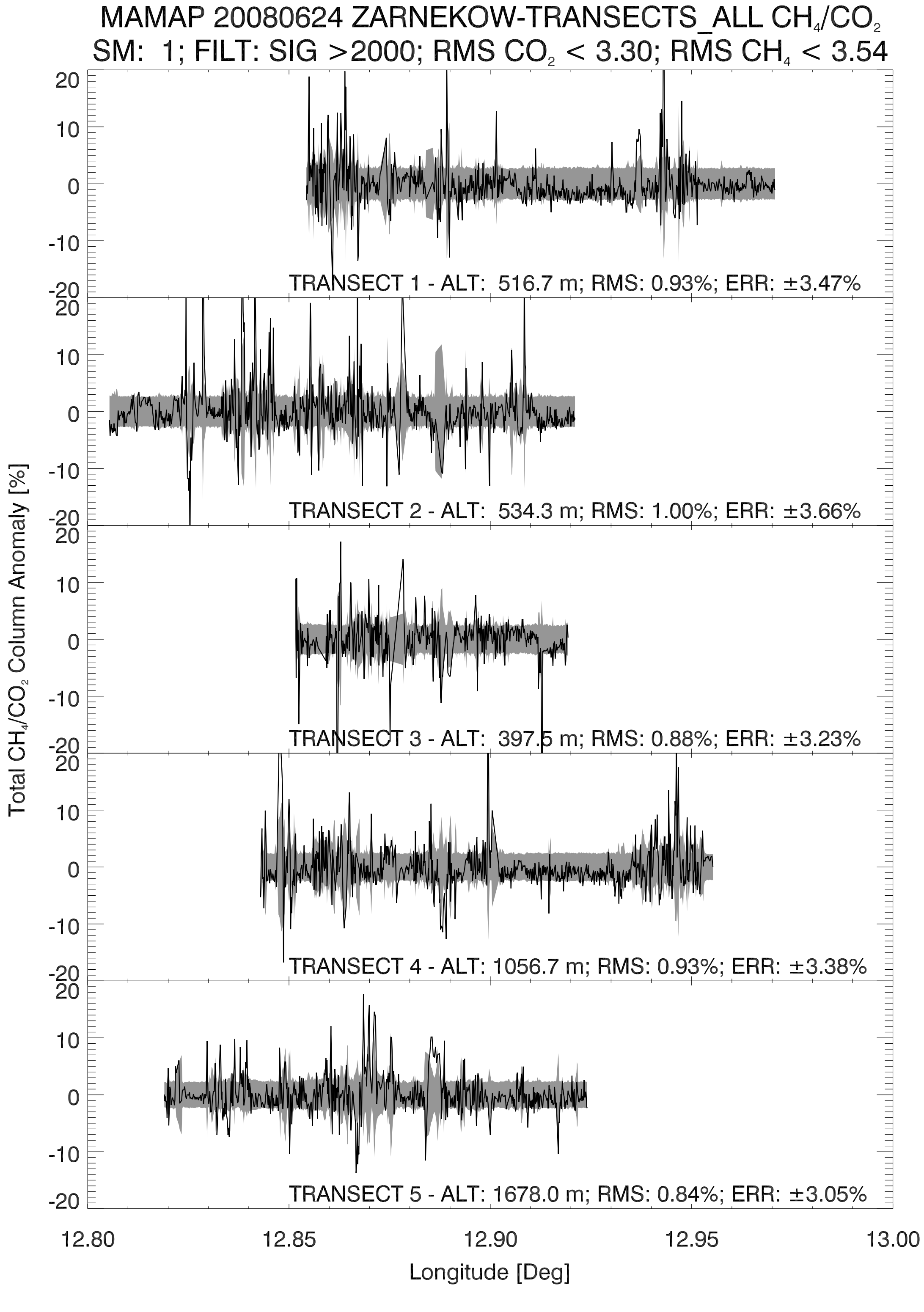

Figure 45: Zarnekow wetlands. Flight of 24-06-2008. Relative anomaly in the CH_4/CO_2 column factor ratio over Site 8. No data averaging, all the valid data points are displayed. The error range from the average value is displayed in grey. The scatter (standard deviation) of the values in the different transects ranges between 3.3% and 4.7%.

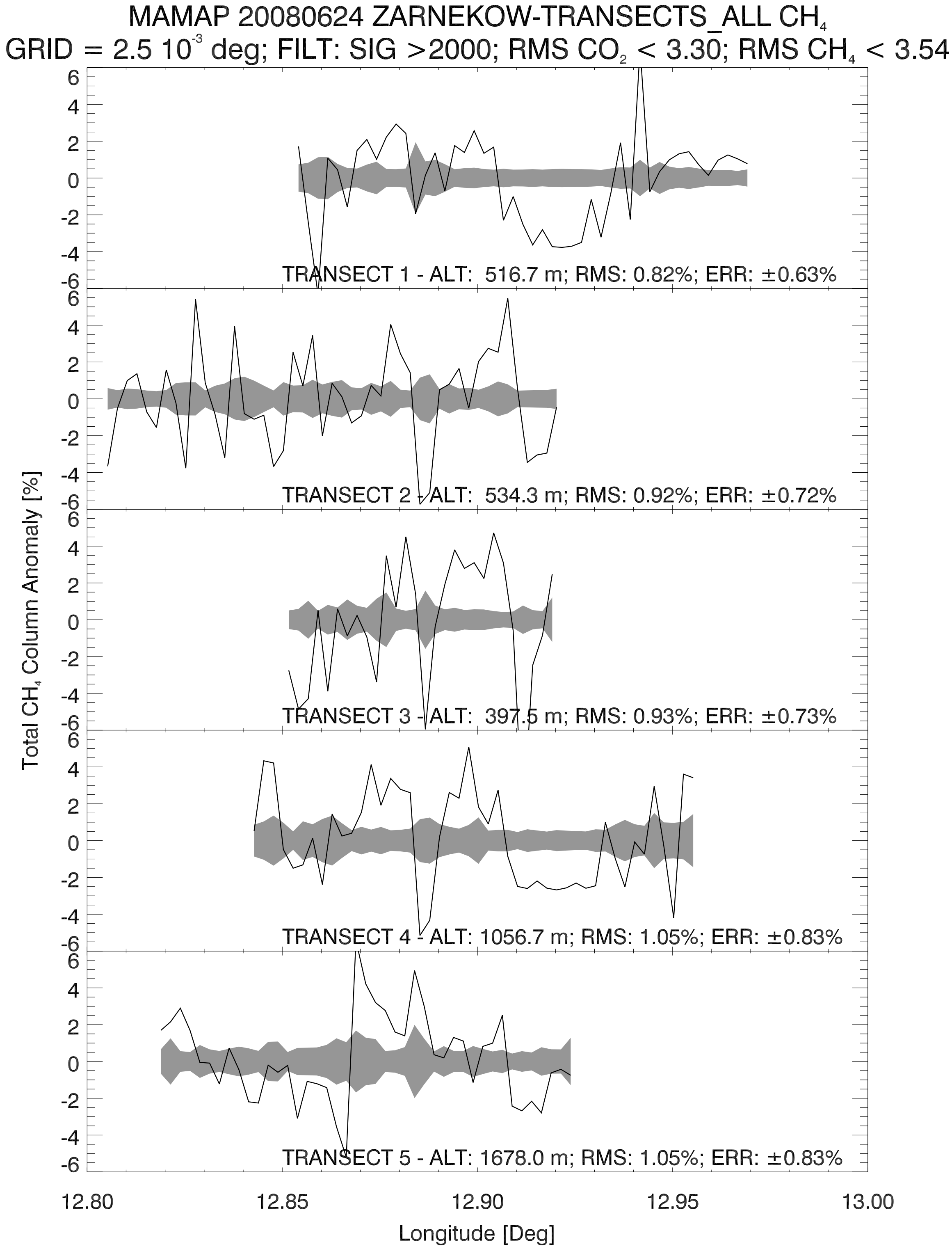

Figure 46: Zarnekow wetlands. Flight of 24-06-2008. Relative anomaly in the CH_4 column factor over Site 8. Data averaged on a constant grid of 0.0035º size. The error range from the average value is displayed in grey.

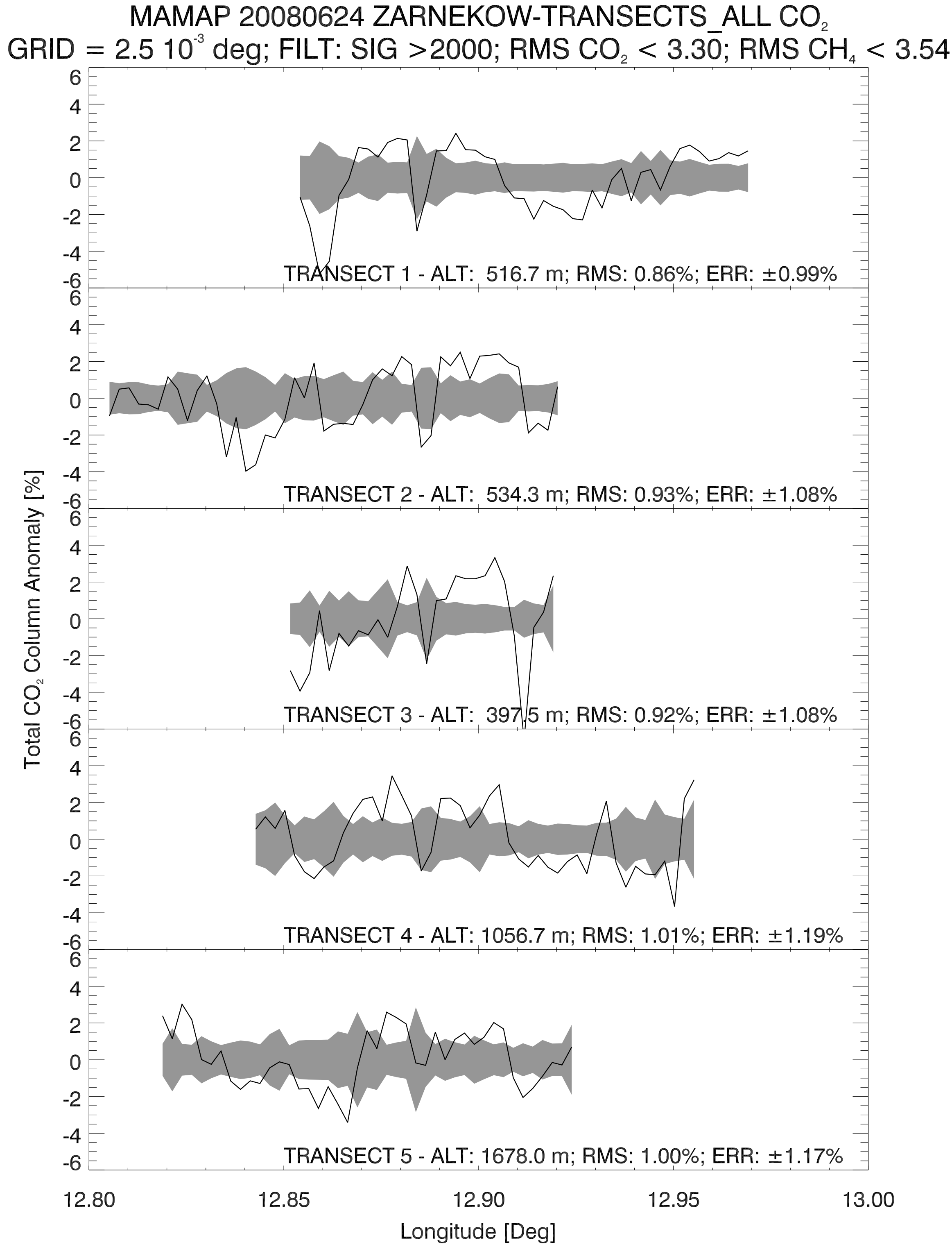

Figure 47: Zarnekow wetlands. Flight of 24-06-2008. Relative anomaly in the CO_2 column factor over Site 8. Data averaged on a constant grid of 0.0035º size. The error range from the average value is displayed in grey.

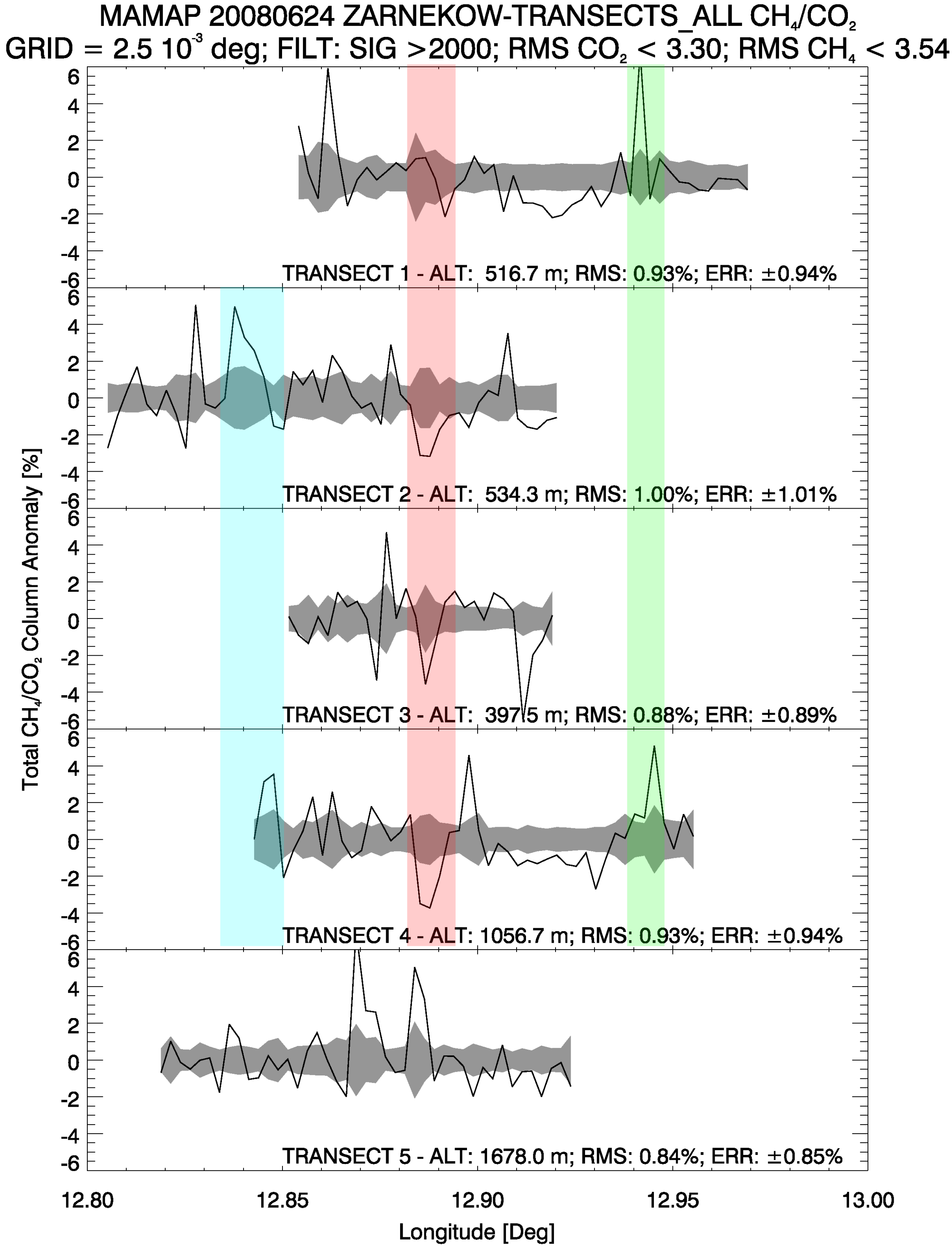

Figure 48: Zarnekow wetlands. Flight of 24-06-2008. Relative anomaly in the CH_4/CO_2 column factor ratio over Site 8. Data averaged on a constant grid of 0.0035° size. The error range from the average value is displayed in grey.

11 An artificial methane source: the Ketzin experiment

Another experiment has been designed and realized to test if MAMap can detect localized high concentrations of methane. A standard laboratory methane flask has been transported in an open field area and its geographic coordinates used as target for the flight track. The flask was then opened at the same time when the instrument was flying over and measuring. The goal of the experiment was to detect the methane plume originating from the bottle against the natural background. Due to the small surface of the methane-enhanced area, in this analysis no averaging was employed, because the full spatial resolution of the instrument was needed.

11.1 Target description

Position: Near Etzin, Havelland District, Brandenburg, Germany, approximately 17 km NNW of Potsdam, 35 km W of Berlin. Wetlands in the Peene river area.

Coordinates: Methane Bottle: Lat 52°30'46" N Lon 12°53'55" E

Features: The GeoForschungZentrum Potsdam (GFZ) runs a CO_2 monitoring station included in the CO_2SINK project of the European Commission. It is a former natural gas storage facilities from the 1960s now used as an experimental CO_2 sequestration site. For this reason, it is expected not to be either a source or sink for greenhouse gases, and a good neutral background for the experiment.

11.2 Expected signal strength

Since the source to be observed is artificial and localized, the methane column enhancement is estimated using the same procedure introduced in Section 9.2. The most important parameters to estimate the increase in the methane column relative to the background are the number of molecules released per second and the area over which they are spread. The amount of gas E released by the flask can be estimated in approximately 2 liters per second, due to the valve discharge. This corresponds to $E = 6.18 \cdot 10^{28}$ molecules/s. The area L^2 over which the enhancement must be spread is given by the ground pixel size of the instrument: since the spectrometer has an instantaneous field of view of 1.34^{o}, when the airplane flies at an altitude of 500 m this gives a ground pixel size of 12 m. The methane flux $F = E/L^2$ will then be equal to $4.52 \cdot 10^{16}$ molecules/cm^2 s. The weather records report a wind speed of 5 knots, approximately equal to 2.5 m/s. An accumulation time $\tau = 4.5$ s then results, and $\Delta C = 2 \cdot 10^{17}$ molecules/cm^2. The average atmospheric methane

$$\begin{array}{rcc} I_{max} & > & 5000 \text{ counts} \\ \|RES\|^2_{CH_4} & < & 0.60 \ \% \\ \|RES\|^2_{CO_2} & < & 0.77 \ \% \end{array}$$

Table 9: Filter specifications for the Ketzin target, 24-06-2008 flight.

column is $C = 3.5 \cdot 10^{19}$ molecules/cm^2 (Buchwitz, 2000), and the expected relative enhancement $\Delta C/C$ then equal to 0.6%.

11.3 Data selection and filtering

The features of the fit residuum distributions are similar to those of the other targets, with median values of 0.49% for CH_4 and 0.63% for CO_2 (cfr. Figures 50 and 51). However, the low expected signal level and the need to rely on the high-resolution data induced to adopt a stricter filtering on the CH_4 residuum, excluding 1637 out of 10410 elements, that is 15.7% of the total.

11.4 Spatial analysis and comparison with ground type information

Due to the small size of the target, each single measured spectrum needed to be accurately geolocated. For the first time, the fact that the measurements are actually not continuous, but performed for 0.58 s every 2.00 seconds has a significant impact. Due to the high speed of the aircraft (180 km/h ca., equivalent to 50 m/s), the probability to fly over the bottle while the instrument is not in detection mode becomes significant. The results are presented in Figure 49.

11.5 Time series analysis

Figure 52 shows the CH_4/CO_2 column ratio for the whole flight track around the Ketzin target. To highlight the small-scale changes in the ratio, a high-pass filter with a step of 150 points has been applied. The data presents a constant scatter around the mean on the order of 2-3%. This is larger than the expected signal from the methane release, and would be enough to affirm that the signal-to-noise ratio is not high enough to be able to distinguish the target from the background. In addition, the the data points closest to the target (highlighted in red in the figure) are selected and examined, but the number of points with values above the average is not significant.

A further confirm comes from an exam of a smaller area (ca. 400 m radius) around the target, presented in Figure 53, and corresponding to the region displayed in Figure 49. Again, no significant enhancement is evident at the points closest to the target.

It can be concluded that, after a post-flight analysis of the data, the signal produced by the artificial methane release proved to be under the background level, and not detectable at this stage.

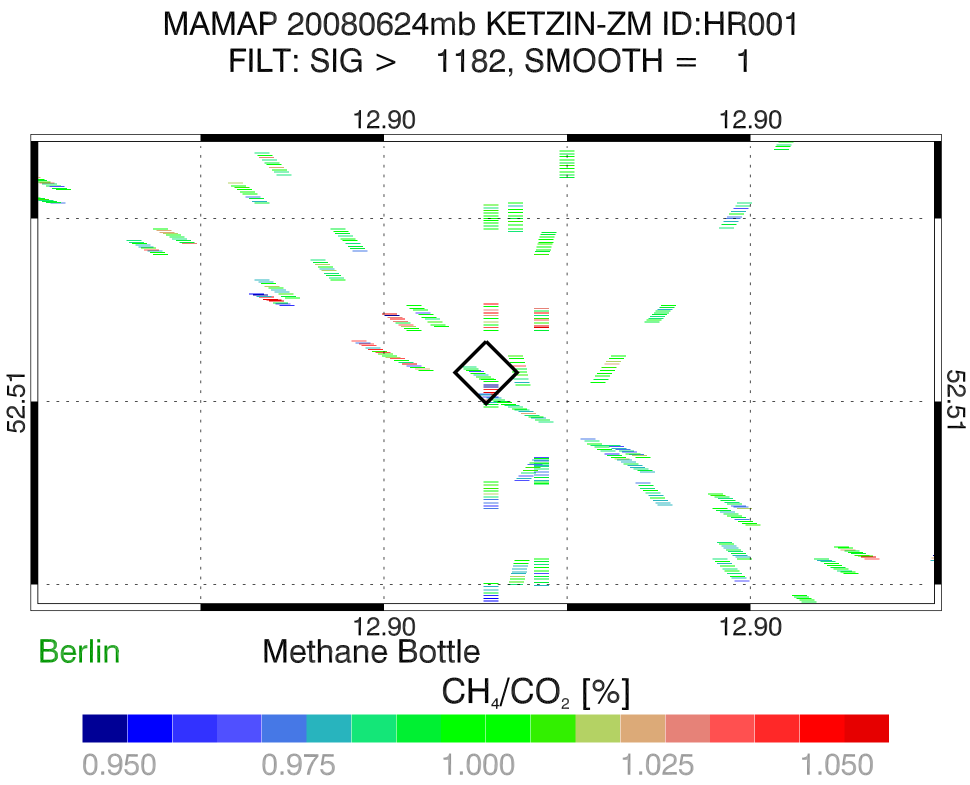

Figure 49: Ketzin - 24-06-2008. CH_4/CO_2 column factor ratio map. The single spectra are plotted, with their actual geolocation based on the instrument internal clock.

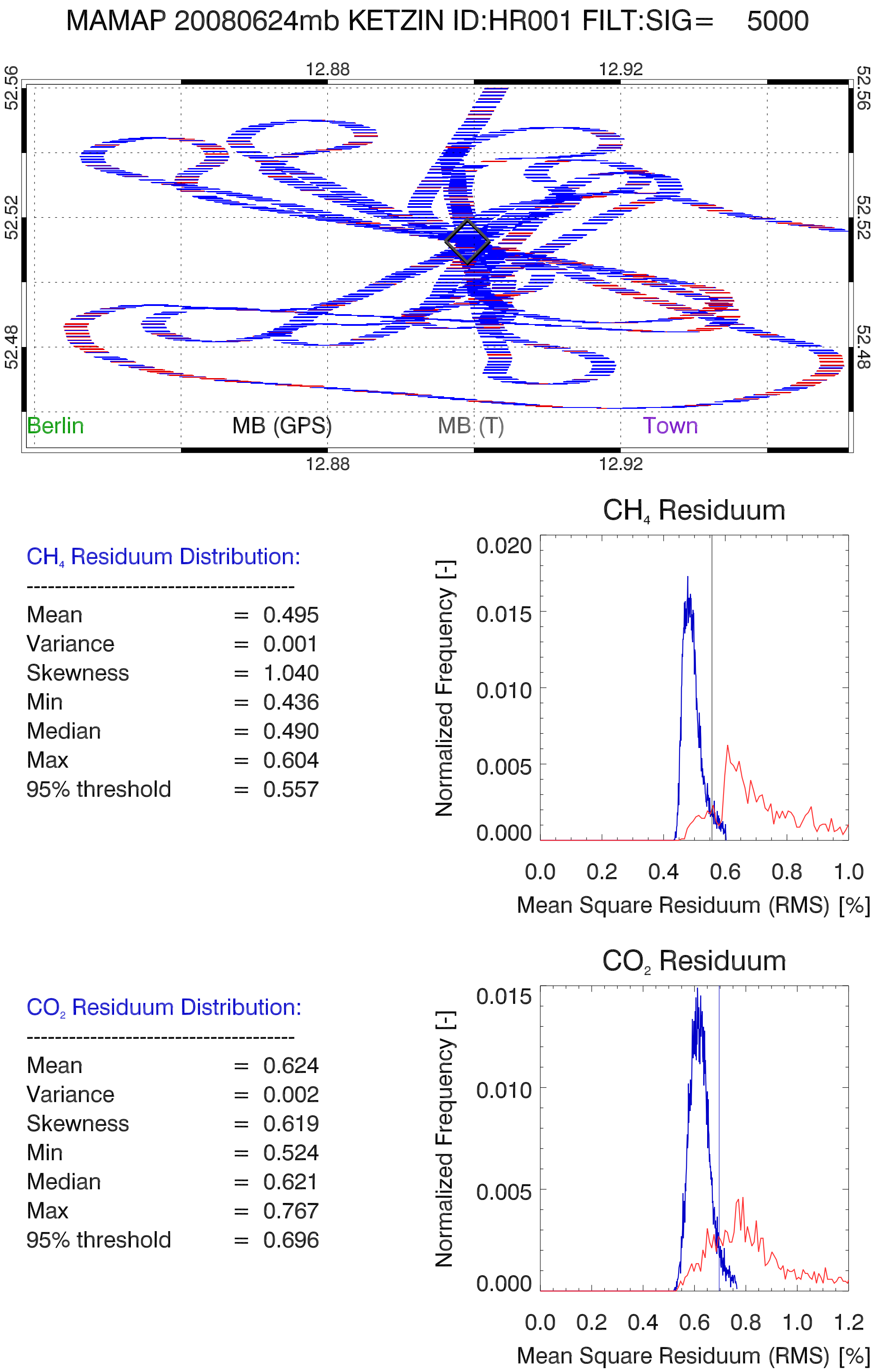

Figure 50: Filtering for the Ketzin target, flight of 24-06-2008. Red represents the data filtered out. On top, map of the flight track. On the right, frequency histograms of the fit residua. On the left, statistics of the dataset used for the analysis, post filtering.

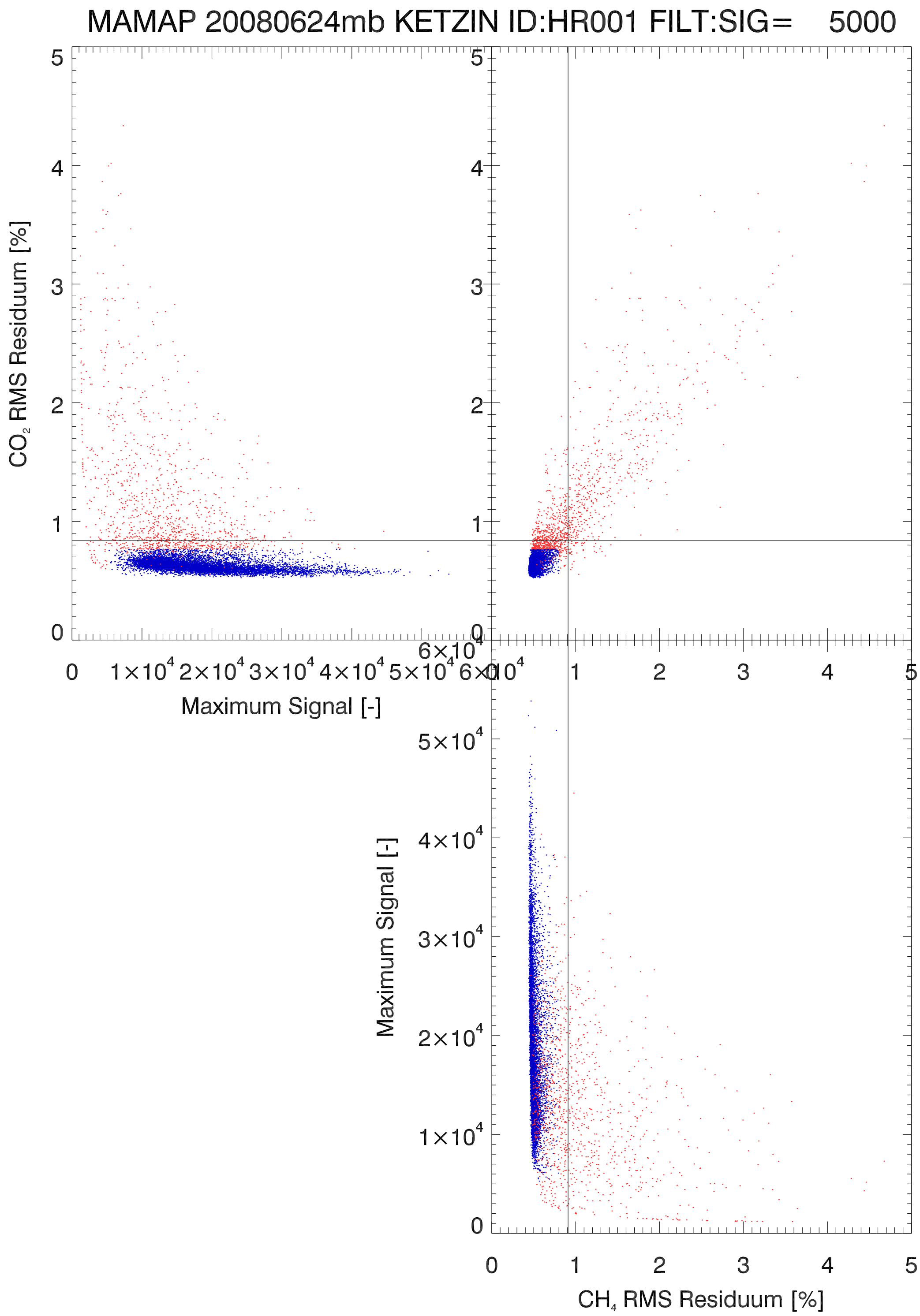

Figure 51: Three-dimensional scatterplot for the Ketzin target, flight of 24-06-2008. The valid data points are displayed in blue, the ones filtered out in red.

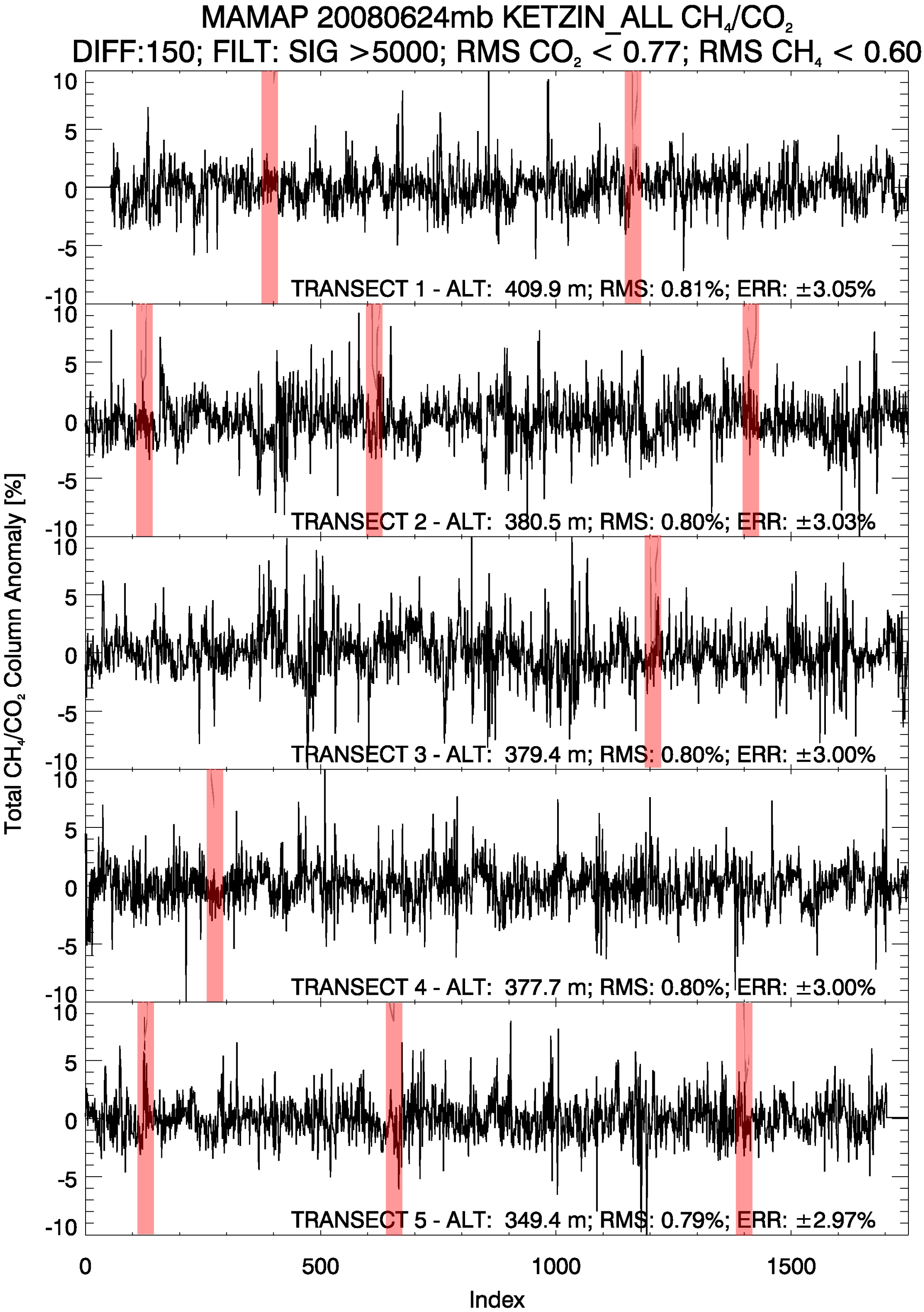

Figure 52: Ketzin methane flask experiment. Flight of 24-06-2008. Relative anomaly in the CH_4/CO_2 column factor ratio over the methane flask. No data averaging, all the valid data points are displayed. The red stripes mark the positions where the distance from the target is minimal and a CH_4 enhancement is expected.

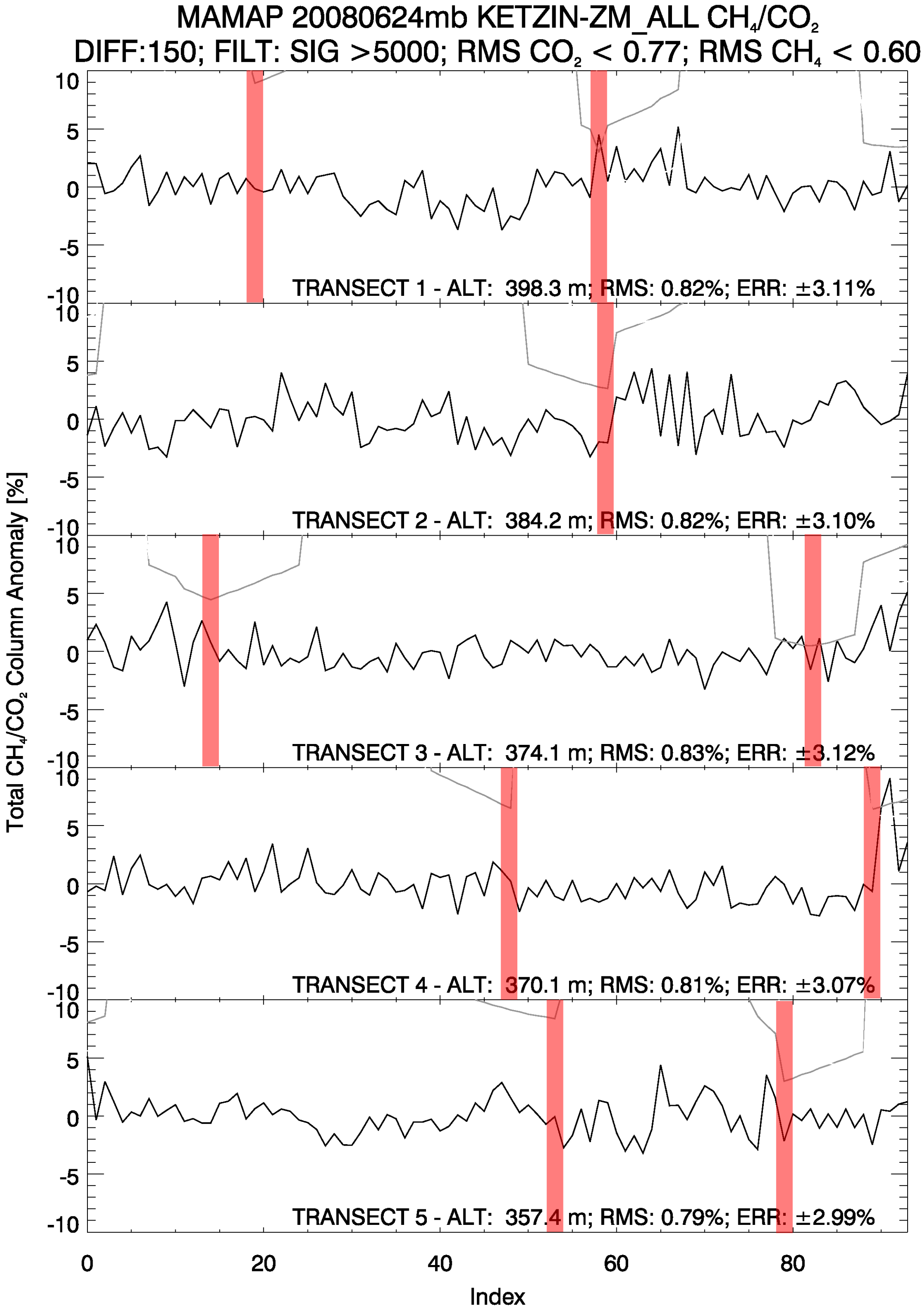

Figure 53: Ketzin methane flask experiment. Flight of 24-06-2008. Relative anomaly in the CH_4/CO_2 column factor ratio in 400 m radius around the methane flask. No data averaging, all the valid data points are displayed. The grey line represents the relative distance to the target. The red stripes mark the positions where the distance from the target is minimal and a CH_4 enhancement is expected.

Part V

Conclusions

Several analyses have been performed in order to assess the capabilities of the MAMap instrument to detect a localized source of methane. The analyses have been limited to the results of the SWIR (CH_4/CO_2) sensor, considered sufficient for a preliminary investigation.

A one-dimensional model of the lower 3 km of the atmosphere has been used to compare ground mixing ratios measured at different stations (expressed in parts per billion - ppb) to the detection capabilities of MAMap (expressed in percent of the vertical column, molecules per cm^2). It has been found that to have an enhancement of 3% of the vertical column under the aircraft, flying at 3 km altitude, an increase from the background of 75-250 ppb at the ground is required, depending on the boundary layer conditions. It can be concluded then that MAMap is well designed to observe large regional increases like the Siberian wetlands, whose emissions are systematically higher than the worse estimate for the detection capabilities (250 ppb from the background).

A theoretical estimate of the signal-to-noise levels and of the fit errors has been carried on, by simulating the measurement and the retrieval based on instrument parameters (e.g. dark current) and geophysical parameters (e.g. surface albedo, solar zenith angle). It can be concluded that the theoretical fit error due to instrument noise, for an exposure time of 58 ms and a surface albedo of 0.15, typical of a land ground scene, is on the order of 1% of the total column. For open water, instead, with a surface albedo of 0.02, the lower signal-to-noise ratio determines theoretical fit errors on the order of 5%. Longer exposure times are then recommended for measurements over water. An analysis of the instrument noise from actual flight data is still to be performed, and is planned as a future goal.

The calibration spectra (dark signal, white light source) of the 2007 flights have been analysed, and no significant change in the performance of the instrument has been observed, within a distance of months. A thorough examination of the fit residua showed that the intensity of the incoming radiance, that is the signal strength, has the largest impact in determining the precision of the fit results. This implies that the illumination of the target scene (due to solar zenith angle, season, cloud coverage) is a crucial factor for the planning and the measurement analysis of flight missions.

A first analysis of the results of the flight of 26-07-2007 over the Schwarze Pumpe power plant has been performed. It was expected to observe an anthropogenic CO_2 enhancement (the emission plume of the power plant) on the order of several percent.

This target had been chosen to test analysis techniques that have then been used on later, less defined targets. From the exam of the results, both as maps and as time series, the detection of the plume has been confirmed. The maximum value from the detected spectra is confirmed as in good agreement with the expected albedos. Filtering and averaging steps have proven necessary, to reduce the data scatter and the measurement uncertainties. The fit errors were 2-4 times larger than the theoretical values based on instrument noise. It can be concluded that these errors are affected by systematic biases in the retrieval, and overestimate the real uncertainties.

The same technique has been applied on the data collected on 24-06-2008 over a natural source of methane, the Zarnekow wetland, with less conclusive results. Some correlation has been observed between enhancements in the CH_4/CO_2 column ratio and the expected emissions at the surface, based on land cover and vegetation type. The repeatability of the measurements has been also tested, with positive results; flight overpasses on the same trajectory at different altitudes show coherent patterns of increases and decreases in the gas columns. Still, a comparison with the ground data gathered in the same campaign will prove useful in the interpretation of the results.

The results of the Ketzin experiment (24-06-2008) with an artificial methane release are also presented. The expected column increase was estimated by the amount of methane released, and compared to the high-resolution flight data. The data scatter of the measurements proved to be larger than the expected signal, and no averaging was possible due to the small size of the target. The synchronization of the measurement cycle with the flight over the target proved to be an issue as well. At the actual state of the measurements, then, there is no conclusive assessment of the capability of the instrument to detect a small, localized artificial methane release. Other experiments are already planned to this purpose.

A Other Targets

A.1 COTTBUS (Open Coal Mines)

Position: Near the Schwarze Pumpe and Jänschwalde power plants, in the Spree-Neisse district around Cottbus.

Coordinates: Open Coal Mine 1: Lat 51.8021° N Lon 14.5374° E
Open Coal Mine 2: Lat 51.6013° N Lon 14.2794° E

Features: During the data analysis of the 26-07 flight, extremely low CH_4/CO_2 ratio were measured over an area belonging to a open air coal mining. This became immediately a new research target, in order to investigate the possibility of enhanced CO_2 emissions.

Flights: 26-07-2007, one casual overpass. 31-10-2007, several planned overpasses.

A.2 PAULIN AUE (Wetlands)

Position: Near Nauen, Havelland District, Brandenburg, Germany, approximately 40 km NNW of Potsdam, 50 km WNW of Berlin.

Coordinates: Lat 52°41'10" N Lon 12°43'22" E

Figure 54: Paulin Aue floodplain measurement site. The yellow numbers correspond to the four terrain types described in the text.

Features: This wetland area lies in the floodplain of the Havel river. The ZALF Institute maintains an experimental field station there for agricultural research. Four different terrain types were isolated or reproduced to measure the different CO_2 and

CH_4 emissions. The four terrains are (1) extensive grassland, (2) simulated pasture, re-created by spreading liquid farmyard manure on open land, (3) trodden pasture, (4) intensive grassland. Over these sites several gas samples were taken and then processed at the ZALF laboratory in Münchenberg.

Flights: On both 01-08-2007, 02-08-2007 flights this was one of the main targets.

References

Baker, D. F. (2007). Reassessing carbon sinks. *Science*, 316:1708–1709.

Belikov, I., Brenninkmeijer, C., Elansky, N., and Ral'ko, A. (2006). Methane, carbon monoxide, and carbon dioxide concentrations measured in the atmospheric surface layer over continental russia in the TROICA experiments. *Izvestiya, Atmospheric and Oceanic Physics*, 1:46–59.

Bergamaschi, P., Krol, M., Dentener, F., Vermeulen, A., Meinhardt, F., Graul, R., Ramonet, M., Peters, W., and Dlugokencky, E. J. (2005). Inverse modelling of national and european CH4 emissions using the atmospheric zoom model TM5. *Atmospheric Chemistry and Physics*, (5):2431–2460.

Bousquet, P., Ciais, P., and J.B., M. (2006). Contribution of anthropogenic and natural sources to atmospheric methane variability. *Nature*, 443:439–443.

Brook, E. J. (2005). Tiny bubbles tell all. *Science*, 310.

Buchwitz, M. (2000). *Strahlungtransport- und Inversions-Algorithmen zur Ableitung atmosphärischer Spurengasinformationen aus Erdfernerkundungsmessungen in Nadirgeometrie im ultravioletten bis nahinfraroten Spektralbereich am Beispiel SCIAMACHY.* PhD thesis, IUP/IFE Universität Bremen.

Buchwitz, M. (2003). *User's Guide for the Radiative Transfer Program SCIATRAN - Version 1.2 -*. Institute of Remote Sensing, University of Bremen, FB1.

Buchwitz, M., de Beek, R., Burrows, J., Bovensmann, H., Warneke, T., Notholt, J., Meirink, J., Goede, A., Bergamaschi, P., Körner, S., Heimann, M., and Schulz, H. (2005). Atmospheric methane and carbon dioxide from SCIAMACHY satellite data: initial comparison with chemistry and transport models. *Atmos. Chem. Phys.*, 5:941–962.

Buchwitz, M., Rozanov, V., and Burrows, J. (2000). A near-infrared optimized DOAS method for the fast global retrieval of atmospheric CH4, CO, CO2, H2O, and N2O total column amounts from SCIAMACHY Envisat-1 nadir radiances. *Journal of Geophysical Research*, 105:15,231 – 15,245.

Buchwitz, M., Schneising, O., Burrows, J. P., Bovensmann, H., Reuter, M., and Notholt, J. (2007). First direct observation of the atmospheric co2 year-to-year increase from space. *Atmos. Chem. Phys.*, 7:4249–4256.

Forster, P., Ramaswamy, V., Artaxo, P., Berntsen, T., Betts, R., Fahey, D., Haywood, J., Lean, J., Lowe, D., Myhre, G., Nganga, J., Prinn, R., Raga, G., Schulz, M., and Dorland, R. V. (2007). *Climate Change 2007: The Physical Science Basis. Contribution of Working Group I to the Fourth Assessment Report of the Intergovernmental Panel on Climate Change*, chapter 2007: Changes in Atmospheric Constituents and in Radiative Forcing. Cambridge University Press.

Frankenberg, C., Meirink, J. F., van Weele, M., Platt, U., and Wagner, T. (2005a). Assessing methane emissions from global space-borne observations. *Science*, 308:1010–1014.

Frankenberg, C., Platt, U., and Wagner, T. (2005b). Iterative maximum a posteriori (IMAP)-DOAS for retrieval of strongly absorbing trace gases: Model studies for CH4 and CO2 retrieval from near infrared spectra of SCIAMACHY onboard ENVISAT. *Atmos. Chem. Phys.*, 5:9–22.

Keppler, F., Hamilton, J. T. G., Braß, M., and Röckmann, T. (2006). Methane emissions from terrestrial plants under aerobic conditions. *Nature*, 439:187–191.

Lelieveld, J. (2006). A nasty surprise in the greenhouse. *Nature*, 443:405–406.

Lillesand, T. and Kiefer, R. (2000). *Remote sensing and image interpretation*. John Wiley, New York.

Lowe, D. C. (2006). A green source of surprise. *Nature*, 439:148–149.

Marques Filho, E. P., de Oliveira, A. P., Rizza, U., and Karam, H. A. (2006). Pollutant transport in a convective boundary layer with les. *Revista Brasileira de Geofisica*, 24(4):547–557.

McClatchey, R. A., Fenn, R. W., Selby, J. E. A., Volz, F. E., and Garing, J. S. (1972). Optical properties of the atmosphere (third edition). *Environmental research papers*.

Miller, J. B., Gatti, L. V., d'Amelio, M. T. S., Crotwell, A. M., Dlugokencky, E. J., Bakwin, P., Artaxo, P., and Tans, P. P. (2007). Airborne measurements indicate large methane emissions from the eastern amazon basin. *GEOPHYSICAL RESEARCH LETTERS*, 34.

Oberlander, E., Brenninkmeijer, C., Crutzen, P., Elansky, N., Golitsyn, G., Granberg, I., Scharffe, D., Hofmann, R., Belikov, I., Paretzke, H., and van Velthoven, P. (2002). Trace gas measurements along the Trans-Siberian railroad: The TROICA 5 expedition. *Journal of Geophysical Research*, (14).

Petit, J. R., Jouzel, J., Raynaud, D., Barkov, N. I., Barnola, J.-M., Basile, I., Bender, M., Chappellaz, J., Davis, M., Delaygue, G., Delmotte, M., Kotlyakov,

V. M., Legrand, M., Lipenkov, V. Y., Lorius, C., Pépin, L., Ritz, C., Saltzman, E., and Stievenard, M. (1999). Climate and atmospheric history of the past 420,000 years from the Vostok ice core, Antarctica. *Nature*, 399:429–436.

Press, W., Teukolsky, S., Vetterling, W., and Flannery, B. (1992). *Numerical Recipes in Fortran*. Cambridge University Press, London.

Richter, A. (2007). Introduction to Measurement Techniques in Atmospheric Physics: Differential Optical Absorption Spectroscopy (DOAS).

Rodgers, C. D. (2000). *Inverse methods for atmospheric sounding : theory and practice*, volume 2 of *Series on atmospheric oceanic and planetary physics*. World Scientific, xvi edition.

Schlitzer, R. (2006). Introduction to Inverse Methods and Mathematical Data Analysis.

Schneising, O. (2008). *Analysis and interpretation of satellite measurements in the near-infrared spectral region: Carbon dioxide and methane (DRAFT)*. PhD thesis, University of Bremen.

Schneising, O., Buchwitz, M., Burrows, J. P., Bovensmann, H., Bergamaschi, P., and Peters, W. (2008a). Three years of greenhouse gas column-averaged dry air mole fractions retrieved from satellite - Part 2: Methane. *Atmospheric Chemistry and Physics Discussions*, 8:8273 – 8326.

Schneising, O., Buchwitz, M., Burrows, J. P., Bovensmann, H., Reuter, M., Notholt, J., Macatangay, R., and Warneke, T. (2008b). Three years of greenhouse gas column-averaged dry air mole fractions retrieved from satellite – part 1: Carbon dioxide. *Atmospheric Chemistry and Physics*, 8(14):3827–3853.

Severinghaus, J., Sowers, T., Brook, E., Alley, R., and Bender, M. (1998). Timing of abrupt climate change at the end of the Younger Dryas interval from thermally fractionated gases in polar ice. *Nature*, 391.

Trenberth, K. E., Christy, J. R., and Olson, J. G. (1988). Global atmospheric mass, surface pressure, and water vapor variations. *JOURNAL OF GEOPHYSICAL RESEARCH*, 93(D9):10,925.

VDEW, V. d. E. (2000). Energiewelten. Informational CD-ROM for schools.

von Savigny, C. (2007). Introduction to measurement techniques in atmospheric physics: Atmospheric remote sensing.

Wallace, J. M. and Hobbs, P. V. (2006). *Atmospheric science: an introductory survey*. Number 92 in International Geophysics Series. Elsevier, 2nd edition.

Walter, B. P., Heimann, M., and Matthews, E. (2001). Modeling modern methane emissions from natural wetlands 1. Model description and results. *Journal of Geophysical Research*, 106(D24):34,189–34,206.

Walter, K., Zimov, S., Chanton, J., Verbyla, D., and III, F. C. (2006). Methane bubbling from Siberian thaw lakes as a positive feedback to climate warming. *Nature*, (443):71–75.

WWF, E. P. O. (2007). Dirty Thirty - Ranking of the most polluting power stations in Europe.